Universiteit Gent
Faculteit Ingenieurswetenschappen
Vakgroep Elektrische energie, Systemen en Automatisering

Exploring the limitations of linear and nonlinear vibration absorbers

Over de beperkingen van lineaire en niet-lineaire trillingsdempers

Frits Petit

Proefschrift tot het bekomen van de graad van
Doctor in de Ingenieurswetenschappen:
Werktuigkunde-Electrotechniek
Academiejaar 2011-2012

Universiteit Gent
Faculteit Ingenieurswetenschappen
Vakgroep Elektrische energie, Systemen en
Automatisering

Promotoren: Prof. Dr. Ir. Mia Loccufier
Prof. Dr. Ir. Dirk Aeyels

Universiteit Gent
Faculteit Ingenieurswetenschappen

Vakgroep Elektrische energie, Systemen en Automatisering
Technologiepark Zwijnaarde 914, B-9042 Zwijnaarde, België

Tel.: +32-9-264.56.57
Fax.: +32-9-264.58.40

Proefschrift tot het behalen van de graad van
Doctor in de Ingenieurswetenschappen:
Werktuigkunde-Electrotechniek
Academiejaar 2011-2012

Acknowledgements

I am very pleased that you are reading these few lines as it means that the hard work has finally paid off. I am in great depth to all of you. You have supported me, encouraged me and made me laugh when I needed to. Without your help, finishing the PhD would not have been possible.

First of all, I would like to thank my supervisor, Mia Loccufier. If it wasn't for her, you wouldn't be holding this book. I would like to thank her for introducing me into the wonderful world of mechanical vibrations and for helping me throughout these six years. I have learned a tremendous amount of things, more than I had ever imagined possible.
Thanks also to my co-promotor, Dirk Aeyels, who has guided me through the nonlinear dynamics field and who handed me the opportunity of teaching Systems and signals, the benefits of which I'll carry with me for many years.
I would like to express my gratitude to Marc De Boom from DEME for supporting me with all the information needed regarding the dredging vessels. I even had the opportunity to visit some of them, a great experience.
The experimental work wouldn't have been possible without Wouter Ost who has had a great deal in simplifying my initial far-fetched designs.
The latter also holds for Joris Degrieck. Unfortunately, it lacked me time to implement some of his interesting ideas.
I would like to acknowledge Joachim Vanwalleghem for his contribution to the model reduction part.
I would also like to show my appreciation to the technicians Tony Boone and Stefaan Dhondt for skillfully manufacturing the nonlinear vibration absorber.
Thank you SYSTeMS Research Group! Mia, Dirk, Gert, René, Margot, Keivan, Mohammad, Herman, Nicolae, Erik, Jonathan, Filip, Fortunato, Filip and more recently Jasper, Arthur, Nathan, Rollando and I am sure I am forgetting some (please forgive me). You have made my stay at SYSTeMS a very pleasant one. Special thanks to my lunch buddies, Filip and Fortunato who have been a great support during my time at SYSTeMS, we sure had a good laugh! Also to Jonathan, the best roomy one could have hoped for. Erik, Keivan and Filip for solving my annoying computer problems, thank you very much!
Thanks to my friends for helping me throughout these six years. Freggels, I am back in full force! Stappers, Roel, Tom, Maarten, love you guys!

Without the all time support of my mum and dad I would not be writing this right now. Also Bart and Ania, looking forward to your wedding!
Last but not least, Joke, my love and Janne. You are all I've ever wished for. A hard day at work is forgotten the moment I open the door.

Janneke, kiekeboe ;)

Gent, oktober 2011
Frits Petit

Table of Contents

Nederlandse samenvatting –Summary in Dutch–

Een veel toegepaste manier om overmatige trillingsamplitudes te beperken is het aanhechten van een licht massa-veer-demper systeem, beter bekend als een dynamische trillingsdemper. Sinds de uitvinding hiervan door Frahm meer dan honderd jaar geleden, hebben onnoemelijk veel onderzoekers nieuwe types van trillingsdempers ontwikkeld in de hoop de klassieke trillingsdemper te verbeteren. Een zeer recent voorbeeld hiervan is het gebruik van sterk niet-lineaire veren die erin slagen om de trillingen in een veel ruimer frequentiegebied te onderdrukken.

In dit eindwerk wordt zowel ingegaan op het klassiek lineaire element als op zijn niet-lineaire tegenhanger. Hoewel reeds zeer veel onderzoek is gewijd aan beide elementen, zijn we erin geslaagd om het inzicht in verschillende aspecten sterk te verruimen. Vooral bij het praktisch implementeren is dit van cruciaal belang.

De thesis is opgedeeld in drie delen. Het eerste deel belicht de lineaire absorber, het tweede deel de niet-lineaire. In het derde deel worden de mogelijkheden van beide elementen met betrekking tot trillingsreductie onderzocht in een industriële toepassing.

Deel I: De lineaire dynamische trillingsdemper

Dit deel behandelt twee belangrijke concepten i.v.m. trillingsreductie van een lineair systeem met meerdere vrijheidsgraden onderhevig aan een harmonische excitatie, namelijk het verschuiven van resonanties en antiresonanties. Bekeken vanuit systeemtheoretische bril zijn dit de polen en de nullen van een transfert functie. In de context van trillingsreductie zijn resonanties te vermijden (hoge trillingsamplitudes) terwijl de antiresonanties gewenst zijn (zeer lage trillingsamplitudes). We bestuderen de mogelijkheid om resonanties en antiresonanties te beïnvloeden door het aanhechten van een ongedempt dynamische massa-veer element, i.e. de lineaire dynamische trillingsdemper.

Een belangrijke doelstelling is het crëeren van een zo groot mogelijke resonantievrije zone rond een problematische frequentie. Hierbij gaan we dieper in op de invloed die de locatie van de trillingsdemper heeft op de breedte van die zone. De aanhechtingslocatie wordt typisch gekozen volgens de eigenvector die hoort bij de desbetreffende trillingsmode. De eigenvector geeft immers weer hoe de energie van de trillingsmode verdeeld is over de structuur. De plaats wordt dan gekozen daar waar de energie maximaal is, dit om een zo groot mogelijke dynamische

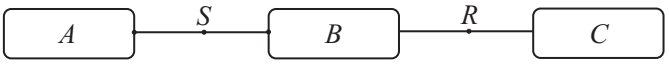

Figuur 1: Hoofdsystemen ontkoppeld in drie subsystemen A, B en C

tegenwerking van het element te betrachten.

Hier gaan we een stap verder en nemen we ook de invloed mee van de naburige trillingsmodi die belangrijker wordt naarmate de massa van de trillingsdemper groter wordt. We besluiten dat voor een even grote absorbermassa, een grotere resonantievrije zone bekomen wordt indien ter hoogte van de aanhechting van de trillingsdemper de naburige modi een lagere trillingsenergie hebben. De mode waarrond een resonantievrije zone gecreëerd wordt, moet dus op de aanhechtingsplaats domineren over zijn naburige modi. Een belangrijke indicatie hiervan zijn de naburige antiresonanties. Deze zijn immers voor elke locatie verschillend en geven aan hoe groot de resonantievrije zone maximaal kan worden.

Naast het verschuiven van resonanties biedt ook het verschuiven van antiresonanties interessante mogelijkheden. Antiresonanties blokkeren immers de harmonische excitatie waardoor sommige plaatsen op de structuur volledig gevrijwaard zijn van trillingen. Een belangrijke doelstelling is dan ook om de antiresonanties te verschuiven naar plaatsen op de structuur waar men geen trillingen wil. Meestal wordt dit probleem omgezet in het verschuiven van resonanties, echter dit zijn dan resonanties van een fictief systeem waardoor metingen niet aangewend kunnen worden.

Voor een groot aantal systemen kunnen we dit verhelpen door een ontkoppelingstechniek toe te passen zoals getoond in Fig. 1. Het initieel probleem, namelijk het plaatsen van antiresonanties van transfert functie H_{RS} voor het gehele systeem, wordt door deze opsplitsing omgezet in drie kleinere problemen, namelijk het plaatsen van antiresonanties voor de drie kleinere subsystemen. Bovendien biedt de ontkoppelingstechniek nog andere voordelen. Een eerste voordeel is dat de ontkoppeling extra inzicht verschaft in het bestaan van antiresonanties. Subsystemen A en C werken immers als ongedempte dynamische trillingsdempers met meerdere vrijheidsgraden. Met andere woorden, een groot deel van de antiresonanties van de transfert functie tussen R en S, worden gegeven door de resonanties van subsystemen A en C. Vermits dit fysische systemen zijn, hebben we als bijkomend voordeel dat metingen nu wel aangewend kunnen worden. Bovendien kunnen de resultaten bekomen i.v.m. de aanhechtingslocatie van de trillingsdemper ook hier aangewend worden.

Deel II: De niet-lineaire dynamische trillingsdemper

Een relatief nieuw element in de wereld van passieve trillingscontrole is de sterk niet-lineaire dynamische trillingsdemper. Sterk niet-lineair slaat op de veerkarakteristiek die in dit geval niet lineariseerbaar is. De belangrijkste eigenschap van dit type trillingsdempers is dat zij geen voorkeursfrequentie hebben. In principe zijn ze in

staat om trillingen met gelijk welke frequentie te reduceren, hetgeen een belangrijk voordeel is ten opzichte van hun klassieke lineaire tegenhanger.

Voor deze frequentierobuustheid moet echter een prijs betaald worden. Een efficiënte trillingsreductie is immers enkel mogelijk binnen een welbepaald gebied van trillingsamplitudes. Meerbepaald bestaat er een kritische energiedrempel die ervoor zorgt dat de trillingsdemper enkel goed werkt vanaf een bepaalde trillingsamplitude van het hoofdsysteem. Vermits dit een zeer belangrijk concept betreft aangaande de praktische implementatie van dit sterk niet-lineair element, wordt hierop in detail ingegaan. De belangrijkste bijdrage is een breed inzetbare dimensieloze aanpak die aangeeft hoe de trillingsdemper moet ontworpen worden om efficiënte trillingsreductie te realiseren.

Voor een dynamische demper met kubische niet-lineariteit aangehecht aan een lineaire oscillator (het hoofdsysteem) worden de bewegingsvergelijkingen in vrije responsie gegeven door

$$\begin{cases} m\ddot{x} + c\dot{x} + kx + c_{\text{na}}(\dot{x} - \dot{x}_{\text{na}}) + k_{\text{na}}(x - x_{\text{na}})^3 = 0 \\ m_{\text{na}}\ddot{x}_{\text{na}} + c_{\text{na}}(\dot{x}_{\text{na}} - \dot{x}) + k_{\text{na}}(x_{\text{na}} - x)^3 = 0 \end{cases} \tag{1}$$

waarbij m, c and k de massa, dempingsconstante en veerconstante van de lineaire oscillator voorstellen, terwijl subscript 'na' gebruikt wordt voor het niet-lineaire element. Het bestaan van een energiedrempel volgt uit Fig. 2 waar een kleine toename van de initiële snelheid van het hoofdsysteem ($\dot{x}(0) = 0.5$ t.o.v. $\dot{x}(0) = 0.6$) voor een sterke toename zorgt van de trillingsamplitude van de dynamische demper. Dit gaat bovendien gepaard met een veel snellere trillingsreductie van het hoofdsysteem.

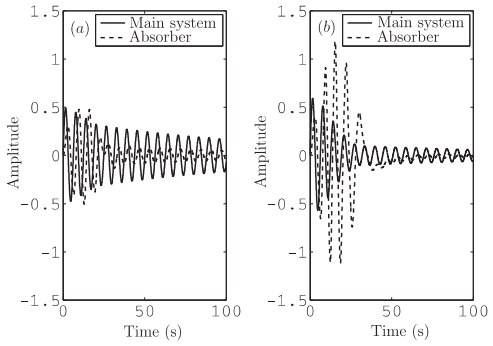

Figuur 2: Responsie van het hoofdsysteem en de niet-lineaire absorber ($m = 1, c = 0, k = 1, m_{na} = 0.05, c_{na} = 0.016, k_{na} = 0.067$*;* *(a)* $\dot{x}(0) = 0.5$, $x(0) = \dot{x}_{na}(0) = x_{na}(0) = 0$ *(b)* $\dot{x}(0) = 0.6$, $x(0) = \dot{x}_{na}(0) = x_{na}(0) = 0$

Om meer inzicht te verschaffen in het bestaan van een energiedrempel, hebben we het systeem gegeven in (1) onderworpen aan een grondige theoretische analyse. Een belangrijke benadering hierin is het verwaarlozen van termen in

$\epsilon = m_{\text{na}}/m << 1$. Dit zorgt ervoor dat het initiële systeem met twee vrijheidsgraden omgezet kan worden naar een systeem met één vrijheidsgraad dat bovendien omgevormd is tot een dimensieloos systeem

$$\frac{d^2 x_{\text{d}}}{d\tau^2} + \gamma x_{\text{d}}^3 = \sin(\tau + \phi) \tag{2}$$

met beginvoorwaarden

$$\begin{cases} x_d(0) & = \frac{(x_{\text{na}}(0) - x(0))\omega_0^2}{\sqrt{\omega_0^4 x(0)^2 + \omega_0^2 \dot{x}(0)^2}} \\ \frac{dx_d}{d\tau}(0) & = \frac{(\dot{x}_{na}(0) - \dot{x}(0))\omega_0}{\sqrt{\omega_0^4 x(0)^2 + \omega_0^2 \dot{x}(0)^2}}. \end{cases} \tag{3}$$

Een zeer groot voordeel van deze aanpak is dat de verschillende parameters k_{na}, m_{na}, ω_0 (eigenfrequentie van het hoofdsysteem), $x(0)$ and $\dot{x}(0)$ samengevoegd zijn in één dimensieloze parameter $\gamma > 0$

$$\gamma = \frac{k_{\text{na}}}{m_{\text{na}}} \frac{(x(0)^2 \omega_0^2 + \dot{x}(0)^2)}{\omega_0^4}. \tag{4}$$

Een bifurcatieanalyse van (2) met γ als bifurcatieparameter heeft aangetoond dat er een goede werking is van het niet-lineaire element (initieel in rust) vanaf een bepaalde waarde voor γ, namelijk

$$\gamma = \frac{k_{\text{na}}}{m_{\text{na}}} \frac{(x(0)^2 \omega_0^2 + \dot{x}(0)^2)}{\omega_0^4} > \gamma_c \approx 0.18 \tag{5}$$

Dit betekent dat het bestaan van een energiedrempel uitgebreid kan worden naar een meer algemene parameterdrempel. Met andere woorden, elke parameter vervat in γ (met inbegrip van de energie in de vorm van beginvoorwaarden) heeft zijn eigen drempelwaarde. We kunnen dus bepalen welke gebieden in de parameterruimte efficiënte trillingsreductie opleveren en welke niet. Naar een praktische implementatie toe is dit cruciale informatie. Bovendien zijn we er ook in geslaagd om bovenstaande eenvoudige analyse uit te breiden naar absorbers met niet-kubische niet-lineariteit, alsook naar niet-lineaire hoofdsystemen en naar harmonisch aangedreven lineaire hoofdsystemen.

We hebben de bovengenoemde theoretische resultaten ook experimenteel gevalideerd door een niet-lineaire dynamische demper te implementeren in een bestaande proefstand rond torsietrillingen, getoond op Fig. 3. Een as van verenstaal doet dienst als lineaire stijfheid van het hoofdsysteem. De inertie wordt verzorgd door vier schijven, hoewel voor de experimenten slechts één schijf gebruikt is zodat een systeem met één vrijheidsgraad bekomen wordt. De torsietrillingen van het hoofdsysteem worden opgewekt door een servomotor. De niet-lineariteit van de trillingsdemper (in blauw) wordt gerealiseerd door middel van een tweezijdig ingeklemde staaldraad (Fig. 4).

We hebben zowel experimenten in transiënt gedrag (motorimpuls) als in regimegedrag (sinusexcitatie aan resonantiefrequentie) doorgevoerd. In beide gevallen

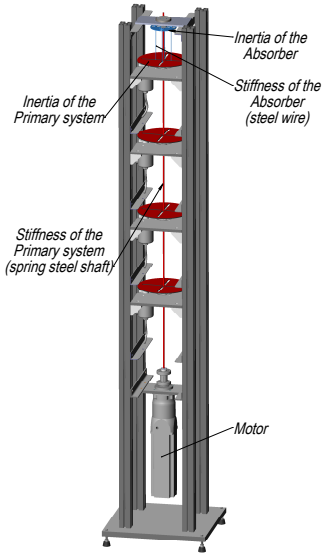

Figuur 3: Proefstand voor torsietrillingen - Hoofdsysteem (rood) en niet-lineaire absorber (blauw)

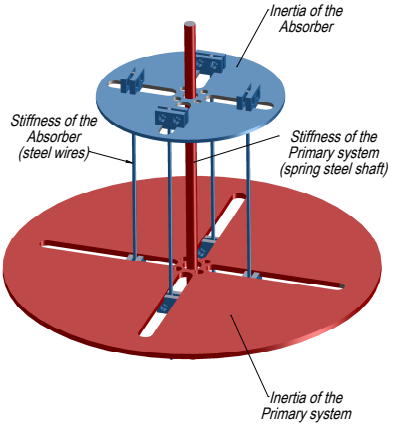

Figuur 4: Proefstand voor torsietrillingen - detail niet-lineaire absorber (blauw)

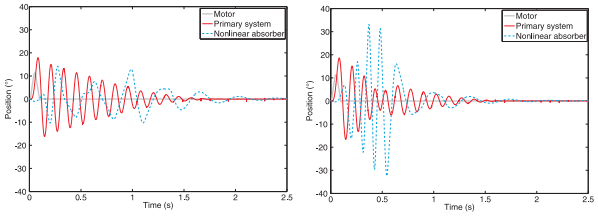

Figuur 5: Impulsresponsie van het hoofdsysteem (rood) en niet -lineaire trillingsdemper (blauw) - links: onder energiedrempel, rechts: boven energiedrempel

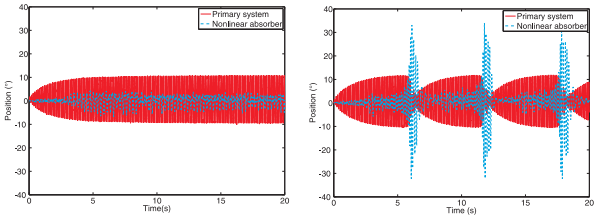

Figuur 6: Regimeresponsie van het hoofdsysteem (rood) en niet -lineaire trillingsdemper (blauw) - links: onder energiedrempel, rechts: boven energiedrempel

zorgt een kleine toename van de excitatieamplitude voor een sterke toename van de responsie van het niet-lineaire element zoals duidelijk naar voor komt in Figuren 5-6. Het verschil in excitatieamplitude onder en boven de energiedrempel is in beide gevallen minder dan 5%.

Deel III: Naar een industriële toepassing

In het laatste deel van dit proefschrift bekijken we wat de mogelijkheden zijn van dynamische trillingsdempers in een industriële toepassing. De meeste structuren worden in de praktijk gemodelleerd met een eindige elementen model (met zeer veel vrijheidsgraden) dat echter meestal te gedetailleerd is met het oog op trillingscontrole. Een eerste belangrijke stap is dan ook het reduceren van dit complexe model tot een model dat in staat is om accuraat het laagfrequent gedrag van het hoofdsysteem weer te geven. De trillingsdempers zullen hierop immers afgesteld worden.

Een techniek die toegepast wordt in zeer veel softwarepakketten is de reductietechniek van Guyan. Hierbij wordt de totale set van vrijheidsgraden opgedeeld in master coördinaten q_m en slave coördinaten q_s

$$\begin{bmatrix} M_{mm} & M_{ms} \\ M_{sm} & M_{ss} \end{bmatrix} \begin{Bmatrix} \ddot{q_m} \\ \ddot{q_s} \end{Bmatrix} + \begin{bmatrix} K_{mm} & K_{ms} \\ K_{sm} & K_{ss} \end{bmatrix} \begin{Bmatrix} q_m \\ q_s \end{Bmatrix} = \begin{Bmatrix} f_m \\ 0 \end{Bmatrix}. \tag{6}$$

De slave coördinaten worden verondersteld zeer weinig invloed te hebben op het laagfrequent gedrag zodat deze met een goede nauwkeurigheid weggelaten kunnen

worden door volgende transformatie door te voeren

$$M_m = S_f^T M_n S_f \quad K_m = S_f^T K_n S_f \tag{7}$$

met

$$\begin{bmatrix} q_m \\ q_s \end{bmatrix} = \begin{bmatrix} I \\ -K_{ss}^{-1} K_{sm} \end{bmatrix} \{q_m\} = S_f \{q_m\}. \tag{8}$$

Een belangrijk vraag binnen deze reductietechniek is dan ook welke coördinaten als slaves gekozen moeten worden.

De klassieke selectietechniek is een sequentiële eliminatiemethode (SEM) waarbij telkens één slave coördinaat wordt geselecteerd en geëlimineerd totdat enkel de master coördinaten overblijven. De methode start met het bepalen van de maximumwaarde voor k_{ii}/m_{ii} met k_{ii} en m_{ii} diagonale elementen van de volledige n bij n K_n en M_n matrices. De overeenkomstige coördinaat wordt geselecteerd als slave en geëlimineerd via Guyan reductie zodat K_n en M_n omgezet worden in $n-1$ bij $n-1$ matrices. De volgende slave wordt dan geselecteerd op basis van de maximumwaarde k_{ii}/m_{ii} van de gereduceerde K_{n-1} en M_{n-1} matrices. Uiteindelijk blijven enkel de master coördinaten over. Echter, voor FEM modellen met zeer veel vrijheidsgraden is dit proces zeer rekenintensief aangezien het aantal iteraties dan zeer groot wordt. Het aantal master coördinaten is immers typisch veel kleiner dan het aantal slaves. Bovendien worden de matrices na elke reductiestap niet alleen kleiner, maar hun densiteit wordt ook veel hoger waardoor de geheugenvereisten en rekentijd alsmaar hoger oplopen.

Om dit probleem te vermijden, is er een algoritme ontwikkeld dat de master coördinaten selecteert in plaats van de slaves zodat veel minder iteraties doorlopen moeten worden. In plaats van op basis van k_{ii}/m_{ii} te kiezen zoals bij de selectie van de slaves, worden de masters gekozen op basis van de diagonaalelementen van $|K_{ss}^{-1} M_{ss}|$. De component die overeenkomt met het grootste diagonaalelement van $|K_{ss}^{-1} M_{ss}|$ wordt weerhouden als master waarbij in een eerste stap K_{ss} en M_{ss} gelijk zijn aan de initiële K_n en M_n matrices. Vermits het aantal iteraties drastisch afneemt, kunnen rekentijd en geheugenvereisten significant verminderd worden.

Het ontwikkelde algoritme is met succes toegepast in een industriële omgeving, met name de aandrijflijn van een baggerschip die bestaat uit een dieselmotor, een baggerpomp, een generator en een propeller. Deze hoofdelementen zijn verbonden met onder andere flexibele koppelingen en tandwielkasten die vroegtijdige schade ondervinden ten gevolge van overmatige torsietrillingen. Een belangrijk storend koppel wordt veroorzaakt door de dieselmotor. Hier gaan we echter dieper in op de kortstondige excitaties die de aandrijflijn doen trillen. Voorbeelden hiervan zijn het aan- en afkoppelen van schakelbare koppelingen, lastwissels op de generator en schokbelastingen ter hoogte van de baggerpomp. Het gevolg van dit soort excitaties is een hevige torsietrilling waarin meerdere trillingsmodi een aandeel hebben, een uitstekende toepassing om de mogelijkheden af te toetsen van de sterk niet-lineaire dynamische trillingsdemper.

De afstelling van de parameters van het niet-lineaire element (kubische niet-lineariteit) gebeurt volgens formule (5) uit Deel II. De performantie van dit element

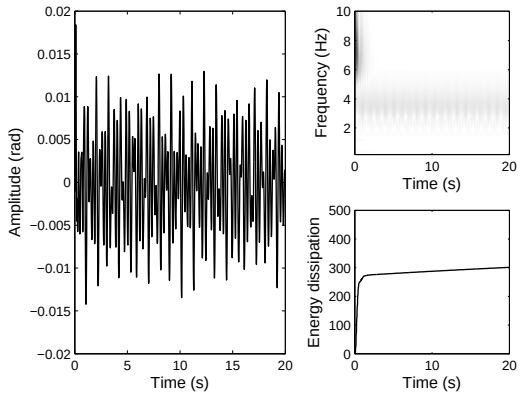

Figuur 7: Trillingsreductie ter hoogte van de tandwielkast - lineaire trillingsdemper ($m_a = 200\ kg\ m^2$)

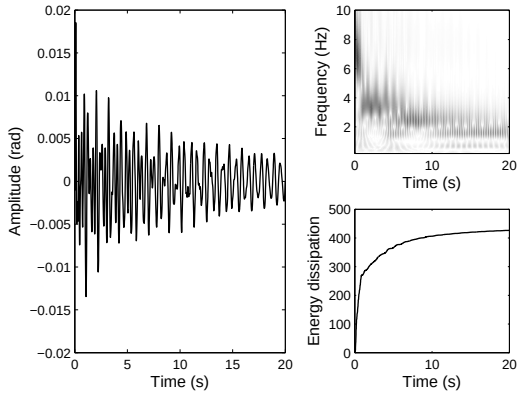

Figuur 8: Trillingsreductie ter hoogte van de tandwielkast - niet-lineaire trillingsdemper ($m_{na} = 200\ kg\ m^2$)

wordt vergeleken met die van het lineaire element waarvan de afstelling gebeurt volgens klassieke methodes. De simulaties in Figuren 7 en 8 tonen aan de niet-lineaire trillingsdemper een sterkere trillingsreductie realiseert dan zijn lineaire tegenhanger. In de beginfase slagen beiden in een snelle reductie van de trillingsenergie vervat in één trillingsmode. De energiedissipatie van de lineaire valt hierna stil. De niet-lineaire echter slaagt erin om ook de trillingsenergie van de overige modi te reduceren, maar de reductie verloopt jammer genoeg veel trager. Verder verhogen van de absorbermassa kan dit probleem verhelpen zoals aangetoond in Fig. 9. De praktische haalbaarheid van een grotere massa blijft wel een open vraag. Bovendien is het voor een diepgaande studie i.v.m. de bruikbaarheid van

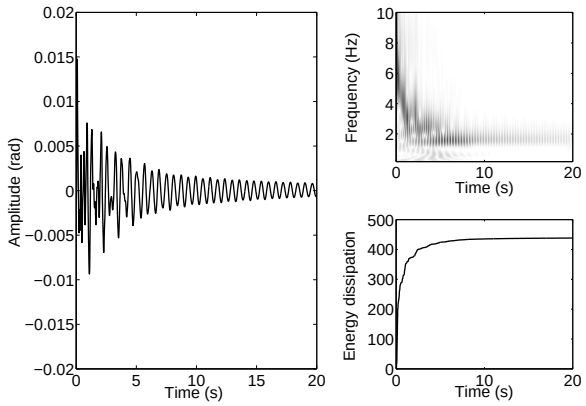

Figuur 9: Trillingsreductie ter hoogte van de tandwielkast - niet-lineaire trillingsdemper ($m_{na} = 800\ kg\ m^2$)

het niet-lineaire element, vereist dat onder andere het excitatiekoppel van de diesel, de snelheidsregelaar en de demping van het hoofdsysteem in rekening gebracht worden.

English summary

A very popular approach to mitigate excessive vibration amplitudes is to add small spring-mass systems to the structure, known as dynamic vibration absorbers or tuned mass dampers. Since their invention by Frahm, many researchers have tried to develop new types of vibration absorbers that outperform the classical ones. A recent example is the use of strongly nonlinear vibration absorbers which are believed to feature a larger frequency robustness compared to their linear counterpart.

In this dissertation, an improved insight in many different aspects of both the linear and the strongly nonlinear vibration absorber is developed. We have subdivided the thesis into three parts. Part I deals with the linear vibration absorber, Part II with the nonlinear vibration absorber. Part III exemplifies the use of vibration absorbers in a real-life industrial application.

Part I: The linear vibration absorber

This part deals with two concepts offering great opportunities when it comes to vibration reduction of a linear MDOF primary system under harmonic load, namely relocating resonances and antiresonances. In a system's theory setting, resonances and antiresonances correspond to the poles and zeros of a transfer function. For the vibration control engineer, resonances (high vibration amplitudes) are to be avoided while on the other hand antiresonances (zero vibration amplitudes) are desired. We study the possibilities of relocating resonances and antiresonances by attaching Frahm's undamped vibration absorber.

An important objective in vibration control is to create a resonance free zone or spectral gap around a troublesome frequency by attaching a vibration absorber. More precisely, the influence of the attachment location on the width of the spectral gap is investigated. Typically, the attachment location is determined according to the eigenvector of the troublesome vibration mode which provides the spatial distribution of the vibration energy within a single vibration mode. This *single mode approach* does however not take into account the influence of the neighboring vibration modes which becomes important for larger absorber masses and closely spaced modes.

Here, the influence of the neighboring vibration modes is revealed. For an a priori chosen absorber mass, it is shown that the resonances are further shifted away from the resonant excitation frequency when the vibration energy of the neighboring modes is low at the attachment location. In other words, the frequency robustness of the device is larger when at the attachment location, the vibration

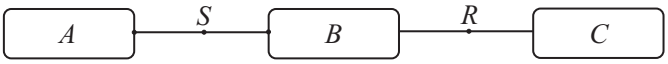

Figure 10: Decoupling the main system into three subsystems A, B and C

mode to which the absorber is tuned, is dominating over its neighboring modes. An important indication of this dominance is shown to be given by the neighboring antiresonances. These antiresonances are different for each attachment location and provide the boundaries of the shift of the resonances for $m_{\mathrm{a}} \rightarrow \infty$. As a result, a larger gap between the troublesome vibration mode and its neighboring antiresonances is a clear indication of an improved attachment location for larger values of m_{a}.

The second important means in reducing vibration amplitudes is handed by the antiresonances which define points of zero vibration on the structure. Hence, the question arises how they can be relocated to the desired location. Usually, the problem of assigning antiresonances is transformed into assigning resonances of a virtual system. Here, we use a substructure coupling technique which divides the primary system into three subsystems coupled at R and S as shown in Fig. 10. Besides reducing the size of the problem, this subdivision has two main advantages. An improved insight is obtained in how antiresonances of the transfer function between R and S are created. Indeed, it is shown that subsystems A and C work as MDOF vibration absorbers. As a result, the assignment of antiresonances can be rewritten as the assignment of resonances which in this case belong to physical systems instead of virtual ones. This allows to assign antiresonances by means of measurements, a huge advantage compared to classical methods. Moreover, as we are again dealing with resonances, the above mentioned results regarding the attachment location of the absorber can be reused.

Part II: The nonlinear vibration absorber

A relatively new element in passive vibration control is the strongly nonlinear vibration absorber, i.e. it features a nonlinearizable stiffness characteristic. The key feature of these type of absorbers is their lack of a preferential frequency, i.e. they can reduce vibrations at virtually any frequency. This provides a great advantage over the classical linear absorbers which are typically limited to a single frequency.

The most important downside is their amplitude dependency, i.e. they only succeed in achieving efficient vibration reduction in a well-defined vibration amplitude region. More precisely, a critical *energy threshold* exists which means that efficient vibration reduction is only possible above a minimum amount of input energy into the primary system. Because this defines a crucial concept in the design procedure of nonlinear vibration absorbers, we have studied it into detail. The main contribution is a dimensionless approach which enables to determine the boundaries between weak and strong vibration reduction for a wide variety of systems.

For a cubic nonlinear vibration absorber attached to a linear oscillator (LO)

subject to initial conditions, the equations of motion become

$$\begin{cases} m\ddot{x} + c\dot{x} + kx + c_{\text{na}}(\dot{x} - \dot{x}_{\text{na}}) + k_{\text{na}}(x - x_{\text{na}})^3 = 0 \\ m_{\text{na}}\ddot{x}_{\text{na}} + c_{\text{na}}(\dot{x}_{\text{na}} - \dot{x}) + k_{\text{na}}(x_{\text{na}} - x)^3 = 0 \end{cases} \tag{9}$$

where m, c and k denote the mass, damping and stiffness of the linear oscillator, while subscript 'na' is used for the nonlinear absorber. The existence of the energy threshold is evidenced by Fig. 11 where a small increase in the LO's initial velocity, causes a large increase in the absorber's response and its ability to dissipate vibrational energy.

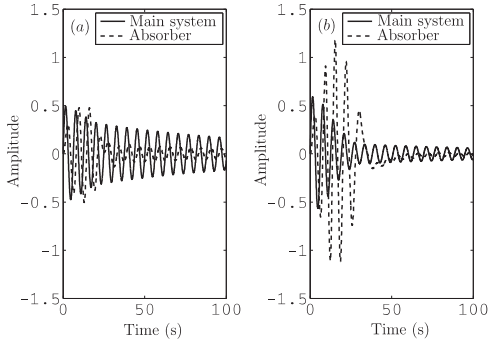

Figure 11: Main system and cubic absorber response ($m = 1, c = 0, k = 1, m_{na} = 0.05, c_{na} = 0.016, k_{na} = 0.067$); (a) $\dot{x}(0) = 0.5$, $x(0) = \dot{x}_{na}(0) = x_{na}(0) = 0$ (b) $\dot{x}(0) = 0.6$, $x(0) = \dot{x}_{na}(0) = x_{na}(0) = 0$

To improve insight in this remarkable behavior, an approximate theoretical analysis has been performed. The key approximation is neglecting terms in $\epsilon = m_{\text{na}}/m << 1$ which allows to reduce the initial 2DOF system of (9) to a SDOF system in dimensionless form:

$$\frac{d^2x_{\text{d}}}{d\tau^2} + \gamma x_{\text{d}}^3 = \sin(\tau + \phi) \tag{10}$$

with initial conditions

$$\begin{cases} x_d(0) & = \frac{(x_{\text{na}}(0) - x(0))\omega_0^2}{\sqrt{\omega_0^4 x(0)^2 + \omega_0^2 \dot{x}(0)^2}} \\ \frac{dx_d}{d\tau}(0) & = \frac{(\dot{x}_{na}(0) - \dot{x}(0))\omega_0}{\sqrt{\omega_0^4 x(0)^2 + \omega_0^2 \dot{x}(0)^2}}. \end{cases} \tag{11}$$

The main advantage of (10) is that k_{na}, m_{na}, the LO's natural frequency ω_0, $x(0)$ and $\dot{x}(0)$ are joined into one dimensionless parameter $\gamma > 0$

$$\gamma = \frac{k_{\text{na}}}{m_{\text{na}}} \frac{(x(0)^2\omega_0^2 + \dot{x}(0)^2)}{\omega_0^4}. \tag{12}$$

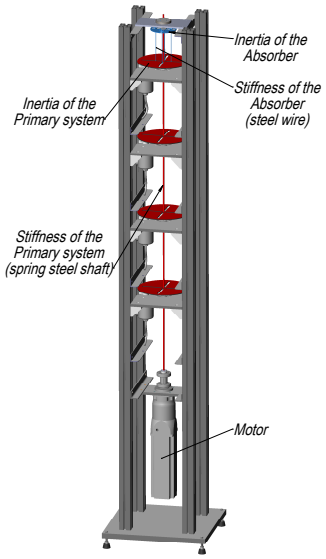

Figure 12: Torsional vibration setup - Primary system and absorber

Using γ as the bifurcation parameter in (10), we have shown that the initial energy threshold value of system (9), is transformed into a threshold value for γ

$$\gamma = \frac{k_{\text{na}}}{m_{\text{na}}} \frac{(x(0)^2\omega_0^2 + \dot{x}(0)^2)}{\omega_0^4} > \gamma_c \approx 0.18 \tag{13}$$

As a result, the energy threshold concept is extended to a more general parameter threshold where each parameter (including the initial energy) is featuring its own threshold value. In other words, by using Eq. (13) we can determine which subset of the parameter space is capable of efficient vibration reduction and which is not, crucial information when practically implementing the nonlinear absorber. Moreover, the same approach can be extended to cope with general nonlinear spring characteristics, nonlinear main systems and forced LO.

To experimentally verify the different concepts, we have implemented a nonlinear absorber into a torsional vibration setup as shown in Fig. 12. The primary system, excited by a servo motor, consists of a spring steel shaft with attached to it up to four inertia disks. In the experiments only one disk is used such that a SDOF system is obtained. The nonlinearity of the absorber is achieved using a clamped-clamped steel wire, which approximately acts as a cubic nonlinear spring. The threshold phenomena were captured both in transient and steady state conditions as shown by Figs. 14-15. In both cases, the difference in excitation amplitude is less than 5 $\%$.

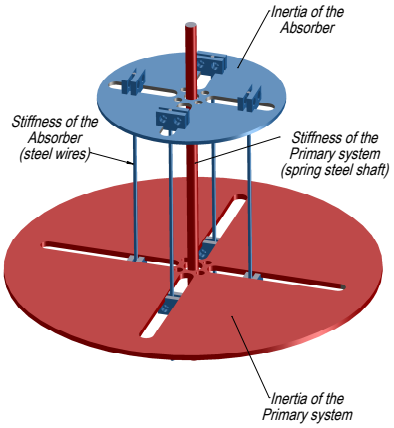

Figure 13: Torsional vibration setup - Primary system and absorber

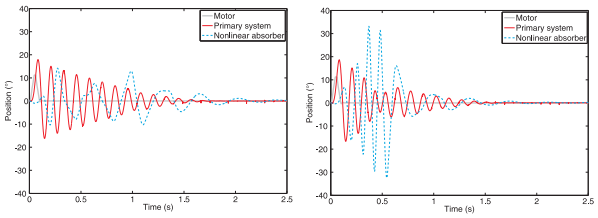

Figure 14: Primary system and absorber response to a motor impulse - below (left) and above (right) energy threshold

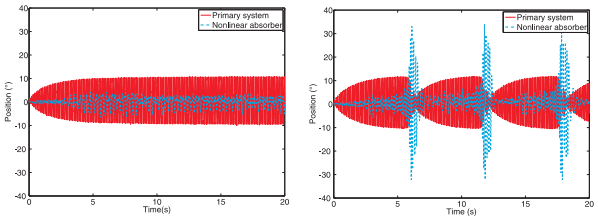

Figure 15: Steady state response of the primary system and the absorber - below (left) and above (right) energy threshold

Part III: Towards an industrial application

The last part of this dissertation is concerned with the feasibility of using vibration absorbers in an industrial application. An important step towards the design of a vibration absorber is reducing the generally complex FEM model of the primary system into a system of manageable size able to represent the low frequency behavior.

A very popular technique used in many software packages is the Guyan reduction technique where the entire set of coordinates is divided into master coordinates q_m and slave coordinates q_s

$$\begin{bmatrix} M_{mm} & M_{ms} \\ M_{sm} & M_{ss} \end{bmatrix} \begin{Bmatrix} \ddot{q_m} \\ \ddot{q_s} \end{Bmatrix} + \begin{bmatrix} K_{mm} & K_{ms} \\ K_{sm} & K_{ss} \end{bmatrix} \begin{Bmatrix} q_m \\ q_s \end{Bmatrix} = \begin{Bmatrix} f_m \\ 0 \end{Bmatrix}. \tag{14}$$

The slave coordinates are assumed to have a negligible effect on the low frequency behavior such that they can be eliminated by applying the following transformation

$$M_m = S_f^T M_n S_f \quad K_m = S_f^T K_n S_f \tag{15}$$

with

$$\begin{bmatrix} q_m \\ q_s \end{bmatrix} = \begin{bmatrix} I \\ -K_{ss}^{-1} K_{sm} \end{bmatrix} \{q_m\} = S_f \{q_m\}. \tag{16}$$

A crucial step is the selection of the slave coordinates. A widely implemented approach is the numerical algorithm where the slave DOFs are condensed out one by one leaving only the master coordinates. This method starts by selecting the maximum k_{ii}/m_{ii} where k_{ii} and m_{ii} are diagonal entries of the full n by n K_n and M_n matrices. The corresponding degree of freedom is selected as a slave coordinate and condensed out by Guyan reduction, transforming K_n and M_n into $n-1$ by $n-1$ matrices. The cycle then recommences by selecting the maximum k_{ii}/m_{ii} of the reduced K_{n-1} and M_{n-1} matrices. In this way, the slave degrees of freedom are eliminated one by one leading to a set of master degrees of freedom. For large mechanical systems however, this sequential elimination method (SEM) becomes very computationally expensive.

To overcome this problem, a new algorithm is proposed which sequentially selects the master DOFs, i.e. a sequential selection method (SSM). In this method, the component that corresponds to the largest diagonal entry of $|K_{ss}^{-1} M_{ss}|$ is retained as a master in each step where K_{ss} and M_{ss} are initially equal to the full n by n K_n and M_n matrices. Because the number of master DOFs is usually much smaller than the number of slave DOFs, a significant time reduction is achieved. Moreover, both methods are based on the exact same principles resulting in a comparable accuracy.

The developed algorithm has been successively applied in an industrial environment, namely the drive line of a hopper dredger which consists of a diesel engine driving a dredge pump, a propeller and a generator. In between these main elements are flexible couplings and gearboxes which suffer from troublesome torsional vibrations. Although these torsional vibrations also arise from steady state excitation

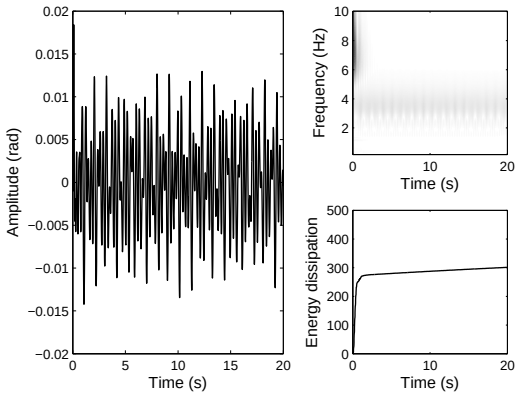

Figure 16: Multimodal response at the gearbox with linear absorber ($m_a = 200$ kg m^2)

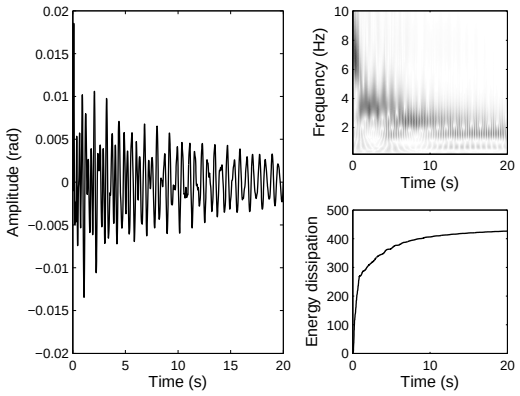

Figure 17: Multimodal response at the gearbox with nonlinear absorber ($m_{na} = 200$ kg m^2)

(e.g. from the diesel engine), only transient loads are considered because the hopper dredger is, more than any other ship, subject to highly frequent changes both in configuration and load. Many of these transient loads initiate a multimodal response which calls for the application of a strongly nonlinear vibration absorber.

The parameters of the nonlinear absorber (with cubic nonlinearity) are determined according to Eq. (13) from Part II. Using the same absorber mass, simulations shown in Figs. 16 and 17 demonstrate that the cubic spring absorber outperforms the classical linear absorber. In the initial phase both absorbers succeed in reducing the energy of one vibration mode which rapidly decreases due to a beating phenomenon. After this initial phase, the linear absorber becomes ineffective. The nonlinear absorber however, succeeds in reducing the energy of the remaining vibration modes as well. This happens in a sequential manner through so called

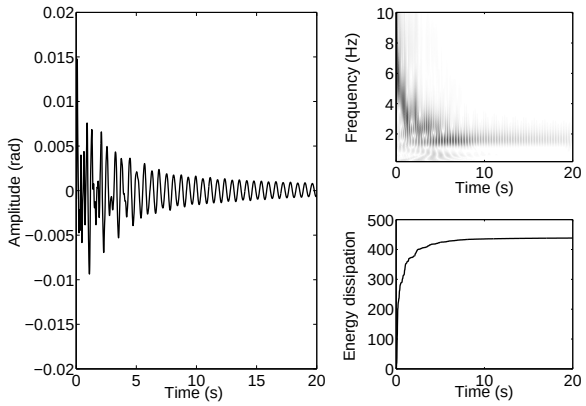

Figure 18: Multimodal response at the gearbox with nonlinear absorber ($m_{na} = 800\ kg\ m^2$)

resonance capture cascades which unfortunately exhibit a much slower vibration reduction. Further increasing the absorber mass improves this situation (Fig. 18), but the question remains whether such a large mass is practically implementable. For a detailed feasibility study one should also take into account the excitation of the diesel engine, the speed governor and the primary system's damping.

1 Introduction

1.1 Problem statement

Decades ago, mechanical vibrations were nothing more than a troublesome side-effect hampering the main functioning of a machine or structure. Nowadays, with the ever increasing demands of reliability, accuracy, comfort and noise reduction, minimizing mechanical vibrations has become an essential part of the design stage in many different areas of engineering.

Unfortunately, despite these efforts, vibration problems are still encountered in many applications like transportation, construction and rotating machinery. There are several reasons why unexpected failures occur after the design stage. The most obvious one, notwithstanding the huge advances in finite element method (FEM) modelling, is a lack of accuracy of the underlying theoretical model. Another reason is deviating from the initially intended operating range of the machinery, e.g. by increasing the speed range. Sometimes, the structure encounters excitation sources not foreseen in the design. A very well-known example is the recently built Millennium bridge in London (finished in 2000) where the crowd started *wobbling* along with the bridge (now nicknamed the ”Wobbly bridge”), thereby creating a so called synchronous lateral excitation not taken into account in the design stage.

When facing damaging vibrations, engineers aim for a simple, low cost and efficient solution. In many cases, like the Millennium bridge, dynamic vibration absorbers meet these requirements. Dynamic vibration absorbers or tuned mass dampers are small mass-spring-damper elements locally attached to the structure

designed to dissipate excessive vibration energy. As opposed to structural modification where structural parameters like damping and stiffness are altered [1], dynamic absorbers are extra mechanical elements attached to the structure which itself remains unaltered. A second important difference with structural modification is that extra degrees of freedom (DOF) are added to the structure.

Vibration absorbers and structural modification fit in the framework of passive control, i.e. no extra energy is added to the system. The opposite of passive control is active control that does require an energy source. The vibration amplitudes (measured with a sensor) are minimized by creating counteracting forces (with an actuator) using a well-defined control strategy [2]. The advantage is that a wide variety of counteracting measures can be realized. The drawback of applying active control is added cost (it requires an energy source) and stability issues.

The high energy requirement of active control can be circumvented by using semi-active control, also denoted as adaptive-passive control [3]. Although the semi-active approach requires a feedback control as well, it is only used to alter the stiffness and damping values of the absorber resolving in this way some mistuning issues. The main advantage is that this can be achieved with a much smaller amount of energy. The practical implementation however, typically using electro- and magneto-rheological fluid dampers, is still a problem. For a review on the existing implementations, see [4].

A schematic overview of the different vibration control techniques is given in Fig. 1.1. Active and semi-active control undoubtedly offer great opportunities regarding vibration reduction. However, many researchers throughout the world (including the author) are still trying to squeeze out all the possibilities of passive vibration control and more specifically of dynamic vibration absorbers. These efforts have resulted in an enormous amount of papers each describing different tuning procedures and optimization techniques depending on the type of primary system, the type of excitation and the type of vibration absorber configuration. Describing all the existing techniques here would lead us too far off and we would like to refer the interested reader to [5], [6], [7] and [8] for a detailed overview. Instead, the key developments in the history of dynamic vibration absorbers are outlined in the next section.

1.2 Milestones in the development of dynamic vibration absorbers

”Device for Damping Vibrations of Bodies”, the patent claimed by Frahm in 1909 opened a fascinating field of engineering [9]. His idea was beautifully simple. When a structure is suffering from heavy vibrations, don’t alter the structure itself. No, instead add an extra *device* to it. This passive device, i.e. no energy source is required,

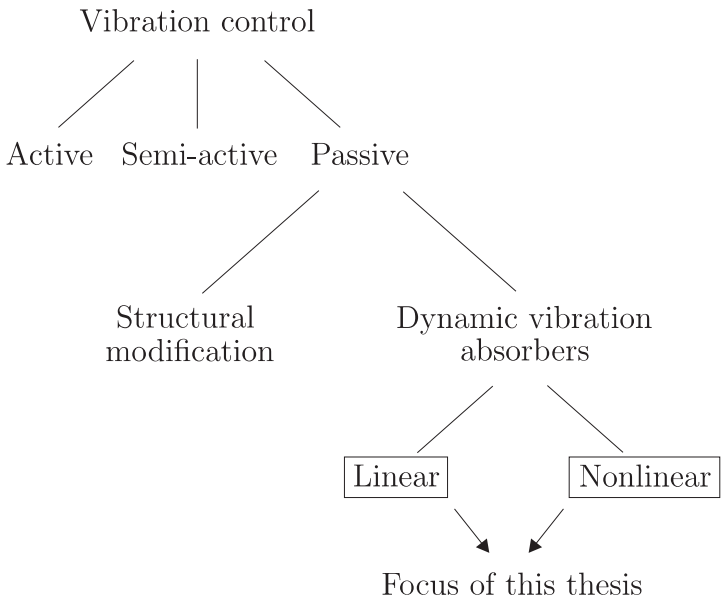

Figure 1.1: Vibration control - Overview

is nowadays known under several names: dynamic vibration absorber (DVA), tuned mass damper (TMD), attached oscillator and tuned vibration absorber and has become indispensable in many engineering applications such as transportation, machinery and earthquake engineering.

Since its invention more than 100 years ago, an overwhelming amount of research has been conducted to optimize the vibration controlling capacities of this simple, low cost yet ingenious device. Of course, the main idea sounds very intriguing. Not only is the structure itself left unaltered, but the added device may also be very lightweight. How this is possible is explained hereafter.

1.2.1 The undamped vibration absorber

The vibrating structure is denoted as the primary or main system and is modelled as an undamped single-degree-of-freedom (SDOF) spring-mass system with mass m and stiffness coefficient k as shown in Fig. 1.2. Periodically forcing the primary system at its natural frequency $\omega_0 = \sqrt{k/m}$ creates a resonance condition and theoretically drives the vibration amplitude to infinity. To resolve the resonance condition, a dynamic vibration absorber is attached to the primary system (Fig. 1.2). The absorber is also modelled as an undamped spring-mass system, but with a much smaller mass, i.e. the mass ratio $\mu = m_\mathrm{a}/m << 1$ (typically around 5%). The equations of motion of the resulting 2DOF system (initially at rest) are given

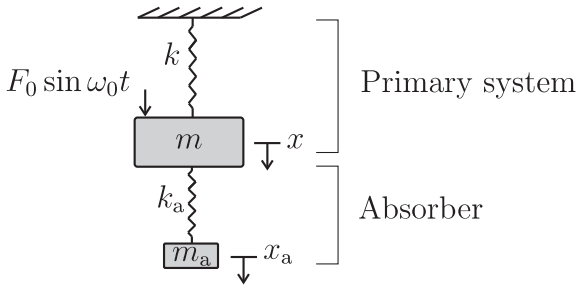

Figure 1.2: An undamped dynamic vibration absorber attached to an undamped SDOF primary system

by

$$\begin{cases} m\ddot{x} + kx + k_\mathrm{a}(x - x_\mathrm{a}) = F_0 \sin \omega_0 t \\ m_\mathrm{a}\ddot{x}_\mathrm{a} + k_\mathrm{a}(x_\mathrm{a} - x) = 0 \end{cases} \tag{1.1}$$

or by introducing $\omega_\mathrm{a} = \sqrt{k_\mathrm{a}/m_\mathrm{a}}$ rewritten as

$$\begin{cases} \ddot{x} + \omega_0^2 x + \mu\omega_\mathrm{a}^2(x - x_\mathrm{a}) = \frac{F_0}{m} \sin \omega_0 t \\ \ddot{x}_\mathrm{a} + \omega_\mathrm{a}^2(x_\mathrm{a} - x) = 0. \end{cases} \tag{1.2}$$

The resulting steady state vibration amplitudes of the primary system and the absorber become

$$x(t) = \frac{\omega_\mathrm{a}^2 - \omega_0^2}{m\Delta(\omega^2)} F_0 \sin \omega_0 t \tag{1.3}$$

$$x_\mathrm{a}(t) = \frac{\omega_\mathrm{a}^2}{m\Delta(\omega^2)} F_0 \sin \omega_0 t \tag{1.4}$$

with $\Delta(\omega^2)$ defined as

$$\Delta(\omega^2) \triangleq \omega^4 - \left[\frac{k_\mathrm{a}}{m_\mathrm{a}} + \frac{k + k_\mathrm{a}}{m}\right] \omega^2 + \frac{k k_\mathrm{a}}{m m_\mathrm{a}} \tag{1.5}$$

The working principle of the absorber can be explained by Eq. (1.3) which shows that correctly tuning the absorber, i.e.

$$\omega_a = \omega_0 \tag{1.6}$$

forces the vibration amplitude of the primary system to zero. Since no energy dissipation is present, this means that the energy must be completely localized to the attached dynamic element. Indeed, for $\omega_a = \omega_0$, Eqs. (1.4) -(1.5) show that its vibration amplitude is given by

$$x_\mathrm{a}(t) = -\frac{F_0}{k_\mathrm{a}} \sin \omega_0 t. \tag{1.7}$$

This vibration causes a force

$$k_{\mathrm{a}} x_{\mathrm{a}}(t) = -F_0 \sin \omega_0 t \tag{1.8}$$

which is equal and opposite in phase to the force exerted upon the primary system. In other words, the motion of the dynamic vibration absorber completely neutralizes the excitation force $F_0 \sin \omega_0 t$ achieving in this way a perfect vibration reduction.

This 'perfect' vibration reduction however, needs to be nuanced by discussing some drawbacks of the lightweight device. A key parameter in the discussion is the mass of the absorber. Ideally, the mass is chosen as small as possible. This however has two important consequences. The first one is revealed by Eq. (1.7) and rewritten here as

$$x_{\mathrm{a}}(t) = -\frac{F_0}{k_{\mathrm{a}}} \sin \omega_0 t \tag{1.9}$$

$$= -\frac{1}{\mu} \frac{F_0}{k} \sin \omega_0 t \tag{1.10}$$

which shows that the vibration amplitude is inversely proportional to the mass ratio $\mu = m_{\mathrm{a}}/m$. Consequently, a smaller mass m_{a} results in a larger vibration amplitude of the absorber. Besides a larger required rattle space, fatigue problems may arise. The second and most important drawback of using a small mass is clarified in Fig. 1.3 showing the amplitude Bode plot of the primary system. For a small mass ratio (e.g. $\mu = 0.05$), the new resonance peaks are very close to the initial one at ω_0. Hence, a slight deviation of the excitation frequency can cause a new resonance condition. Increasing the absorber mass ratio (e.g. $\mu = 0.25$) shifts the resonance peaks further away from ω_0 attaining in this way a larger frequency robustness. In practice however, the absorber mass is limited such that other means of resolving this frequency robustness issue must be sought.

1.2.2 The damped vibration absorber

The most natural solution is to include damping in the device as displayed in Fig. 1.4. This changes the equations of motion to

$$\begin{cases} m\ddot{x} + kx + c_{\mathrm{a}}(\dot{x} - \dot{x}_{\mathrm{a}}) + k_{\mathrm{a}}(x - x_{\mathrm{a}}) = F_0 \sin \omega_0 t \\ m_{\mathrm{a}}\ddot{x}_{\mathrm{a}} + c_{\mathrm{a}}(\dot{x}_{\mathrm{a}} - \dot{x}) + k_{\mathrm{a}}(x_{\mathrm{a}} - x) = 0. \end{cases} \tag{1.11}$$

By introducing $\zeta_{\mathrm{a}} = \frac{c_{\mathrm{a}}}{2m_{\mathrm{a}}\omega_{\mathrm{a}}}$, (1.11) is rewritten as

$$\begin{cases} \ddot{x} + \omega_0^2 x + 2\mu\omega_{\mathrm{a}}\zeta_{\mathrm{a}}(\dot{x} - \dot{x}_{\mathrm{a}}) + \mu\omega_{\mathrm{a}}^2(x - x_{\mathrm{a}}) = \frac{F_0}{m} \sin \omega_0 t \\ \ddot{x}_{\mathrm{a}} + 2\omega_{\mathrm{a}}\zeta_{\mathrm{a}}(\dot{x}_{\mathrm{a}} - \dot{x}) + \omega_{\mathrm{a}}^2(x_{\mathrm{a}} - x) = 0. \end{cases} \tag{1.12}$$

Adding damping enlarges the frequency band over which the absorber is effective. The downside is an increased vibration amplitude near ω_0 compared to the zero

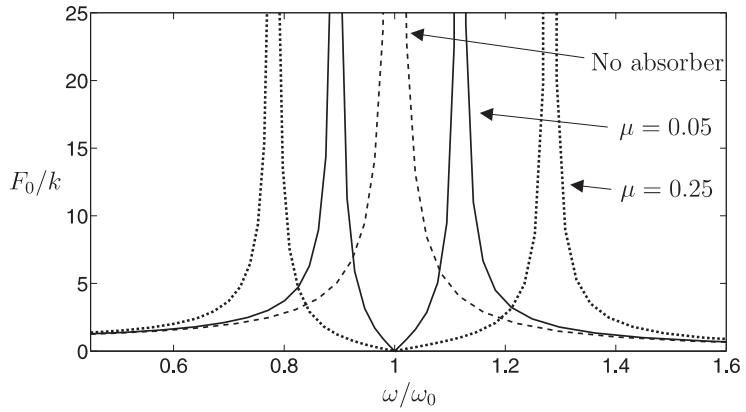

Figure 1.3: Influence of the mass ratio μ on the amplitude Bode plot of primary system, $m = 1$, $k = 1$, $\omega_a = \omega_0$

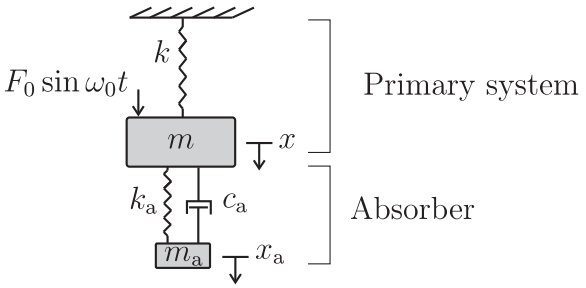

Figure 1.4: Damped dynamic vibration absorber attached to undamped SDOF primary system

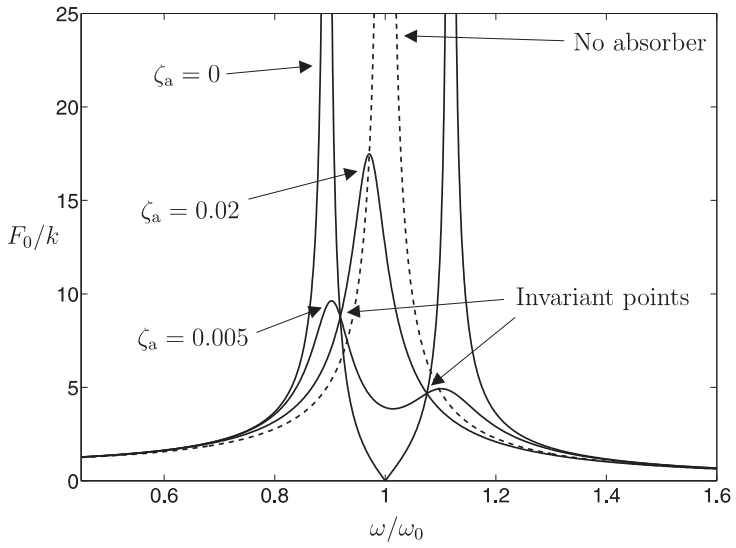

Figure 1.5: Invariant points independent on the value of ζ_a, $m = 1$, $k = 1$, $\mu = 0.05$, $\omega_a = \omega_0$

vibration amplitude attained with the undamped variant. In other words, damping introduces a tradeoff between frequency robustness and vibration attenuation.

A very popular and elegant optimization approach concerning the parameters of the damped vibration absorber is known as the Den Hartog's procedure [10]. It is based on the existence of so called *invariant or fixed points* in the amplitude Bode plot as these points do not depend on ζ_a (Fig. 1.5). For a fixed mass ratio μ, the idea is to tune the absorber's natural frequency ω_a such that both invariant points feature the same vibration amplitude (Fig. 1.6). The amplitude response in between the invariant points can further be flattened by tuning ζ_a as shown in Fig. 1.7. Finally, the entire design procedure can be repeated for a different mass ratio μ which shows that a larger μ leads to an increased vibration attenuation (Fig. 1.7).

For a SDOF primary system, the problem of frequency robustness is more or less solved by using the damped vibration absorber. However, how do we deal with multi-degree-of-freedom (MDOF) primary systems where multiple natural frequencies contribute to the total response, i.e. a so called *multimodal* response? After all, the SDOF linear vibration absorber described above cannot cope with multiple frequencies because it is tuned to a single frequency. Hence, again we encounter some kind of frequency robustness issue.

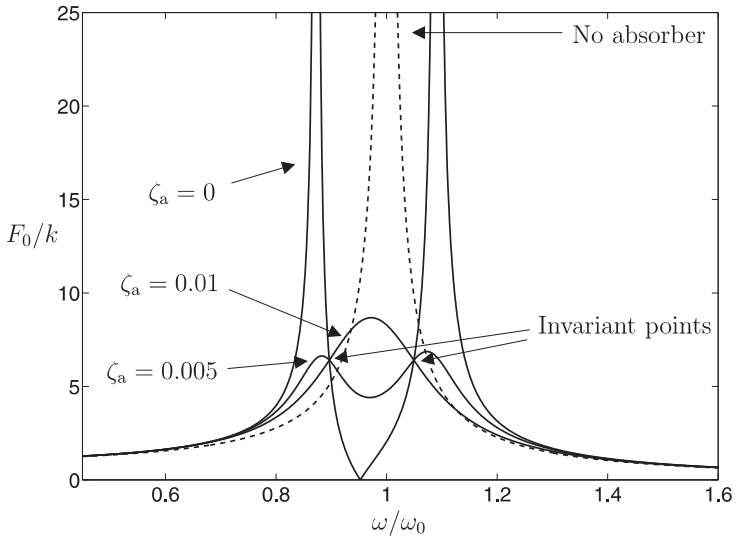

Figure 1.6: Invariant points featuring equal amplitudes, $m = 1$, $k = 1$, $\mu = 0.05$, $\omega_a = \omega_0/(1+\mu)$

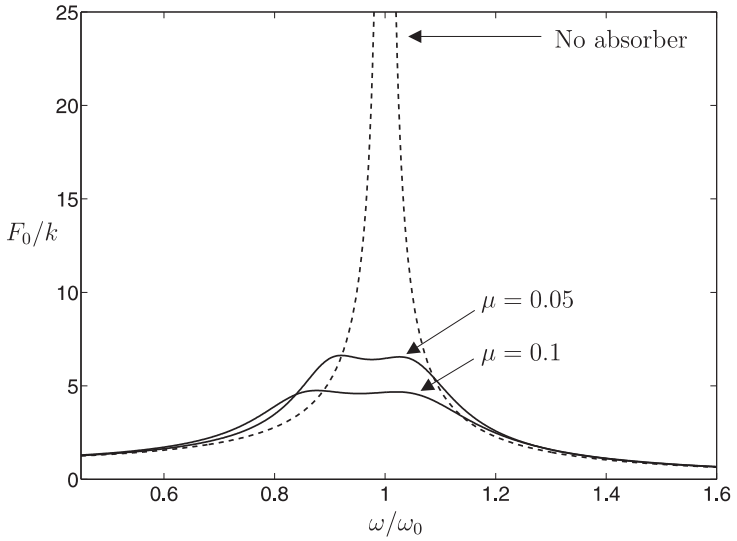

Figure 1.7: Influence of μ *on the vibration attenuation,* $m = 1$, $k = 1$, $\omega_a = \omega_0/(1+\mu)$, $\zeta_a = \sqrt{\frac{mu}{2(1+\mu)}}$

1.2.3 Strongly nonlinear vibration absorbers

Recently, an inventive and very interesting approach has opened new doors towards the development of a frequency-robust mechanical vibration controlling device. The novelty is to replace the linear spring in the conventional tuned mass damper by a *strongly nonlinear* one, where strongly nonlinear refers to a nonlinearizable spring. By introducing the nonlinear spring, a much wider variety of sometimes very complicated response regimes is possible. The challenge lies in picking out and controlling the desired one.

The idea of using a strongly nonlinear spring absorber was first proposed by Gendelman [11]. In his case, the desired response regime was closely related to an energy pumping phenomenon, i.e. the one-way energy transfer from the linear primary system to the nonlinear attachment, which is of course interesting when it comes to vibration reduction. Besides the pumping phenomenon, two other key concepts were addressed in the same article. The first one is the existence of a critical energy threshold below which no efficient vibration reduction is possible. In other words, the energy imparted into the primary system must be high enough for the absorber to work properly, a crucial feature regarding the tuning procedure of the absorber. The second concept is that a strongly nonlinear absorber does not feature a preferential frequency which allows it to work as a multi-frequency vibration reduction element.

The concepts outlined by Gendelman have been further developed and analyzed throughout the years. Most of the results are gathered in [12] where the focus lies on the energy pumping phenomenon or *targeted energy transfer* (TET) from the linear primary system to the nonlinear vibration absorber. Much effort is put in understanding the transient dynamics (which appear to be very complicated) of the following seemingly simple 2DOF system (Fig. 1.8)

$$\begin{cases} m\ddot{x} + kx + c_{\text{na}}(\dot{x} - \dot{x}_{\text{na}}) + k_{\text{na}}(x - x_{\text{na}})^3 = 0 \\ m_{\text{na}}\ddot{x}_{\text{na}} + c_{\text{na}}(\dot{x}_{\text{na}} - \dot{x}) + k_{\text{na}}(x_{\text{na}} - x)^3 = 0. \end{cases} \tag{1.13}$$

Despite its complicated behavior, the nonlinear attachment succeeds in achieving a broadband vibration reduction. An important example in this matter is given in [13] where the existence of so called *resonance capture cascades* is described, i.e. for an impulsively excited MDOF primary system the nonlinear vibration absorber sequentially reduces the vibration energy of the different vibration modes. Compared to its linear counterpart, the strongly nonlinear vibration absorber forms a relatively new research field, many aspects of which are still to be explored.

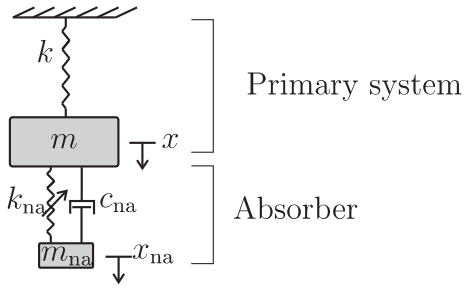

Figure 1.8: Damped nonlinear vibration absorber attached to undamped SDOF primary system

1.3 Objectives and main results

In this dissertation many different aspects of vibration absorbers are investigated. Although a great deal of work has already been performed, we are convinced that the current work succeeds in adding important insights which contribute to a successful practical implementation of the vibration absorber.

The thesis is subdivided into three parts. Part I deals with the linear vibration absorber attached to a MDOF system under harmonic load, Part II with the nonlinear vibration absorber attached to a SDOF system undergoing transient excitation. Part III exemplifies the use of vibration absorbers in a real-life industrial application.

1.3.1 Part I: The linear vibration absorber

For the vibration control engineer, resonances (high vibration amplitudes) are to be avoided while on the other hand antiresonances (zero vibration amplitudes) are desired. We study the possibilities of relocating resonances (Chapter 3) and antiresonances (Chapter 4) by attaching Frahm's undamped vibration absorber.

Chapter 2 is an introductory chapter on the frequency response function (FRF).
Main message/result

- the main features of the FRF are the resonances and the antiresonances
- a general applicable substructure coupling technique shows how the FRF of the entire system is comprised of the FRFs of subsystems

In Chapter 3 the most appropriate attachment location for the absorber is determined when creating a resonance free zone around a troublesome vibration mode.
Main message/result

- the influence of the neighboring vibration modes is taken into account resulting in a multi mode approach extending the classically used single mode approach
- a lower activity of the neighboring modes at the attachment location results in a larger spectral gap around the troubling vibration mode
- a clear indication in determining the attachment location is provided by the neighboring antiresonances which define the boundaries of the spectral gap for $m_{\mathrm{a}} \to \infty$

Chapter 4 deals with the assignment of antiresonances, i.e. points of zero vibration on the structure.
Main message/result

- a substructure decoupling technique reduces the original problem/system to three smaller problems/systems
- two of these subsystems are shown to be working as MDOF absorbers, creating in this way antiresonances at the point of connection to the rest of the system
- the assignment of antiresonances is transformed to the assignment of resonances such that the results of Chapter 3 can be reused
- the subsystems are physical systems, i.e. measurements can be used to assign the antiresonances

1.3.2 Part II: The nonlinear vibration absorber

In this part the focus lies on the amplitude dependence of strongly nonlinear vibration absorbers. More precisely, a critical *energy threshold* exists which means that efficient vibration reduction is only possible above a minimum amount of input energy into the primary system. The threshold phenomenon is studied both theoretically (Chapter 5) and experimentally (Chapter 6).

In Chapter 5, a dimensionless approach is used to explain the energy threshold phenomenon, which is observed when a SDOF cubic spring absorber is attached to a SDOF linear primary system subject to initial conditions.
Main message/result

- a single dimensionless parameter governs the qualitative dynamical behavior

- a simple analytical formula is derived which defines the boundary between weak and strong absorber movement
- the energy threshold concept is extended to a more general parameter threshold concept, i.e. each system parameter features its own threshold value
- the analysis is generally applicable, i.e. it is extendable to general nonlinear spring characteristics, to nonlinear main systems and to forced linear main systems

Chapter 6 presents experimental results of a nonlinear torsional vibration absorber.
Main message/result

- the classical implementation of using a wire as a cubic nonlinear spring is extended to a torsional vibration setting
- the phenomena and trends as described in Chapter 5 are verified both in transient and steady state conditions
- a new implementation of a strongly nonlinear absorber is proposed enabling a wide variety of functional forms

1.3.3 Part III: Towards an industrial application

In the last part of this dissertation, we investigate the feasibility of applying vibration absorbers in an industrial environment where the structure is generally modelled as a complex finite element method (FEM) model. Consequently, a first essential step in the design procedure of the vibration absorber is to reduce this FEM model to a manageable size (Chapter 7), highlighting in this way the dominating dynamical behavior. A challenging application is a hopper dredger drive line (Chapter 8), a complex assembly of rotors suffering from a wide variety of transient and periodic excitations.

The focus of Chapter 7 lies on the numerical implementation of the Guyan reduction technique.
Main message/result

- a new numerical algorithm is developed which sequentially selects the master DOFs instead of sequentially eliminating the slave DOFs as done in the classical algorithm
- a reduction in both time and memory requirements is achieved while an accuracy comparable to the classical approach is obtained

In Chapter 8, the effectiveness of the linear vibration absorber is compared to that of the nonlinear alternative.
Main message/result

- the resonance capture cascades achieved with the nonlinear absorber result in an improved transient vibration reduction over its linear counterpart
- a faster transient vibration reduction is obtained for increased absorber mass

1.4 List of Publications

Part I: The linear vibration absorber

1. F.Petit, M. Loccufier and D. Aeyels. On the attachment location of dynamic vibration absorbers. Journal of Vibration and Acoustics, 131(3), 2008.
2. F. Petit, M. Loccufier and D. Aeyels. Changing the eigenfrequency spectrum using passive vibration absorbers. International Conference on Noise and Vibration Engineering, ISMA2008, Leuven 15-17 September, 2008.
3. F. Petit, M. Loccufier and D. Aeyels. Vibration reduction using dynamic vibration absorbers. Book of Abstracts of the 26th Benelux Meeting on Systems and Control, Lommel, 13-15 March, 2007.

Part II: The nonlinear vibration absorber

4. F.Petit, M. Loccufier, D.Aeyels. A dimensionless approach to nonlinear vibration absorber tuning. Journal of Sound and Vibration, In preparation.
5. F.Petit, M. Loccufier, D.Aeyels. Feasibility of nonlinear absorbers for transient vibration reduction. International Conference on Noise and Vibration Engineering ISMA 2010, Leuven, 20-22 september, 2010.
6. F.Petit, M. Loccufier, D.Aeyels. Adjusting the energy thresholds of a nonlinear vibration absorber. 17th International Congress on Sound and Vibration, Cairo, 19-22 juli, 2010.

Part III: Towards an industrial application

7. F. Petit, M. Loccufier, D. Aeyels. A computationally efficient selection procedure for the master degrees of freedom in condensation. International Journal for Numerical Methods in Engineering, Under review.

8. M. Loccufier and F. Petit. Multifunctional pilot plant for mechanical engineers. The International Journal of Mechanical Engineering Education, 39(1), pp. 31-45, 2011.

9. F. Petit, M. Loccufier. Torsional Vibrations on a Hopper Dredger Due to Transient Conditions. 22nd Biennial Conference on Mechanical Vibration and Noise, IDETC/CIE 2009, San Diego August 30-September 2, 2009.

10. F. Petit, M. Loccufier, D. Aeyels. Feasibility study of vibration absorbers with simplified ship propulsion models. IFAC Conference on Control Applications in Marine Systems, CAMS '07, Bol, 19-21 September, 2007.

11. M. Loccufier and F. Petit. Interaction of governor behaviour and torsional vibrations of a ship propulsion system. Proceedings of the International Conference on Ship and Shipping research, NAV 2006, Genova, 21-23 June, 2006.

12. F. Petit, M. Loccufier, W. Ost and J. Degrieck. Pilot plants for simulating earthquakes. National Congress on Theoretical and Applied Mechanics, Bergen, May 29-30, 2006.

Part I

The linear dynamic vibration absorber

2

On the frequency response function

2.1 A universal concept

A linear time-invariant (LTI) mechanical structure can be modelled in many different ways, ranging from a lumped parameter model where mass, damping and stiffness are assumed to exist only in discrete points of the structure, over a finite element model (FEM) with thousands degrees of freedom, to a fully distributed parameter model having continuously varying mass, damping and stiffness properties. The latter can be considered as the limit case of a lumped parameter model with infinite degrees of freedom. Although the resulting governing equations of these models are not alike (e.g. a lumped system is governed by ordinary differential equations, while a distributed system is described by partial differential equations), they can all be described by the same concept, namely the frequency response function (FRF) matrix H. One component of this matrix H, denoted as H_{RS} is defined as a frequency response function or receptance and determines the steady state displacement x_R of a structure at location R (the Receiver) when it is excited by a sinusoidally varying force f_S at location S (the Source) as displayed in Fig. 2.1. In the frequency domain this relationship becomes

$$X_R(\omega) = H_{RS}(\omega)F_S(\omega) \tag{2.1}$$

while in the time domain with $f_S(t) = f_0 \sin(\omega t)$

$$x_R(t) = A(\omega)f_0 \sin(\omega t + \phi(\omega)). \tag{2.2}$$

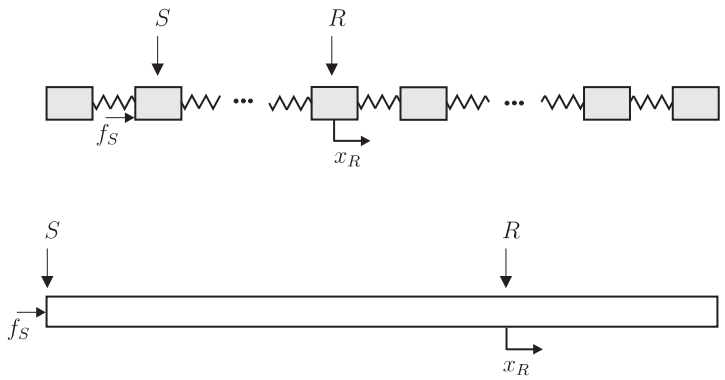

Figure 2.1: Longitudinal vibration response x_R at location R due to harmonic loading f_S at location S; Upper:lumped system; Lower: distributed system

In Eq. (2.2), A and ϕ denote the amplitude and phase of the complex valued function H_{RS} and are displayed as a function of ω in so called Bode plots, examples of which are shown in Fig. 2.2.

2.2 Resonances and antiresonances

The most important features of Fig. 2.2 are the resonances and the antiresonances, highlighted in the amplitude Bode plot. A resonance of the FRF is defined as a frequency for which the FRF reaches a local maximum, while an antiresonance is a frequency for which a local minimum is attained. For undamped structures, the resonance frequencies are equal to the natural frequencies or eigenfrequencies and correspond to the imaginary part of the system poles. Exciting an undamped system at a resonance frequency theoretically leads to infinite vibration amplitudes. In practice however, a small amount of damping is always present such that the vibration amplitude at resonance is bounded. In this case, the imaginary parts of the system poles are known as the damped natural frequencies and differ from the resonance frequencies. In this chapter however, only lightly damped structures are considered. As a result, the above mentioned differences become negligible and further on no distinction between the different entities (natural, damped and resonance frequencies) will be made.

The antiresonances on the other hand correspond to the imaginary part of the zeros of the transfer function and result in points of zero vibration for undamped systems. For damped structures, points of zero vibration become points of minimum vibration. As illustrated in Fig. 2.2, every receptance $H_{R_iS_i}$ $(i = 1, 2)$ is characterized by the same resonance frequencies (global feature) while generally different antiresonances occur depending on R_i and S_i (local feature).

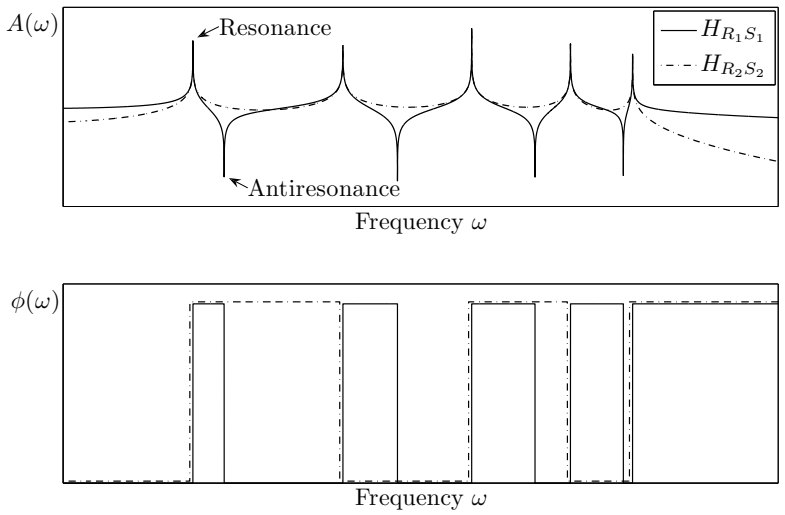

Figure 2.2: Amplitude and phase bode plots for cross receptances $H_{R_1S_1}$ and $H_{R_2S_2}$ of an undamped structure

Regarding vibration control, most interest is focused on relocating the resonances as in this way a possibly damaging resonant condition of the entire structure may be averted. Relocating antiresonances on the other hand can be useful when dealing with sensitive equipment requiring minimum vibration amplitudes. Because resonances and antiresonances correspond to the system poles and zeros, relocating them is equivalent to the placement of poles and zeros [14]. As opposed to the general case where this is achieved by designing a feedback requiring active control means, here only passive means are considered.

2.3 Direct vs inverse problem

When modifying the structure, a distinction is made between the *direct* and the *inverse* problem. In the direct problem, the effect of physical changes (mass, stiffness) on the modal parameters (e.g. eigenfrequencies, eigenvectors) is studied. The goal of the inverse problem is to determine the modifications necessary to obtain the desired changes in modal parameters.

Although relocating resonances and antiresonances can be tackled both as direct and inverse problems, many engineering issues require solving the more demanding inverse problem. As opposed to the direct problem however, the inverse problem is ill-posed as its solution is not unique. Generally multiple solutions are possible

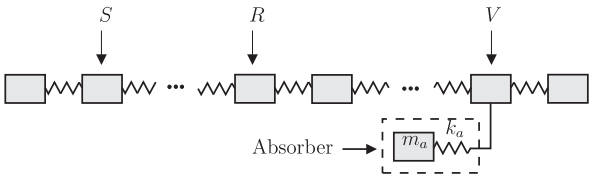

Figure 2.3: MDOF structure with harmonic loading at location S and vibration absorber at location V

while sometimes even no solution exists, e.g. a certain frequency band cannot be cleared of resonances or an antiresonance cannot be relocated to the desired frequency.

In Chapters 3 and 4, we therefore rather focus on the direct problem, i.e. we aim to shift the resonance or the antiresonance as much as possible *towards* its desired outcome. A great help in achieving this goal is a substructure decoupling technique presented in the next section.

2.4 Substructure decoupling technique

Consider Fig. 2.3 which shows the combination of two systems, a MDOF primary system and a SDOF absorber locally attached at V. The primary system is subject to a harmonic excitation at S and we would like to determine the influence of the absorber on the frequency response at R. This information is provided by Lemma 1 which shows a relationship between $\hat{H}_{RS}$, the receptance of the structure with the absorber, and that of the structure without the absorber, which is H_{RS}. The proof starts by decoupling the absorber from the main structure as displayed in Fig. 2.4.

Lemma 1.

$$\hat{H}_{RS}(\omega) = H_{RS}(\omega) - \frac{H_{RV}(\omega)H_{VS}(\omega)}{H_{VV}(\omega) + H_{AA}(\omega)} \tag{2.3}$$

with

$$H_{AA}(\omega) = \frac{\omega^2 - \omega_a^2}{m_a\omega^2\omega_a^2}; \qquad \omega_a^2 = \frac{k_a}{m_a} \tag{2.4}$$

Proof. To take the decoupling into account force f_V and displacement x_V are introduced at the main structure, while force f_A and x_A are introduced at the absorber (Fig. 2.4).

The response x_R at location R is caused by the force f_S at location S and f_V at location V, with $f_V = -f_A$ as these are equal and opposite forces. In the frequency

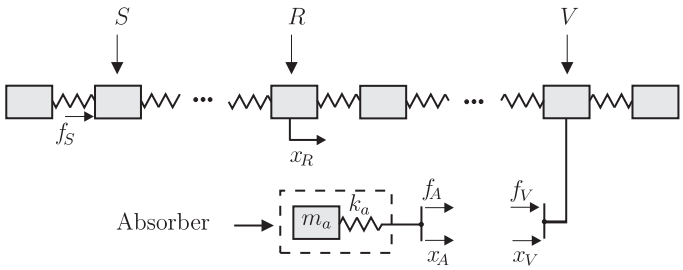

Figure 2.4: Decoupling the absorber from the main system

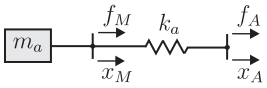

Figure 2.5: The receptance of the absorber as a separate system

domain (with capital letters for Fourier transforms) this yields

$$\begin{aligned} X_R(\omega) &= H_{RS}(\omega)F_S(\omega) + H_{RV}(\omega)F_V(\omega) \\ &= H_{RS}(\omega)F_S(\omega) - H_{RV}(\omega)F_A(\omega). \end{aligned} \tag{2.5}$$

The response x_V is caused by the same forces f_S and f_V and is determined as follows

$$\begin{aligned} X_V(\omega) &= H_{VS}(\omega)F_S(\omega) + H_{VV}(\omega)F_V(\omega) \\ &= H_{VS}(\omega)F_S(\omega) - H_{VV}(\omega)F_A(\omega). \end{aligned} \tag{2.6}$$

The response x_A is only caused by the force f_A

$$X_A(\omega) = H_{AA}(\omega)F_A(\omega) \tag{2.7}$$

$$= X_V(\omega) \tag{2.8}$$

where H_{AA} is the receptance of the absorber when it is considered as a separate system as displayed in Fig. 2.5. In between the absorber mass m_a and its stiffness k_a a new force f_M and a new displacement x_M are defined. With $f_M = f_A$, the receptances belonging to m_a and k_a become

$$X_M(\omega) = \frac{-1}{m_a\omega^2}F_M(\omega) \tag{2.9}$$

$$= \frac{-1}{m_a\omega^2}F_A(\omega) \tag{2.10}$$

$$X_A(\omega) - X_M(\omega) = \frac{1}{k_a}F_A(\omega). \tag{2.11}$$

H_{AA} (2.7) becomes

$$\begin{aligned} H_{AA}(\omega) &= \frac{X_A(\omega)}{F_A(\omega)} \\ &= \frac{1}{k_a} + \frac{-1}{m_a\omega^2} \\ &= \frac{\omega^2 - \omega_a^2}{m_a\omega^2\omega_a^2}. \end{aligned} \tag{2.12}$$

Substituting $X_V(\omega) = H_{AA}(\omega)F_A(\omega)$ into Eq. (2.6) yields

$$F_A(\omega) = \frac{H_{VS}(\omega)}{H_{VV}(\omega) + H_{AA}(\omega)} F_S(\omega). \tag{2.13}$$

Finally, inserting Eq. (2.13) into Eq. (2.5) leads to Eq. (2.3). □

It should be noted that Lemma 1 can also be used to describe the connection between any two arbitrary systems. The only necessary condition is that the two systems are connected through a single coordinate. This generality is exploited in Chapters 3 and 4 where Eq. (2.3) serves as a starting point for many of the derived results.

Remark In practice, adding a vibration absorber at a single location or *coordinate* is impossible to achieve. The attachment of an absorber always effects multiple coordinates due to the spatial character of the attachment. Consequently, the subsequent theoretical developments should be addressed with care especially when higher natural frequencies are considered. For lower natural frequencies however, this should pose no problems.

3 Relocating resonances

3.1 Introduction

The most important task in vibration engineering is the avoidance of resonance, a condition where the frequency of the excitation source matches a natural frequency of the structure. In such a situation, even a small force can lead to unacceptable vibration levels as the amplitude builds up each vibration cycle. To avoid a resonance condition, the excitation frequency has to be separated from the natural frequencies of the structure. Because it is generally not straightforward to change the frequency of the vibration source (e.g. by changing the number of blades on a fan), it is often preferred to alter the natural frequencies (the resonances) of the structure.

However, as the ultimate goal is to avoid a resonance condition, simply displacing the resonances is not sufficient. For a frequency robust solution, a resonance free zone or spectral gap around the excitation frequency is required [15, 16]. An important objective is to create such a spectral gap with a minimal amount of modification to the structure. Here, this means realizing the resonance free zone with a minimum amount of absorber mass. A crucial aspect in this matter and the topic of this chapter is where the absorber should be located.

Remark Attaching a vibration absorber also covers two special types of structural modification, namely the attachment of a mass (for $k_a \to \infty$) and that of a grounded spring (for $m_a \to \infty$) as shown in Fig. 3.1.

In practice, when a structure is resonating at a certain natural frequency, the

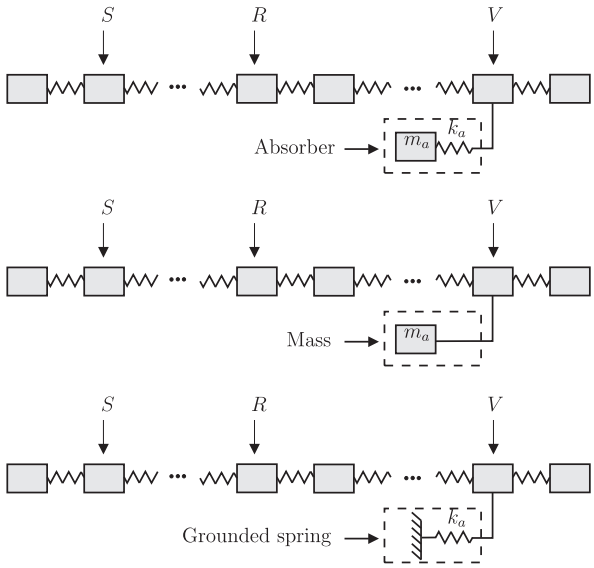

Figure 3.1: Undamped structure with harmonic loading at location S and a local attachment at V; Upper: vibration absorber, Middle: mass, Lower: grounded spring

absorber's location is determined according to the maximum value of the corresponding eigenvector or vibration mode shape. As only one vibration mode is considered, this is known as the single mode approach [17]. Here, we extend the commonly used single mode approach to a multi mode approach where the influence of the neighboring vibration modes is taken into account. For a certain absorber mass m_a, we determine which attachment locations provide the largest spectral gap in between the resonant mode and the new eigenfrequencies close to this mode.

Two results are derived. First, for a wider spectral gap it is required that the activity of the neighboring vibration modes at the attachment location is low. Secondly, as a result of the interlacing property, it is shown that for $m_a \to \infty$, the spectral gap is limited by the neighboring zeros at the attachment location. Both results are combined in Section 3.4 describing a procedure which determines the location that maximizes the spectral gap.

3.2 Resonances after attaching a vibration absorber

Regarding the receptance H_{VV} of an m-degree of freedom system, we define the resonances as ω_i ($i = 1 \ldots m$). The resonances of the receptance $\hat{H}_{VV}$ belonging to the system with absorber are defined as $\hat{\omega}_i$ ($i = 1 \ldots m + 1$).

When attaching an undamped vibration absorber at location V, the new recep-

tance $\hat{H}_{VV}$ can be derived from Eqs. (2.3-2.4) with $R = S = V$.

$$\hat{H}_{VV}(\omega) = \frac{H_{VV}(\omega)H_{AA}(\omega)}{H_{VV}(\omega) + H_{AA}(\omega)} \tag{3.1}$$

The new resonances are the solution of

$$H_{VV}(\omega) + H_{AA}(\omega) = 0 \tag{3.2}$$

$$1 - m_a \frac{\omega_a^2 \omega^2}{\omega_a^2 - \omega^2} H_{VV}(\omega) = 0 \tag{3.3}$$

while the antiresonances are determined by

$$H_{VV}(\omega)H_{AA}(\omega) = 0 \tag{3.4}$$

$$H_{VV}(\omega)\frac{\omega^2 - \omega_a^2}{m_a \omega^2 \omega_a^2} = 0. \tag{3.5}$$

Theorem 1. *An undamped vibration absorber with constant tuning frequency $\omega_a = \sqrt{\frac{k_a}{m_a}}$ attached at location V of a lightly damped system shifts the resonances of $\hat{H}_{VV}$ away from ω_a in a monotone way. The resonances of $\hat{H}_{VV}$ can not be shifted beyond the neighboring antiresonances of H_{VV}.*

Proof. Theorem 1 can be easily proven by applying root locus theory which is usually described in the Laplace domain. Therefore, we introduce the transfer function G_{VV} which corresponds to the FRF H_{VV} as follows

$$\lim_{s \to j\omega} G_{VV}(s) = H_{VV}(\omega). \tag{3.6}$$

With this notation, the Laplace domain equivalent of Eq. (3.1) becomes [1]

$$\hat{G}_{VV}(s) = \frac{G_{VV}(s)G_{AA}(s)}{G_{VV}(s) + G_{AA}(s)}; \qquad G_{AA}(s) = \frac{s^2 + \omega_a^2}{m_a \omega_a^2 s^2} \tag{3.7}$$

$$= \frac{G_{VV}(s)}{1 + m_a \frac{s^2 \omega_a^2}{s^2 + \omega_a^2} G_{VV}(s)}. \tag{3.8}$$

Equation (3.8) can be interpreted as the transfer function of a closed loop system with G_{VV} as the open loop transfer function and $\frac{s^2\omega_a^2}{s^2+\omega_a^2}$ as the feedback transfer function with feedback gain m_a as illustrated in Fig. 3.2. According to root locus theory [18], the poles of the closed loop system start at the poles of $\frac{s^2\omega_a^2}{s^2+\omega_a^2}G_{VV}(s)$ for $m_a \to 0$ and reach the zeros of $\frac{s^2\omega_a^2}{s^2+\omega_a^2}G_{VV}(s)$ for $m_a \to \infty$. Furthermore, due to the quadratic form of G_{VV} and $\hat{G}_{VV}$, they both have alternating poles and

[1] As already mentioned in Chapter 2, the imaginary parts of the poles and zeros of G_{VV} are approximately equal to the resonances and antiresonances of the FRF H_{VV}.

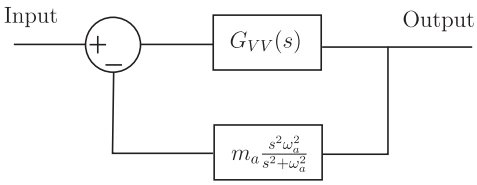

Figure 3.2: The attachment of a vibration absorber as a feedback system

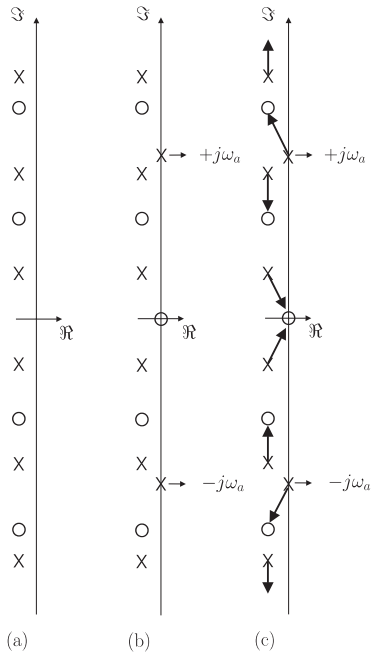

Figure 3.3: (a) Poles and zeros of G_{VV}, (b)Poles and zeros of $\frac{s^2\omega_a^2}{s^2+\omega_a^2}G_{VV}(s)$; compared to (a), $\frac{s^2\omega_a^2}{s^2+\omega_a^2}$ adds two zeros at $s=0$ and two poles at $s=\pm j\omega_a$, (c) Root locus as a function of m_a

zeros along the imaginary axis. This is known as the interlacing property [2]. As a result, the poles of $\hat{G}_{VV}$ are bounded by the zeros of G_{VV} and the zeros at $s=0$. A graphical representation is given in Fig. 3.3 where the arrows indicate the root locus as a function of m_a. □

The damped case In practice, a small amount of damping is always present in the absorber such that G_{AA} becomes

$$G_{AA}(s) = \frac{s^2 + 2\zeta_a\omega_a s + \omega_a^2}{m_a(\omega_a^2 + 2\zeta_a\omega_a s)s^2}. \tag{3.9}$$

Equation (3.8) is adjusted accordingly

$$\hat{G}_{VV}(s) = \frac{G_{VV}(s)}{1 + m_a \frac{(\omega_a^2 + 2\zeta_a\omega_a s)s^2}{s^2 + 2\zeta_a\omega_a s + \omega_a^2} G_{VV}(s)}. \tag{3.10}$$

Instead of the poles $s = \pm j\omega_a$, the absorber adds the poles $s = -\zeta_a\omega_a \pm j\sqrt{1-\zeta_a^2}\omega_a$. Besides the two zeros at $s = 0$, an extra zero is created at $s = \frac{-\omega_a}{2\zeta_a}$. We consider the assembly of the lightly damped main system with a damped vibration absorber again as a lightly damped system. Consequently, the interlacing property still holds for $\hat{G}_{VV}$ such that Theorem 1 is still valid.

3.3 On the attachment location

In resolving a resonance condition for mode i, the new eigenfrequencies close to ω_i ($\hat{\omega}_i < \omega_i < \hat{\omega}_{i+1}$) are the most important ones. Shifting these further away from ω_i, leads to a larger resonance free frequency band. We propose the following design principle for the absorber:

Design Principle 1. *The absorber is designed such that the resonance free zone around the resonance frequency ω_i is maximized.*

Throughout the next sections this principle is used as a basis to compare different possible attachment locations for the absorber. For a certain absorber mass m_a, we determine locations V that maximize the spectral gap between ω_i and the new eigenfrequencies $\hat{\omega}_i$ and $\hat{\omega}_{i+1}$, i.e. $\max\{\min(\omega_i - \hat{\omega}_i, \hat{\omega}_{i+1} - \omega_i)\}$. To simplify the analysis, the main system and the absorber are considered to be undamped although the results can easily be extended to lightly damped systems.

3.3.1 The single mode approach

The attachment location of the absorber is usually determined by considering the eigenvector e_i corresponding to the mode i in resonance. Denote the component of e_i corresponding to location V as $v'e_i$. The larger the mode activity $|v'e_i|$ at a certain location V, the better the location is assumed to be. This is known as the single mode approach [17]. This approach is valid when dealing with a sufficiently small absorber mass and well separated eigenfrequencies. In this case the effect of the neighboring modes can be neglected when choosing a suitable attachment location as shown hereafter.

The new resonances after attaching an undamped absorber are given by Eq. (3.3), repeated here for convenience

$$1 - m_a \frac{\omega_a^2 \omega^2}{\omega_a^2 - \omega^2} H_{VV}(\omega) = 0. \tag{3.11}$$

Using modal analysis [19], H_{VV} can be rewritten as

$$H_{VV}(\omega) = \sum_{k=1}^{m} \frac{(v'e_k)^2}{\omega_k^2 - \omega^2} \tag{3.12}$$

where ω_k, $k = 1, ..., m$ are the eigenfrequencies of the main system without absorber and $e_k \in R^{m\times 1}$, $k = 1, ..., m$ the corresponding mass matrix normalized eigenvectors, i.e. $e_k' M e_k = 1; k = 1, ..., m$. The new eigenfrequencies $\hat{\omega}_i$ and $\hat{\omega}_{i+1}$ are very close to the resonance frequency ω_i such that in this neighborhood, Eq. (3.12) can be approximated by

$$H_{VV}(\omega) \approx \frac{(v'e_i)^2}{\omega_i^2 - \omega^2} \tag{3.13}$$

which changes Eq. (3.11) into

$$1 - m_a \frac{\omega_a^2 \omega^2}{\omega_a^2 - \omega^2} \frac{(v'e_i)^2}{\omega_i^2 - \omega^2} = 0. \tag{3.14}$$

From Eq. (3.14) it can be seen that for a fixed value of ω_a, the shift of the eigenfrequencies near ω_i depends on $m_a(v'e_i)^2$. For an equal shift in eigenfrequencies, a smaller $(v'e_i)^2$ requires a larger m_a. We recover the well known result that an antinodal location, i.e. the location with the maximum value for $|v'e_i|$, yields the best location.

Determining a suitable attachment location can also be achieved by applying sensitivity analysis. With this technique one obtains the sensitivity of the modal parameters (eigenfrequencies and eigenvectors) towards physical changes of the structure. A theoretical derivation of this technique for undamped systems can be found in [20] for the case of general structural modification. The sensitivity of the eigenfrequencies ω_i as a function of a point mass m_a (a limit case of the absorber) attached at location V is given as follows

$$\frac{\delta \omega_i}{\delta m_a} = \omega_i \frac{v'e_i^2}{2m_a}. \tag{3.15}$$

Equation (3.15) shows that the best location V for adding mass is where $v'e_i$ reaches a maximum. In other words: using sensitivity analysis results in attaching mass at an antinode of ω_i, again a single mode approach. However, in Eq. (3.15) only the first order term of a Taylor expansion is presented. Consequently, it is only valid for a sufficiently small m_a. To overcome this problem, different authors show how the second partial derivative can be calculated. However, since these calculations require the knowledge of *all* vibration modes and their mode shapes, they are rarely used.

3.3.2 The multi mode approach

As shown in [21], the eigenvector e_i does not always provide all the information needed to find the best location. Other vibration modes can become important when dealing with larger absorber masses as used in ship propulsion applications. Also, when dealing with eigenfrequencies close to each other, neighboring modes have to be taken into account.

Using the Design Principle presented above, we reveal the influence of the neighboring vibration modes and therefore extend the single mode approach to a multi mode approach.

Using Eq. (3.3) and (3.12) the new eigenfrequencies $\hat{\omega}_k$, $k = 1, \ldots, m+1$ are given by

$$1 - m_a \frac{\omega_a^2 \omega^2}{\omega_a^2 - \omega^2} \sum_{k=1}^{m} \frac{(v' e_k)^2}{\omega_k^2 - \omega^2} = 0. \tag{3.16}$$

Without loss of generality, we assume $\overline{\omega}_{i-1} < \omega_a < \omega_i$, i.e. ω_a lies near ω_i which is the typical tuning approach.

- Assume eigenfrequency ω_i has to be shifted to a new eigenfrequency $\hat{\omega}_i$ such that $\hat{\omega}_i < \omega_a < \omega_i$. We determine the attachment location V that provides this shift with a minimal amount of the absorber mass m_a. Equation (3.16) becomes

$$1 - m_a \frac{\omega_a^2 {\hat{\omega}_i}^2}{\omega_a^2 - {\hat{\omega}_i}^2} \sum_{k=1}^{m} \frac{(v' e_k)^2}{\omega_k^2 - {\hat{\omega}_i}^2} = 0. \tag{3.17}$$

  As $\frac{\omega_a^2 {\hat{\omega}_i}^2}{\omega_a^2 - {\hat{\omega}_i}^2} > 0$, a large positive $\sum_{k=1}^{m} \frac{(v' e_k)^2}{\omega_k^2 - {\hat{\omega}_i}^2}$ fulfills Eq. (3.17) with a smaller absorber mass yielding a better location V. Consider the different components of $\sum_{k=1}^{m} \frac{(v' e_k)^2}{\omega_k^2 - {\hat{\omega}_i}^2}$ in (3.17)

$$\frac{(v' e_k)^2}{\omega_k^2 - {\hat{\omega}_i}^2} < 0, \quad k = 1, ..., i-1$$

$$\frac{(v' e_k)^2}{\omega_k^2 - {\hat{\omega}_i}^2} > 0, \quad k = i, ..., m.$$

  The mode activity $(v' e_k)^2$ of mode k, $k = 1, ..., i-1$ must be low, while the mode activity $(v' e_k)^2$ of mode k, $k = i, ..., m$ must be high. As $|\frac{(v' e_k)^2}{\omega_k^2 - {\hat{\omega}_i}^2}|$ increases as ω_k is closer to $\hat{\omega}_i$, we concentrate on the modi i, $i-1$ and $i+1$. We conclude that a location V corresponding to larger $(v' e_i)^2$ and $(v' e_{i+1})^2$ and to smaller $(v' e_{i-1})^2$, achieves the shift from ω_i to $\hat{\omega}_i$ with a smaller absorber mass.

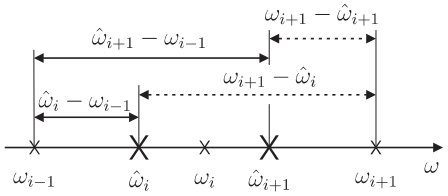

Figure 3.4: Analysis of the neighboring modes

- For the new eigenfrequency $\hat{\omega}_{i+1}$ it holds that $\hat{\omega}_{i+1} > \omega_i > \omega_a$. Equation (3.16) becomes

$$1 - m_a \frac{\omega_a^2 \hat{\omega}_{i+1}^2}{\omega_a^2 - \hat{\omega}_{i+1}^2} \sum_{k=1}^{m} \frac{(v' e_k)^2}{\omega_k^2 - \hat{\omega}_{i+1}^2} = 0. \tag{3.18}$$

  As $\frac{\omega_a^2 \hat{\omega}_{i+1}^2}{\omega_a^2 - \hat{\omega}_{i+1}^2} < 0$, a large negative $\sum_{k=1}^{m} \frac{(v' e_k)^2}{\omega_k^2 - \hat{\omega}_{i+1}^2}$ allows for a smaller absorber mass and yields a better location V.

  A similar analysis shows that a location V corresponding to larger $(v' e_i)^2$ and $(v' e_{i-1})^2$ and to smaller $(v' e_{i+1})^2$, achieves the shift from ω_i to $\hat{\omega_{i+1}}$ with a smaller absorber mass.

As both $|\omega_i - \hat{\omega}_i|$ and $|\omega_i - \hat{\omega}_{i+1}|$ have to be maximized we notice a contradictory influence of the neighboring modes. From Fig. 3.4 it is clear that

$$0 < \frac{(v' e_{i+1})^2}{\omega_{i+1}^2 - \hat{\omega}_i^2} < \frac{(v' e_{i+1})^2}{\omega_{i+1}^2 - \hat{\omega}_{i+1}^2}. \tag{3.19}$$

As $\frac{(v' e_{i+1})^2}{\omega_{i+1}^2 - \hat{\omega}_i^2}$ increases $\sum_{k=1}^{m} \frac{(v' e_k)^2}{\omega_k^2 - \hat{\omega_i}^2}$ of Eq. (3.17), it contributes to a smaller absorber mass. On the contrary, $\frac{(v' e_{i+1})^2}{\omega_{i+1}^2 - \hat{\omega}_{i+1}^2}$ increases $\sum_{k=1}^{m} \frac{(v' e_k)^2}{\omega_k^2 - \hat{\omega}_{i+1}^2}$ of Eq. (3.18) leading to a larger absorber mass. Based on Eq. (3.19), we can conclude that the overall effect of mode $i+1$ is counteracting, i.e. a high activity for this mode (large $(v' e_{i+1})^2$) requires a larger absorber mass m_a to shift towards eigenfrequency $\hat{\omega}_{i+1}$. The same conclusion holds for mode $i-1$. We summarize these findings in Proposition 1.

Proposition 1. *Given the attachment location V, a low activity for the neighboring modes improves the performance of the absorber as defined in the Design Principle.*

Although a high activity $(v' e_i)^2$ for the mode corresponding to ω_i is still the most important argument to choose the absorber location, this means that a location V with a relatively smaller $(v' e_i)^2$ can still be favorable if the neighboring modes have a relatively lower activity, i.e. $(v' e_{i-1})^2$ and $(v' e_{i+1})^2$ are lower.

Remark 1 From the multi mode approach it is clear that the optimal attachment location V can change depending on the amount of the absorber mass. Therefore two optimization problems can be distinguished without necessarily the same outcome for the absorber parameters:

1. Given the absorber mass m_a, determine the absorber parameters (location, stiffness) that maximize the shift of the new eigenfrequencies. This is a direct problem.
2. Given the required shift of the new eigenfrequencies, determine the absorber parameters that achieve this shift with a minimal absorber mass m_a. This is an inverse problem.

Remark 2 As shown in Theorem 1, for $m_a \to \infty$, the eigenfrequencies of the system with absorber are equal to the zeros of G_{VV} at the attachment location V. Therefore, in the multi mode approach, the neighboring antiresonances offer, in addition to $|v'e_i|$, a clear indication of suitable attachment locations. The larger their separation from the resonant frequency, the better the location. Since this is only true for $m_a \to \infty$, this is merely an approximated way of finding appropriate attachment locations. In section 3.4, this property is used to take into account the effect of the neighboring modes when determining the best absorber location.

Remark 3 As already mentioned in Chapter 2, the results obtained with the absorber are completely analogous when a mass or a grounded spring is attached to the main system because the latter are limit cases of the absorber ($k_a \to \infty$ and $m_a \to \infty$ respectively).

3.4 Procedure

In Section 3.3.1 the commonly used single mode approach was compared with the multi mode approach. It was shown that the activity of the neighboring modes can be important when an appropriate attachment location of the absorber is determined. Here we explain a step by step procedure to identify the best location for the absorber. This procedure combines the single mode approach, valid for sufficiently small absorber mass, with Theorem 1 where it is shown that the neighboring antiresonances limit the shift of the new eigenfrequencies for $m_a \to \infty$. These neighboring zeros are a representation of the activity of the neighboring modes. They provide extra information required to determine the best location for every absorber mass m_a. In a resonance condition for mode i the following procedure is proposed:

1. Consider the location V where the mode activity $|v'e_i|$ reaches a maximum. This location will be optimal for sufficiently small absorber mass.

2. Consider the location V where the distance in frequency between the neighboring zeros of ω_i is highest. This defines the optimal location for $m_a \to \infty$.

3. When 1. and 2. yield the same location: this location will be optimal for every amount of m_a.

4. When 1. and 2. yield a different location: given a certain absorber mass m_a, consider the new eigenfrequencies when the absorber is attached according to 1. If these are closer to the neighboring zeros than they are to ω_i, the location obtained in 2. will be optimal. If not, 1. yields the optimal location.

3.5 Locating the absorber at a vibration node of a neighboring mode

In step 2 of the Procedure of section 3.4, one needs to determine the location with the largest frequency separation in between the neighboring antiresonances of mode i. For a lumped parameter model the outcome of this step is a single coordinate. However, if the lumped parameter model is extended to a pseudo continuous model, we show in this section that the outcome of step 2 can be a location *in between* two coordinates. Of course, a location in between two coordinates does not exist but can be created if the vibration amplitude is assumed to vary linearly between two coordinates of the system. Under this assumption the eigenvector is extended from a finite vector to an infinite vector where each component is denoted as $v_\alpha' e_i$ with v_α equal to

$$v_\alpha = \begin{bmatrix} 0 & 0 & \cdots & \alpha & 1-\alpha & 0 & \cdots & 0 \end{bmatrix}'. \tag{3.20}$$

Up till now α was zero. By letting $0 \leq \alpha \leq 1$ we show that the distance in between the neighboring antiresonances can reach a maximum in between two components. More specifically, this maximum occurs at a vibration node of a neighboring mode.

Theorem 2. *A vibration node occurs for mode k at location V_α ($v_\alpha' e_k = 0$) if and only if $H_{V_\alpha V_\alpha}$ has a pole-zero cancellation at $s = j\omega_k$.*

Proof For mass normalized eigenvectors ($e_k' M e_k = 1; \quad k = 1, ..., m$), $H_{V_\alpha V_\alpha}$ can be written as

$$\begin{aligned} H_{V_\alpha V_\alpha} &= v_\alpha' (Ms^2 + K)^{-1} v_\alpha & (3.21) \\ &= v_\alpha' E (I_m s^2 + \Omega^2)^{-1} E' v_\alpha & (3.22) \end{aligned}$$

with $\Omega = diag(\omega_k); k = 1, ..., m$, $E = [e_1 e_2 ... e_m]$ and $I_m \in R^{m \times m}$ the identity matrix. The transfer function $H_{V_\alpha V_\alpha}$ can be realized by the state space matrices

$\{A_\alpha, B_\alpha, C_\alpha\}$

$$H_{V_\alpha V_\alpha}(s) = C_\alpha(sI_{2m} - A_\alpha)^{-1}B_\alpha \quad (3.23)$$
$$= \frac{b(s)}{a(s)} \quad (3.24)$$

where $A_\alpha \in R^{2m\times 2m}, B_\alpha \in R^{2m\times 1}, C_\alpha \in R^{1\times 2m}, I_{2m} \in R^{2m\times 2m}$:

$$A_\alpha = \begin{bmatrix} 0 & I_m \\ -\Omega^2 & 0 \end{bmatrix}, \quad B_\alpha = \begin{bmatrix} 0 \\ E'v_\alpha \end{bmatrix}, \quad C_\alpha = \begin{bmatrix} v'_\alpha E & 0 \end{bmatrix}, \quad I_{2m} = \begin{bmatrix} I_m & 0 \\ & I_m \end{bmatrix}. \quad (3.25)$$

The lemma of Hautus states

Lemma 2. *$\{A, B\}$ is controllable if and only if $rank\begin{bmatrix} sI_{2m} - A & B \end{bmatrix} = 2m$ for all eigenvalues s of A.*

Applied to the matrices in Eq. (3.25) and after some row and column manipulations, we have

$$\{A_\alpha, B_\alpha\} \text{ is controllable} \Leftrightarrow rank\begin{bmatrix} s^2 I_m + \Omega^2 & E'v_\alpha \end{bmatrix} = m, \text{ for all } \omega_k; \quad k = 1, ..., m.$$

or

$$\{A_\alpha, B_\alpha\} \text{ is controllable } \Leftrightarrow e'_k v_\alpha \neq 0; \quad k = 1, ..., m. \quad (3.26)$$

As we are dealing with a collocated system ($H_{V_\alpha V_\alpha}$), the same condition holds for observability of $\{C_\alpha, A_\alpha\}$ as well.
We first prove that a pole-zero cancellation for $H_{V_\alpha V_\alpha}$ at $s = j\omega_k$ yields a vibration node for mode k at location $v'_\alpha q$. Theorem 2.4-5 of Kailath, p. 127 [14] states

Theorem 3. *A realization $\{A, B, C\}$ is minimal if and only if $a(s) = det(sI_{2m} - A)$ and $b(s) = CAdj(sI_{2m} - A)B$ are relatively prime.*

If $H_{V_\alpha V_\alpha}$ features a pole-zero cancellation, then $\{A_\alpha, B_\alpha, C_\alpha\}$ is not a minimal realization of $H_{V_\alpha V_\alpha}$. We formulate theorem 2.4-6 of Kailath, p. 127 [14]

Theorem 4. *A realization $\{A, B, C\}$ is minimal if and only if $\{A, B\}$ is controllable and $\{C, A\}$ is observable.*

This means $\{A_\alpha, B_\alpha\}$ of Eq. (3.25) is not controllable and / or $\{C_\alpha, A_\alpha\}$ of Eq. (3.25) is not observable. Based on Lemma 6.1 and Eq. (3.26): $v'_\alpha e_k = 0$, i.e. V_α is located at a node for mode k. As all theorems and lemmas are valid in both directions one can easily prove the opposite statement, i.e. a vibration node ($v'_\alpha e_k = 0$) yields a pole-zero cancellation for ω_k in $H_{V_\alpha V_\alpha}$. □

Theorem 2 states that when location V_α defines a vibration node for mode $i + 1$ ($v'_\alpha e_{i+1} = 0$), the neighboring zero of ω_i becomes equal to its neighboring pole

ω_{i+1}. This means that at a vibration node, the distance in frequency between the resonance ω_i and its neighboring zero is maximum.

Compared to the case where V_α defines an antinode for mode i, the mode activity $|v'_\alpha e_i|$ will decrease when V_α moves away from this antinode. Then the activity of the neighboring modes is important. If their mode activity decreases faster than $|v'_\alpha e_i|$ does, they can compensate for the decrease of $|v'_\alpha e_i|$. As explained in the multi mode approach an alternative representation for the activity of the neighboring modes of eigenfrequency ω_i, is the distance between the neighboring zeros. Based on theorem 2 we can conclude that attaching the absorber in a region nearby an antinode not necessarily means that the performance of the absorber drops heavily. This new information becomes valuable when the absorber cannot be located at an antinode due to constructive constraints. It is illustrated in the first example of Section 3.6.

Remark By locating the absorber at a vibration node, the corresponding mode is left unchanged. Further more, resonances $\omega_k < \omega_a$ are lowered in frequency by the absorber while resonances $\omega_k > \omega_a$ become higher. As a result, the spectral gap between two resonances ω_i and ω_{i+1} can always be increased by attaching a vibration absorber at a vibration node of mode i while keeping the tuning frequency $\omega_a \leq \omega_i$. Likewise, the absorber can be attached at a node of mode $i+1$ while keeping the tuning frequency $\omega_a \geq \omega_{i+1}$. This interesting result is analogous to the result derived in [15] where spectral gaps are increased by adding grounded spring-mass oscillators.

As an example consider the lumped mass system of Fig. 3.6 with modal parameters listed in Table 3.1. Suppose the goal is to enlarge the spectral gap between mode 2 (4.89 rad/s) and 3 (7.70 rad/s). One way to achieve this is by decreasing the natural frequency of mode 2 while keeping the natural frequency of mode 3 unaltered. Therefore, a vibration absorber is attached at a vibration node of mode 3 and tuned such that $\omega_a = \omega_3$. The vibration nodes of mode 3 in the pseudo continuous version of eigenvector e_3 are shown in Fig. 3.5. Finally, attaching a vibration absorber with $m_a = 0.5kg$ at the vibration node in between coordinates q_2 and q_3 increases the spectral gap from (7.70-4.89) rad/s to (7.70-4.46) rad/s.

3.6 Examples

Lumped mass system Consider an undamped uniform spring-mass system (5 DOF) with $k = 34.57$ N/m and $m = 1$ kg, excited with a harmonic force F (Fig. 3.6). The eigenfrequencies and the corresponding mass matrix normalized eigenvectors are shown in Table 3.1. Assume a resonant condition for $\omega_3 = 7.70$ rad/s, i.e. the excitation frequency equals ω_3. Table 3.2 shows the neighboring antiresonances for mode 3.

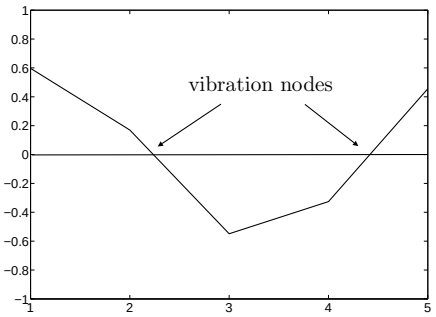

Figure 3.5: 5 DOF uniform spring-mass system

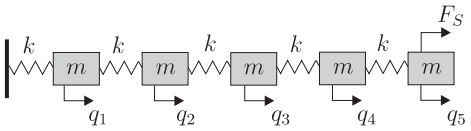

Figure 3.6: 5 DOF uniform spring-mass system

- A vibration absorber is attached with mass $m_a = 0.05$ kg. We compare two different attachment locations: attached at coordinate q_1 and attached at coordinate q_3. Then we repeat this procedure with an absorber of mass $m_a = 0.5$ kg.

  We apply the procedure given in Section 3.4.

  - The activity of mode 3 reaches a maximum at location q_1. For m_a small this will be the optimal location.
  - Table 3.2 shows that the distance between the neighboring antiresonances is highest at location q_3. Therefore as m_a increases, location q_3 maximizes the spectral gap between the new eigenfrequencies ($\hat{\omega}_3$, $\hat{\omega}_4$) and ω_3 , although its modal activity is lower (Table 3.1).
  - To know when this happens the new eigenfrequencies of the system with absorber are considered. For $m_a \approx 0.25kg$ the shifted eigenfrequencies are closer to the neighboring zeros than they are to mode 3. Then the influence of the neighboring zeros becomes dominant yielding q_3 as the best location.

  The results are summarized in Table 3.3.

  Assume location q_3 is not available. Instead we attach the absorber between q_3 and q_4 as in that region the distance in frequency between the neighboring zeros is increased. Table 3.3 shows the location V where this distance reaches

	mode 1	mode 2	mode 3	mode 4	mode 5
e_{i1}	0.17	-0.46	0.60	0.55	-0.33
e_{i2}	0.33	-0.60	0.17	-0.46	0.55
e_{i3}	0.46	-0.33	-0.55	-0.17	-0.60
e_{i4}	0.55	0.17	-0.33	0.60	0.46
e_{i5}	0.60	0.55	0.46	-0.33	-0.17
ω_i (rad/s)	1.67	4.89	7.70	9.89	11.28

Table 3.1: Modal parameters

located at coordinate	q_1	q_2	q_3	q_4	q_5
antiresonances (rad/s)	5.88-9.01	7.33-8.32	5.88-9.51	5.88-8.31	6.91-9.52
|distance| (rad/s)	3.13	0.99	3.63	2.43	2.61

Table 3.2: Neighboring antiresonances for mode 3 (= 7.70 rad/s)

a maximum (4.62 rad/s). The corresponding spectral gap is shown. As can be seen the performance of the absorber has not decreased significantly according to section 3.5.

- We rerun the previous example, but replace the vibration absorber by a point mass, a limit case of the absorber for $k_a \to \infty$ as displayed in Fig. 3.1[1]. The results are shown in Table 3.4. Again location q_3 outperforms location q_1 for higher point masses. Similar conclusions can be drawn for the location in between q_3 and q_4. The lower performance of the point mass compared to the absorber is especially present for low values of m_a.

Continuous structures Consider the transversal vibrations of a uniform beam simply supported at both ends as shown in Fig. 3.7. If the Bernoulli-Euler theory is assumed [22], the equations of motion become

$$\rho A \frac{\partial^2 y}{\partial t^2} = EI \frac{\partial^4 y}{\partial z^4} + P(z,t) \tag{3.27}$$

where ρ is the mass density, A is the area of cross-section, E is Young's modulus, I is the second moment of area of the cross-section about the X-axis and $P(z,t)$ is the applied load. The deflection of the beam can be expressed as the sum of

[1]The case of a grounded spring is not considered as it has less practical usefulness.

location V	m_a (kg)	ω_a (rad/s)	maximum spectral gap (rad/s)
q_1	0.05	7.71	0.50
q_3	0.05	7.67	0.46
q_1	0.5	8.12	1.16
q_3	0.5	7.45	1.20
$0.78q_3 + 0.22q_4$	0.5	7.16	1.19

Table 3.3: Comparing the maximum spectral gap as a function of the absorber mass m_a

location V	$m_a(kg)$	maximum spectral gap (rad/s)
q_1	0.05	0.07
q_3	0.05	0.06
q_1	0.5	0.9
q_3	0.5	0.8
q_1	5	1.37
q_3	5	1.44
$0.78q_3 + 0.22q_4$	5	1.40

Table 3.4: Comparing the maximum spectral gap as a function of the point mass m_a

deflections in the various principle modes

$$y(z,t) \quad = \quad \sum_{k=1}^{\infty} \psi_k(z)\varphi_k(t) \tag{3.28}$$

in which $\psi_k(z)$ is

$$\psi_k(z) = \sin \frac{k\pi z}{L} \tag{3.29}$$

with L the length of the beam. Assume a singular harmonic load $P(z,t)$ applied at z_0

$$P(z,t) = Fe^{i\omega t}\delta(z - z_0). \tag{3.30}$$

The frequency response function H_{VV} between a singular harmonic load $P(z,t)$ applied at V and the response at point V is given by [22]

$$H_{VV}(\omega) \triangleq \sum_{k=1}^{\infty} \frac{\psi_k(V)\psi_k(V)}{a(\omega_k^2 - \omega^2)} \tag{3.31}$$

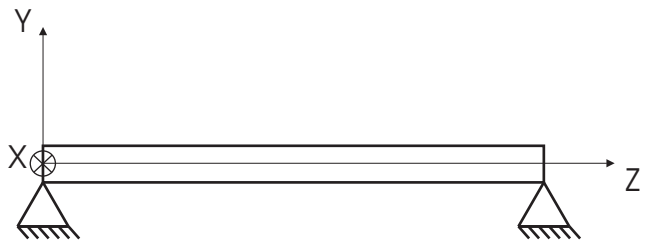

Figure 3.7: Transversely vibrating uniform beam

with $a = \frac{A\rho L}{2}$. The eigenfrequencies ω_k are given by

$$\omega_k = \frac{k^2\pi^2}{L^2}\sqrt{\frac{EI}{\rho A}}. \tag{3.32}$$

The parameters of the beam and the corresponding 5 lowest eigenfrequencies are given in Table 3.5. Equation (3.31) is substituted into Eq. (3.3) to obtain the

beam parameters	ρ (kg/m^3)	A (m^2)	L (m)	E (N/m^2)	I (m^4)
	7800	4×10^{-4}	1	2×10^{11}	3.33×10^{-9}
eigenfrequencies	ω_1 (rad/s)	ω_2 (rad/s)	ω_3 (rad/s)	ω_4 (rad/s)	ω_5 (rad/s)
	144.3	577.1	1298.4	2308.3	3606.8

Table 3.5: Beam parameters

eigenfrequencies of the system with absorber. Assume a resonant condition for the third mode $\omega_3 = 1298.4$ rad/s. According to the single mode approach, the best location for the absorber is where $\psi_3(z)$ reaches a maximum, with $\psi_3(z) = \sin\frac{3\pi z}{L}$. As $\psi_3(z)$ has three equal maxima at $z = \frac{1}{6}L$, $z = \frac{1}{2}L$, $z = \frac{5}{6}L$, the single mode approach does not distinguish between these three locations. However, for larger absorber masses the neighboring modes become important. As can be seen in Fig. 3.8, the activity of the neighboring modes ($\psi_2(z)$ and $\psi_4(z)$) is much higher at $z = \frac{1}{6}L$ and $z = \frac{5}{6}L$ than it is at $z = \frac{1}{2}L$. Hence for larger absorber masses $z = \frac{1}{2}L$ becomes optimal as can be seen from the spectral gap given in Table 3.6. The same results hold when a point mass is added (Table 3.7). However, compared to the absorber, the spectral gaps are much smaller for a given m_a. As a result, the difference between locations $z = \frac{1}{6}L$ and $z = \frac{1}{2}L$ is only apparent for much higher point masses m_a.

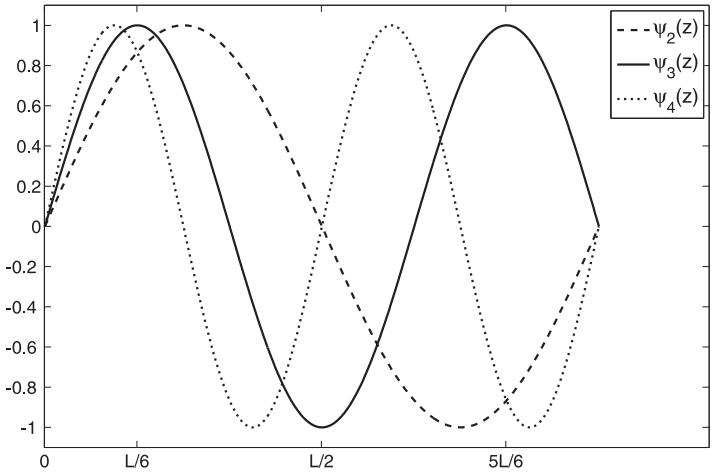

Figure 3.8: Eigenfunctions $\psi_2(z)$, $\psi_3(z)$, $\psi_4(z)$

z	m_a (kg)	ω_a (rad/s)	max. spectral gap (rad/s)	neighb. anti reson. (rad/s)
$\frac{1}{6}L$	0.05	1247	155	965-2034
$\frac{1}{2}L$	0.05	1245	157	908-2308
$\frac{1}{6}L$	0.5	1019	315	965-2034
$\frac{1}{2}L$	0.5	1011	344	908-2308

Table 3.6: Comparing the maximum spectral gap as a function of the absorber mass m_a

z	m_a (kg)	max. spectral gap (rad/s)	neighb. anti reson. (rad/s)
$\frac{1}{6}L$	0.05	10	965-2034
$\frac{1}{2}L$	0.05	10	908-2308
$\frac{1}{6}L$	0.5	82	965-2034
$\frac{1}{2}L$	0.5	82	908-2308
$\frac{1}{6}L$	5	263	965-2034
$\frac{1}{2}L$	5	285	908-2308

Table 3.7: Comparing the maximum spectral gap as a function of the point mass m_a

3.7 Conclusion

This chapter was concerned with obtaining a resonance free zone by attaching an undamped dynamic vibration absorber. An important design parameter in this matter is the attachment location which is typically determined using a single mode approach, i.e. only one vibration mode is taken into account. Here, this single mode approach has been extended to a more general multi mode approach which takes into account the influence of the neighboring vibration modes as well. An important indication of their influence is shown to be given by the neighboring antiresonances, information which is implemented in a clear selection procedure for the attachment location.

4

Relocating antiresonances

4.1 Introduction

Although resonances still deserve the main attention in a vibration engineering design, antiresonances undoubtedly offer great possibilities when it comes to vibration reduction. As already mentioned in Chapter 2, antiresonances are the zeros of the frequency response function H_{RS}, defining points of zero vibration at response location R when the structure is harmonically excited at location S. This feature can prove useful when for instance sensitive equipment needs to be protected from troublesome vibrations.

Starting from an initial design of the mechanical structure, the main goal is to alter the structure such that an antiresonance is relocated to the desired response location, thereby completely suppressing the excitation frequency at that point. This means that assigning resonances fits in the framework of the ill-posed inverse problem such that a solution might not always exist.

To clarify this issue, it is of paramount importance to understand how antiresonances are created and how they can be altered. These necessary insights are provided by appropriately applying the substructure decoupling technique introduced in Chapter 2. It is shown that the problem of relocating antiresonances is exactly equivalent to the problem of relocating resonances. Hence, all the results of Chapter 3 can be reused. This is especially convenient when deciding where to modify the structure, again a crucial issue in this chapter. First, the standard practice for assigning antiresonances is outlined in Section 4.2.

4.2 Assigning antiresonances

We consider two extremes. The first one is structural modification which implies that every mass and stiffness element can be altered to obtain the desired modal changes, i.e. a global modification. The number of DOFs however remains unaltered. The other extreme is attaching a dynamic vibration absorber where only one coordinate is involved, i.e. a local modification. Because the absorber increases the number of DOFs, a different approach is required.

4.2.1 Structural modification

Consider the FRF matrix H of a linear undamped mechanical structure

$$H(\omega) = (K - M\omega^2)^{-1} \tag{4.1}$$

$$= \frac{\text{adj}(K - M\omega^2)}{\det(K - M\omega^2)} \tag{4.2}$$

with M and K the mass and stiffness matrices respectively. The ij^{th} element of matrix H, denoted as $H(i,j)$ can be written as

$$H(\omega)(i,j) = (-1)^{i+j} \frac{\det(K_{\not i\not j} - M_{\not i\not j}\omega^2)}{\det(K - M\omega^2)} \tag{4.3}$$

where $K_{\not i\not j}$ and $M_{\not i\not j}$ are derived from K and M by deleting row i and column j. From Eq. (4.3) it is clear that the zeros or antiresonances of $H(i,j)$ are given by the positive roots of

$$\det(K_{\not i\not j} - M_{\not i\not j}\omega^2) = 0. \tag{4.4}$$

The positive roots of Eq. 4.4 are typically interpreted as the resonances of a fictitious system with mass and stiffness matrices $M_{\not i\not j}$ and $K_{\not i\not j}$ [1]. This consequently transforms the problem of assigning the antiresonances of $H(i,j)$ to the problem of assigning the resonances or poles of the fictitious system formed by $M_{\not i\not j}$ and $K_{\not i\not j}$.

Subsequently, for general changes $\Delta M_{\not i\not j}$ and $\Delta K_{\not i\not j}$ to the mass and stiffness matrices $M_{\not i\not j}$ and $K_{\not i\not j}$ of the fictitious system, a necessary and sufficient condition for the assignment of a resonance ω_r is given by Eq. (4.5)

$$\{(K_{\not i\not j} + \Delta K_{\not i\not j}) - (M_{\not i\not j} + \Delta M_{\not i\not j})\omega_r{}^2\}X = 0 \tag{4.5}$$

where X denotes the eigenvector of the eigenvalue problem. Equation (4.5) can be rewritten as follows

$$\{\Delta K_{\not i\not j} - \Delta M_{\not i\not j}\omega_r^2\}X = -\{K_{\not i\not j} - M_{\not i\not j}\omega_r^2\}X \tag{4.6}$$

$$X = (K_{\not i\not j} - M_{\not i\not j}\omega_r^2)^{-1}(\Delta M_{\not i\not j}\omega_r^2 - \Delta K_{\not i\not j})X \tag{4.7}$$

$$X = H_f(\omega_r)(\Delta M_{\not i\not j}\omega_r^2 - \Delta K_{\not i\not j})X \tag{4.8}$$

with H_f the transfer function matrix of the fictitious system.

Eq. (4.8) can also address two special types of modification, namely a point mass m_a and a grounded spring k_a, which are actually local modifications. When attached to degree of freedom k, their values can be calculated by reducing Eq. (4.8) to

$$m_a = \frac{1}{\omega_r^2 H_f(\omega_r)(k,k)} \tag{4.9}$$

$$k_a = -\frac{1}{H_f(\omega_r)(k,k)}. \tag{4.10}$$

Because H_f belongs to a fictitious system it cannot be measured in practice. As a result, a finite element model (FEM) is required for these calculations. An alternative method applicable for local structural changes that does allow the use of measurements is given in the next Section.

4.2.2 Local modification

When only local modifications (vibration absorber, point mass and grounded spring) are considered, the problem of assigning antiresonances can be described more elegantly. Consider to this end the linear undamped structure of Fig. 2.3 subject to harmonic loading at location S. Is it possible to create an antiresonance at location R by locally modifying the structure at location V? According to Lemma 2.3, outlined in Chapter 2, the FRF of the modified structure can be written as a function of FRFs of the unmodified structure as follows

$$\hat{H}_{RS}(\omega) = H_{RS}(\omega) - \frac{H_{RV}(\omega)H_{VS}(\omega)}{H_{VV}(\omega) + H_{AA}(\omega)}$$

with

$$H_{AA}(\omega) = \frac{\omega^2 - \omega_a^2}{m_a\omega^2\omega_a^2}; \qquad \omega_a^2 = \frac{k_a}{m_a}.$$

Regarding the vibration absorber, the absorber stiffness k_a that assigns an antiresonance at frequency ω_r (such that $\hat{H}_{RS}(\omega_r) = 0$) can be determined as a function of m_a and V

$$k_a = \frac{H_{RS}(\omega_r)m_a\omega_r^2}{H_{RS}(\omega_r) - m_a\omega_r^2[H_{RS}(\omega_r)H_{VV}(\omega_r) - H_{VS}(\omega_r)H_{RV}(\omega_r)]}. \tag{4.11}$$

For a point mass m_a ($k_a \to \infty$) this becomes

$$m_a = \frac{H_{RS}(\omega_r)}{\omega_r^2[H_{RS}(\omega_r)H_{VV}(\omega_r) - H_{VS}(\omega_r)H_{RV}(\omega_r)]} \tag{4.12}$$

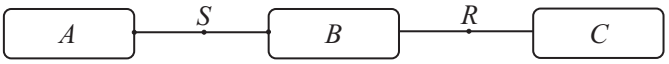

Figure 4.1: Decoupling the main system into three subsystems A, B and C

while for a grounded spring ($m_a \to \infty$)

$$k_a = \frac{H_{RS}(\omega_r)}{-m_a\omega_r^2[H_{RS}(\omega_r)H_{VV}(\omega_r) - H_{VS}(\omega_r)H_{RV}(\omega_r)]}. \tag{4.13}$$

The advantage of using Eqs. (4.11-4.13) is that the required parameters k_a and m_a can be determined with measured FRFs while in the previous section a FEM was required. For both sections however, two important questions remain unanswered:

1. When do Eqs. (4.8-4.10) and (4.11-4.13) yield practically useful solutions? For instance, Eq.(4.11) only yields practically useful solutions if $k_a > 0$. This means that when the absorber mass m_a and the attachment location V are chosen a priori, it is not always possible to assign an antiresonance at frequency ω_r.

2. What is the best attachment location V for the absorber ? In the methods outlined above, the attachment location was assumed to be chosen a priori.

To clarify these issues, a substructure decoupling technique is introduced in Section 4.3.

Remark It is well known that for two special attachment locations, namely $V = R$ and $V = S$, every antiresonance can be assigned by designing the absorber such that $k_a = m_a\omega_r^2$. Indeed, for both cases Eq. (4.11) reduces to

$$k_a = m_a\omega_r^2 \tag{4.14}$$

which for $m_a > 0$, always yields feasible solutions $k_a > 0$ regardless of ω_r.

4.3 Substructure decoupling technique

We assume that the main structure can be subdivided into three subsystems connected at the response location R and the force location S as shown in Fig. 4.1. It is important to note that the interconnections at R and S are limited to a single coordinate. In this case, the following relationship between the FRF of the full system and the FRFs of the subsystems A, B and C can be derived

$$[H_{A+B+C}]_{RS} = \frac{[H_A]_{SS}[H_B]_{RS}[H_C]_{RR}}{[H_B]_{RR}[[H_A]_{SS} + [H_B]_{SS}] - [H_B]_{SS}[H_B]_{RS}}. \tag{4.15}$$

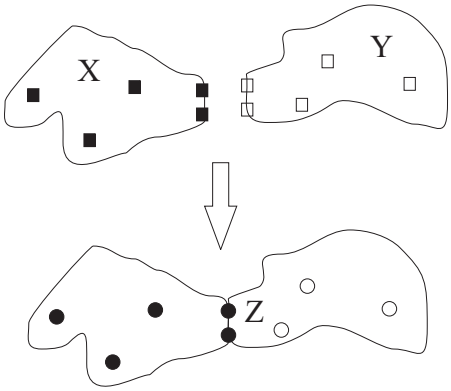

Figure 4.2: Coupling systems X and Y

Indeed, consider subsystems A, B and C as separate systems each having their own FRF matrices $[H_A], [H_B]$ and $[H_C]$ respectively. By attaching system A to system B the FRF $[H_B]_{RS}$ is altered according to Eq. (2.3) with $V = S$

$$[H_{A+B}]_{RS} = [H_A]_{RS} - \frac{[H_A]_{RS}[H_A]_{SS}}{[H_A]_{SS} + [H_B]_{SS}} \tag{4.16}$$

where $[H_{A+B}]$ denotes the FRF matrix of the system $A + B$ comprising of subsystems A and B. Attaching system C to system $A + B$ changes $[H_{A+B}]_{RS}$ into $[H_{A+B+C}]_{RS}$ as follows

$$[H_{A+B+C}]_{RS} = [H_{A+B}]_{RS} - \frac{[H_{A+B}]_{RR}[H_{A+B}]_{RS}}{[H_{A+B}]_{RR} + [H_C]_{RR}}. \tag{4.17}$$

Finally, substituting Eq. (4.16) into Eq. (4.17) and rearranging yields Eq. (4.15).

Equation (4.15) shows that the problem of assigning antiresonances to $[H_{A+B+C}]_{RS}$ can be reformulated as the problem of assigning antiresonances to the receptances $[H_A]_{SS}$, $[H_B]_{RS}$ and $[H_C]_{RR}$ of the different subsystems.

Remark A general substructure coupling technique where the coupling involves more than one coordinate is explained in [23]. Systems X and Y are coupled through a set of coupling coordinates yielding the assembled system Z (Figure 4.2). The FRFs of the overall system Z can be written as a function of the FRFs of the

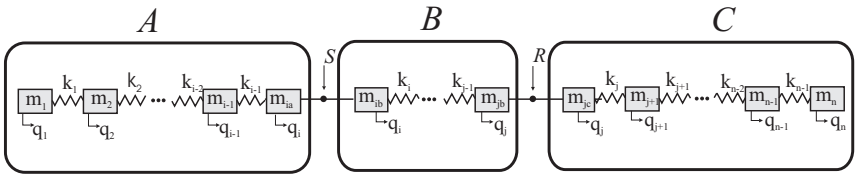

Figure 4.3: Decoupling the main system into three subsystems A, B and C

subsystems X and Y (dependence on ω is omitted for clarity)

$$[H_Z]_{PP} = [H_X]_{PP} - [H_X]_{PS}([H_X]_{SS} + [H_Y]_{SS})^{-1}[H_X]_{SP} \tag{4.18}$$
$$[H_Z]_{PP} = [H_X]_{PS}([H_X]_{SS} + [H_Y]_{SS})^{-1}[H_Y]_{SS} \tag{4.19}$$
$$[H_Z]_{PT} = [H_X]_{PS}([H_X]_{SS} + [H_Y]_{SS})^{-1}[H_Y]_{ST} \tag{4.20}$$
$$[H_Z]_{SS} = [H_X]_{SS}([H_X]_{SS} + [H_Y]_{SS})^{-1}[H_Y]_{SS} \tag{4.21}$$
$$[H_Z]_{ST} = [H_X]_{SS}([H_X]_{SS} + [H_Y]_{SS})^{-1}[H_Y]_{ST} \tag{4.22}$$
$$[H_Z]_{TT} = [H_Y]_{TT} - [H_Y]_{TS}([H_X]_{SS} + [H_Y]_{SS})^{-1}[H_Y]_{ST}. \tag{4.23}$$

In Eqs. (4.18-4.23) S denotes the set of coupling coordinates, P and T denote the set of free coordinates corresponding to systems X and Y respectively. Note that Eqs. (4.18-4.23) define a relation between FRF matrices, e.g. $[H_Z]_{PP} \in \mathbb{C}^{P\times P}$.

4.3.1 Unbranched systems

Before deriving any general conclusions, let's first apply Eq. (4.15) to the simplest system possible, i.e. an unbranched system[1]. As displayed in Fig. 4.3 an unbranched system consists of a series connection of springs and masses. After dividing the entire system into three subsystems A, B and C at locations S and R, the corresponding FRF matrices are given by

$$[H_A] = \begin{bmatrix} k_1 - m_1\omega^2 & -k_1 & & & \\ -k_1 & k_1 + k_2 - m_2\omega^2 & -k_2 & & \\ & \ddots & \ddots & \ddots & \\ & & -k_{i-2} & k_{i-2} + k_{i-1} - m_{i-1}\omega^2 & -k_{i-1} \\ & & & -k_{i-1} & k_{i-1} - m_{ia}\omega^2 \end{bmatrix}^{-1} \tag{4.24}$$
$$\triangleq (K_A - M_A\omega^2)^{-1} \tag{4.25}$$

[1] An important practical example are unbranched drive trains subject to torsional vibrations.

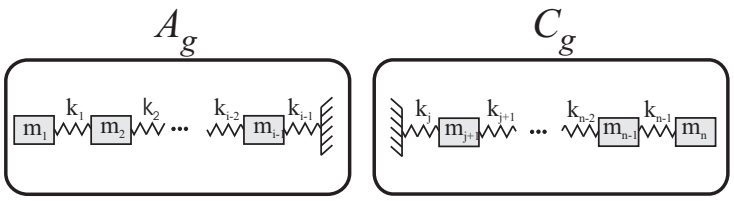

Figure 4.4: Grounded subsystems A_g and C_g

$$[H_B]= \begin{bmatrix} k_i - m_{ib}\omega^2 & -k_i & & \\ -k_i & k_i + k_{i+1} - m_{i+1}\omega^2 & -k_{i+1} & \\ & \ddots & \ddots & \ddots \\ & -k_{j-2} & k_{j-2} + k_{j-1} - m_{j-1}\omega^2 & -k_{j-1} \\ & & -k_{j-1} & k_{j-1} - m_{jb}\omega^2 \end{bmatrix}^{-1} \tag{4.26}$$

$$\triangleq (K_B - M_B\omega^2)^{-1} \tag{4.27}$$

$$[H_C]= \begin{bmatrix} k_j - m_{jc}\omega^2 & -k_j & & \\ -k_j & k_j + k_{j+1} - m_{j+1}\omega^2 & -k_{j+1} & \\ & \ddots & \ddots & \ddots \\ & -k_{n-2} & k_{n-2} + k_{n-1} - m_{n-1}\omega^2 & -k_{n-1} \\ & & -k_{n-1} & k_{n-1} - m_n\omega^2 \end{bmatrix}^{-1} \tag{4.28}$$

$$\triangleq (K_C - M_C\omega^2)^{-1}. \tag{4.29}$$

The antiresonances of $[H_A]_{SS}$ are given by deleting both row and column corresponding to point S in Eq. (4.24) and taking the determinant. Hence, the antiresonances of $[H_A]_{SS}$ are given by the resonances of subsystem A when grounded at spring k_{i-1}. The same analysis holds for subsystem C, i.e. the antiresonances of $[H_C]_{RR}$ are given by the resonances of subsystem C when grounded at spring k_j. As R and S denote the first and last coordinate of subsystem B, $[H_B]_{RS}$ has no antiresonances.

In conclusion: The antiresonances of $[H_{A+B+C}]_{RS}$ correspond to the resonances of the grounded subsystems A_g and C_g shown in Fig. 4.4. Consequently, both subsystems can be regarded as MDOF vibration absorbers, generalizing the SDOF absorber which typically assigns only one antiresonance.

Remark This interesting result is derived in an alternative way in [24] where it is shown that:

$$H_{RS}(\omega) = \alpha_{RS} \frac{\prod_{k=1}^{i-1} (\omega^2 - \hat{\mu}_k^2) \prod_{k=j+1}^{n} (\omega^2 - \tilde{\mu}_k^2)}{\prod_{k=1}^{n} (\omega^2 - \mu_k^2)}. \tag{4.30}$$

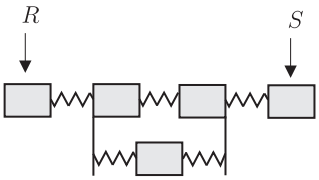

Figure 4.5: $[H_B]_{RS}$ featuring antiresonances although R and S are far away from each other

In (4.30) α_{RS} is a constant, $\hat{\mu}_k$ are the eigenfrequencies of subsystem A when grounded at point S, $\tilde{\mu}_k$ are the eigenfrequencies of subsystem C when grounded at point R and μ_k are the eigenfrequencies of the overall system.

4.3.2 General systems

The above derived conclusions for unbranched systems can easily be extended to more general branched systems, i.e. systems where coordinates are coupled with more than two other coordinates. The only requirement is that subsystems A and C are connected to subsystem B with a single coordinate. In this case, A_g and C_g can still be regarded as MDOF vibration absorbers regardless of their structure. However, one distinction exists. As opposed to unbranched systems, subsystem B can also introduce antiresonances to $[H_{A+B+C}]_{RS}$. Indeed, for general subsystems B, $[H_B]_{RS}$ can have antiresonances despite the fact that R and S are far away from each other. One such example is shown in Fig. 4.5.

Before we actually assign antiresonances to $[H_{A+B+C}]_{RS}$, let's recapture the main advantages of using the subdivision:

- The main problem is broken down into three smaller problems.
- Improved insight in the problem: subsystems A and C work as MDOF absorbers.
- As opposed to the fictitious systems generally introduced when assigning antiresonances all three subsystems are real, e.g. the corresponding eigenvectors retain a physical meaning.
- If the subdivision can be realized physically, one can use measurements of the different subsystems.
- Regarding subsystems A and C, assigning antiresonances is reformulated to assigning resonances which permits to reuse the analysis of Chapter 3 in determining the best suitable location for modifying the structure.

4.4 Assigning antiresonances

Because the analysis for A and C (Figure 4.1) is similar, they are discussed together hereafter. The analysis of subsystem B differs from that of A and C and is discussed separately.

4.4.1 Subsystems A and C

Assigning antiresonances to $[H_A]_{SS}$ and $[H_C]_{RR}$ corresponds to assigning resonances to their grounded equivalents $\mathrm{A_g}$ and $\mathrm{C_g}$ (Figure 4.4). This means the resonances of $\mathrm{A_g}$ or $\mathrm{C_g}$ need to be relocated to the required antiresonances of $[H_{A+B+C}]_{RS}$ by modifying the structure at location V. The procedure differs depending on the availability of a FEM (finite element model) of the structure.

FEM available When a FEM of the structure is available the procedure is as follows:

1. Create the grounded subsystems A_g and C_g from A and C.
2. Determine the optimal location for modification as described in Section 3.4 of Chapter 3.
3. Assign the antiresonance ω_r to $[H_{A+B+C}]_{RS}$, i.e. assign the resonance ω_r to Ag or Cg by solving Eq. (3.3) of Chapter 3 for A_g and C_g:

$$1 + m_a \frac{{\omega_r}^2 \omega_a^2}{{\omega_r}^2 - \omega_a^2} [H_{A_g}]_{VV}(\omega_r) = 0 \tag{4.31}$$

$$1 + m_a \frac{{\omega_r}^2 \omega_a^2}{{\omega_r}^2 - \omega_a^2} [H_{C_g}]_{VV}(\omega_r) = 0. \tag{4.32}$$

For a realistic absorber mass m_a, the solvability of this equation decreases when the difference between an existing resonance and the required resonance ω_r becomes larger. In literature, the only studies that report on this subject are based on a graphical representation of Eq. (3.3) [25–27].

FEM not available If subsystems A and C can be physically decoupled from subsystem B, the procedure outlined above can be repeated by measuring $[H_{A_g}]$ and $[H_{C_g}]$. In practice however, accurate measurements of $[H_{A_g}]$ and $[H_{C_g}]$ are not possible because A_g and C_g require a perfect clamping which is physically not realizable. In what follows, we show how accurate measurements of A and C can be used to obtain the eigenvectors and antiresonances of A_g and C_g needed in step 2 as well as $[H_{A_g}]_{VV}(\omega_r)$ and $[H_{C_g}]_{VV}(\omega_r)$ required in step 3. Because the derivation is exactly the same for both A_g and C_g, only A_g is considered from hereon.

As outlined in [28] the eigenvectors of the grounded system A_g (assume system A is grounded at coordinate n) can be derived from Eq. (4.33) which holds for the ungrounded system A:

$$[Z_A](\omega)[H_A](\omega) = [I_n] \tag{4.33}$$

where $[I_n]$ is the identity matrix of dimension n and $[Z_A]$ the dynamic flexibility matrix:

$$[Z_A](\omega) = (K_A - \omega^2 M_A). \tag{4.34}$$

If Eq. (4.33) is evaluated at ω_r, an antiresonance of $[H_A](n,n)$ (i.e. $[H_A](n,n)(\omega_r) = 0$), and if only column n of $[H_A]$ is considered, one obtains

$$[Z_A](\omega_r) \begin{bmatrix} [H_A](1,n)(\omega_r) \\ [H_A](2,n)(\omega_r) \\ \vdots \\ [H_A](n-1,n)(\omega_r) \\ [H_A](n,n)(\omega_r) \end{bmatrix} = \begin{bmatrix} 0 \\ 0 \\ \vdots \\ 0 \\ 1 \end{bmatrix}. \tag{4.35}$$

Because $[H_A](n,n)(\omega_r) = 0$, following Eq. (4.36) also holds

$$[Z_A]_{\not{n}\not{n}}(\omega) \begin{bmatrix} [H_A](1,n)(\omega) \\ [H_A](2,n)(\omega) \\ \vdots \\ [H_A](n-1,n)(\omega) \end{bmatrix} = \begin{bmatrix} 0 \\ 0 \\ \vdots \\ 0 \end{bmatrix}. \tag{4.36}$$

In Eq. (4.36), $[Z_A]_{\not{n}\not{n}}$ is the dynamic flexibility matrix corresponding to the grounded system A_g. Because ω_r is a resonance of A_g this means that

$$[[H_A](1,n)(\omega_r)[H_A](2,n)(\omega_r)\dots[H_A](n-1,n)(\omega_r)]^T \tag{4.37}$$

is an eigenvector of A_g corresponding to this resonance.[2]

To determine the antiresonances of A_g, first consider the FRFs of A_g as a function of the FRFs of A by means of Eqs. (2.3,2.4)

$$[H_{A_g}]_{R_a S_a} = [H_A]_{R_a S_a} - \lim_{k_a \to \infty} \frac{[H_A]_{R_a V_a}[H_A]_{S_a V_a}}{[H_A]_{V_a V_a} + \frac{1}{k_a}} \tag{4.38}$$

$$= \frac{[H_A]_{R_a S_a}[H_A]_{V_a V_a} - [H_A]_{R_a V_a}[H_A]_{S_a V_a}}{[H_A]_{V_a V_a}} \tag{4.39}$$

where subscript a is introduced in R_a, S_a and V_a to distinguish them from R, S and V from the initial problem. A_g is grounded at location $V_a = S$ such that Eq. (4.38) becomes:

$$[H_{A_g}]_{R_a S_a} = \frac{[H_A]_{R_a S_a}[H_A]_{SS} - [H_A]_{R_a S}[H_A]_{S_a S}}{[H_A]_{SS}} \tag{4.40}$$

[2] In general the eigenvalue problem of A_g is given by $([K_A]_{\not{n}\not{n}} - \omega_i^2 [M_A]_{\not{n}\not{n}})e_i = 0$.

Finally, the antiresonances of A_g can be determined by solving Eq. (4.41) which contains measured FRFs of A:

$$[H_A]_{R_a S_a}[H_A]_{SS} - [H_A]_{R_a S}[H_A]_{S_a S} = 0 \tag{4.41}$$

With the above derived eigenvectors and antiresonances of system A_g, a suitable location can be determined according to Section 3.4. Subsequently, Eqs. (4.31-4.32) can be used to assign the antiresonance by means of Eq. (4.40). Similar to the case where a FEM is available, the solvability of these equations should be checked graphically.

4.4.2 Subsystem B

Since R and S are located far away from each other, H_{RS} features little or no antiresonances (cfr. Fig. 4.5). Consequently, in most cases new antiresonances will have to be created, rather than relocating the few existing ones. In the special case of unbranched systems (Section 4.3.1), the analysis is severely simplified. Indeed, assigning an antiresonance ω_r to $[H_B]_{RS}$ can be achieved by attaching an undamped vibration absorber, tuned to ω_r, anywhere along subsystem B.

More precisely, consider Fig. 4.3. Suppose an undamped vibration absorber tuned to ω_r is attached to subsystem B at coordinate l with $i \leq l \leq j$. Because there is only one dynamic path (i.e. a one-to-one connection), the absorber effectively blocks frequency ω_r not only at its attachment location, but also at every coordinate $k > l$.

4.5 Pole-zero cancellation

A resonance that coincides with an antiresonance (equivalent to a pole that coincides with a zero) is known as a pole-zero cancellation [29]. As stated in Theorem 2, a pole-zero cancellation at frequency ω_k corresponds to a vibration node for mode k at the location of the zero, resulting in low vibration amplitudes. Therefore, a possible vibration reduction approach is to relocate a resonance ω_k to an antiresonance.

When the structure can be divided into substructures A, B and C as displayed in Fig. 4.1, creating a pole-zero cancellation becomes much more convenient. Indeed, the antiresonances of H_{RS} are mainly given by the resonances of the grounded subsystems A_g and C_g. Consequently, a pole-zero cancellation can be created by leaving subsystem C (and the antiresonances it provides to H_{RS}) unaltered while modifying the structure at subsystems A and B (and relocating in this way the resonances). The same conclusion holds when leaving A unaltered while changing B or C.

There is also another way of looking at this problem. At a vibration node for mode k, the system can be decoupled into two subsystems where each subsystem

is grounded at the vibration node. Therefore, ω_k is not only a natural frequency of the entire system but also of the two subsystems separately. This means that a vibration node can be created at location R by assigning the same resonance to both grounded subsystems $(A+B)_g$ and C_g. On the other hand, a vibration node at S can be created by assigning the same resonance to grounded subsystems A_g and $(B+C)_g$.

4.6 Conclusion

An important vibration control option is the creation of antiresonances, i.e. points of zero vibration on the structure. Using a substructure coupling technique, the initial system is cut into three smaller subsystems. Subsequently, it is shown that two of these subsystems work as MDOF vibration absorbers which means that their resonances define antiresonances for the total system. As a result, the assignment of antiresonances is shown to be equivalent to the assignment of resonances. Moreover, both subsystems are physical systems such that also measurements can be used when performing the assignment. This is an important advantage over the classical approach to assigning antiresonances which is typically transformed to assigning the resonances of a virtual system.

The assignment of antiresonances fits in the framework of the inverse problem and has therefore no guaranteed solution. A first approximation is to tackle the corresponding direct problem, i.e. to relocate the antiresonances *towards* the desired outcome with a minimum amount of modification to the structure, e.g. a minimum amount of absorber mass. Because this is equivalent to relocating resonances, the attachment location for the absorber can be determined according to Chapter 3. Solving this direct problem shows the amount of relocation that can be achieved and whether or not the actual antiresonance assignment is possible.

Part II

The nonlinear dynamic vibration absorber

5

A dimensionless approach to nonlinear vibration absorber tuning

5.1 Introduction

Although linear vibration absorbers offer great possibilities in mitigating vibrations, they are only capable of achieving this in a narrow frequency bandwidth. Consequently, they loose effectiveness when the excitation frequency varies or when MDOF systems (featuring multiple natural frequencies) are considered. To increase the frequency bandwidth in which the absorber is effective, different nonlinear spring characteristics have been introduced. The first study in this matter was performed by Roberson [30] who proposed a dynamic vibration absorber with a weakly nonlinear spring characteristic, i.e. a linear spring with small cubic nonlinearity. For an undamped forced main system, he showed that this nonlinear absorber is capable of reducing the vibrations over a larger frequency bandwidth compared to its linear counterpart. This result paved the way in the use of nonlinear vibration absorbers as frequency robust mitigating devices.

More recently, absorbers with a *strongly* nonlinear spring characteristic have been investigated where strongly nonlinear refers to a nonlinearizable spring, e.g. a spring with cubic nonlinearity [12]. Although very complicated dynamics occur even in the simplest system possible [31], [32] (a linear SDOF primary system with attached to it a vibration absorber with cubic spring), strongly nonlinear vibration absorbers offer two interesting advantages that are not possible for linear and weakly nonlinear absorbers. One advantage is that the vibration energy can be transferred

between different nonlinear normal modes [1]. As shown in [11] this enables the localization of the energy to a certain part of the system creating in this way a so called nonlinear energy sink (NES). Secondly, a strongly nonlinear absorber has no preferential frequency enabling vibration reduction at virtually every frequency.

Besides these advantages, which are promising concepts in the field of vibration reduction, some difficulties arise when using nonlinearizable vibration absorbers. One important drawback is the existence of a so called *energy threshold* as explained by [33] where a cubic spring absorber is attached to a linear SDOF system under transient forcing. For an absorber initially at rest (which is of practical importance in many applications), the authors show that a minimum amount of input energy into the primary system is required for the absorber to work properly. In other words, this energy threshold separates regions with weak and strong absorber movement, respectively corresponding to weak and strong vibration reduction. Moreover, the transition between those regions appears to be discontinuous, i.e. a small increase in input energy results in a large increase in absorber movement. This phenomenon forms a crucial aspect of the tuning procedure of strongly nonlinear vibration absorbers and is therefore analyzed in detail in this chapter.

The value of the energy threshold is dependent on the physical properties (stiffness and mass) of the primary system and the absorber. It can be determined by means of a bifurcation analysis as explained in [33] which is limited to primary systems with natural frequency $\omega_0 = 1$. An extended version of this analysis for general linear primary systems ($\omega_0 \neq 1$) is presented in Section 5.3.

In Section 5.4 we propose a different analysis capable of explaining the threshold phenomenon in a dimensionless setting. The advantage of our approach is that all the influencing parameters (stiffness, mass and initial conditions) are joined into one dimensionless parameter. Consequently, the bifurcation analysis presented in Section 5.4 covers every possible combination of parameters while the analysis in [33] is only valid for one particular system. Moreover, the concept of an energy threshold is extended to a more general *parameter threshold*. This means that each parameter is featuring its own threshold value as a function of the other parameters in a closed form expression. Furthermore, the same approach can also provide threshold values for noncubic absorber springs, nonlinear primary systems and even forced linear primary systems as shown in Section 5.5. Its general applicability renders it as a powerful tool in the further development and understanding of nonlinear vibration absorbers.

Before we delve into the theoretical analyzes of Sections 5.3 and 5.4, the existence of threshold values[2] is numerically demonstrated in Section 5.2. We also introduce the concept of *frequency-energy dependence* which is the key to under-

[1] Nonlinear normal modes (NNMs) correspond to periodic solutions of the system and are the nonlinear counterpart of linear vibration modes.

[2] The numerical evidence is limited to the existence of an energy threshold. Other parameter thresholds exist as well as shown in Section 5.4.

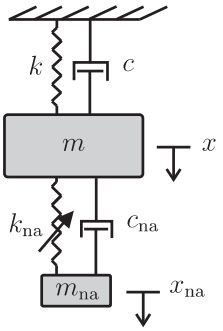

Figure 5.1: Nonlinear absorber attached to a linear SDOF system

standing the dynamics of nonlinear vibration absorbers and nonlinear oscillators in general.

5.2 Hardening and softening nonlinear vibration absorbers

The system under consideration is displayed in Fig. 5.1 showing a linear single-degree-of-freedom (SDOF) system also denoted as LO (Linear Oscillator), with attached to it a vibration absorber with a nonlinear spring characteristic. Under transient forcing (response to initial conditions), the equations of motion become

$$\begin{cases} m\ddot{x} + c\dot{x} + kx + c_{\mathrm{na}}(\dot{x} - \dot{x}_{\mathrm{na}}) + k_{\mathrm{na}}\ \mathrm{sgn}(x - x_{\mathrm{na}})|x - x_{\mathrm{na}}|^p = 0 \\ m_{\mathrm{na}}\ddot{x}_{\mathrm{na}} + c_{\mathrm{na}}(\dot{x}_{\mathrm{na}} - \dot{x}) + k_{\mathrm{na}}\ \mathrm{sgn}(x_{\mathrm{na}} - x)|x_{\mathrm{na}} - x|^p = 0 \end{cases} \tag{5.1}$$

where m, c and k denote the mass, damping and stiffness of the primary system, while subscript 'na' is used for the absorber, sgn(x) refers to the sign function, equal to $+1$ if $x > 0$, 0 if $x = 0$, and -1 if $x < 0$. The degree of nonlinearity of the absorber is characterized by the rational number $p > 0$, e.g. for a cubic spring absorber $p = 3$.

5.2.1 Frequency-energy dependence

Compared to the linear vibration absorber which is limited to resonating at a single frequency, the nonlinear absorber is able to resonate at virtually every frequency due to its frequency-energy dependence. This feature stems from its nonlinear spring characteristic and can be described by deriving an equivalent natural frequency according to the harmonic balance method [34], extended to general spring characteristics by Mickens [35]. Consider to this end the undamped equation of motion of

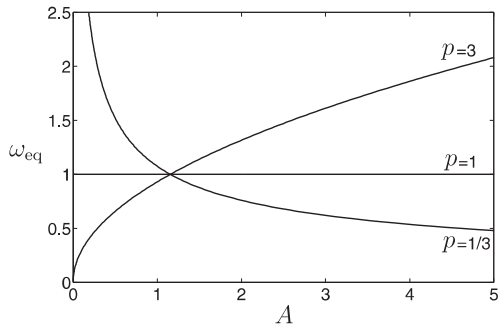

Figure 5.2: Equivalent frequency of linear and nonlinear absorbers

the nonlinear oscillator

$$m_{\rm na}\ddot{x}_{\rm na} + k_{\rm na}\ \mathrm{sgn}(x_{\rm na})|x_{\rm na}|^p = 0 \tag{5.2}$$

subject to initial conditions $\dot{x}_{\rm na}(0)$ and $x_{\rm na}(0)$. Substituting $x_{\rm na}(t) = A\sin(\omega t + \phi)$ with $A = \sqrt{x_{\rm na}(0)^2 + \dot{x}_{\rm na}(0)^2/\omega^2}$ and $\tan(\phi) = \omega x_{\rm na}(0)/\dot{x}_{\rm na}(0)$ as a solution in Eq. (5.2) (with for example $p = 3$ and $p = 1/3$), and balancing the fundamental harmonic (neglecting higher order harmonics) yields

$$p = 3: \quad A^2 = \frac{4}{3}\frac{m_{\rm na}\omega^2}{k_{\rm na}} \tag{5.3}$$

$$p = \frac{1}{3}: \quad A^2 = \frac{4}{3}\frac{k_{\rm na}^3}{m_{\rm na}^3\omega^2}. \tag{5.4}$$

In general, this relation can be written as

$$A \sim [\frac{m_{\rm na}\omega^{\frac{p+1}{2}}}{k_{\rm na}}]^{\frac{1}{p-1}}. \tag{5.5}$$

The equivalent natural frequency $\omega_{\rm eq}$ becomes

$$p = 3: \quad \omega_{\rm eq} = [\frac{3}{4}\frac{k_{\rm na}A^2}{m_{\rm na}}]^{1/2} \tag{5.6}$$

$$p = \frac{1}{3}: \quad \omega_{\rm eq} = [\frac{4}{3}\frac{k_{\rm na}^3}{m_{\rm na}^3A^2}]^{1/2}. \tag{5.7}$$

In summary, the solution of Eq. (5.2) can be approximated by $x_{\rm na}(t) = A\sin(\omega_{\rm eq}t + \phi)$ where $\omega_{\rm eq}$ increases/decreases as a function of A due to the hardening/softening character of the spring as illustrated in Fig. 5.2.

5.2.2 The existence of an energy threshold

When a nonlinear absorber is attached to a SDOF structure, it is expected to achieve optimal vibration reduction in the energy interval (determined by $\dot{x}(0)$ and $x(0)$)

that corresponds to the natural frequency ω_0 of the main system, i.e. $\omega_{eq} \approx \omega_0$. Although this is indeed the case, more complicated phenomena occur which are not present when using a linear absorber. The most important difference is the existence of an energy threshold, below which no efficient vibration reduction is possible. This is illustrated in Fig. 5.3, where a viscously damped absorber (damping factor c_{na}) with cubic spring is attached to a SDOF structure according to (5.1), for two different initial conditions. Increasing $\dot{x}(0)$ from 0.5 to 0.6 ($x(0) = 0$) with the absorber initially at rest, causes a sudden increase in both the absorber response and its efficiency in reducing vibrations. Such behavior is remarkably different from that of the linear absorber where this energy dependence is not present. The existence of an energy threshold for a cubic spring absorber is explained in detail in [33]. The most important results of this paper are summarized in Section 5.3.

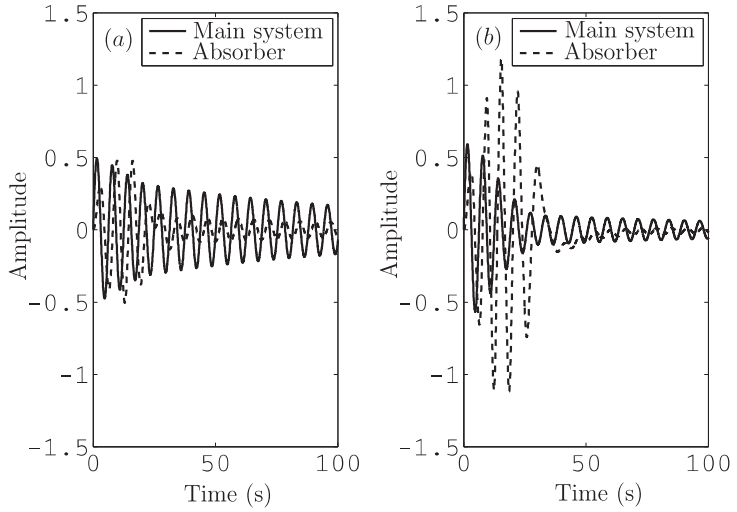

Figure 5.3: Main system and cubic absorber response
($m = 1, c = 0, k = 1, m_{na} = 0.05, c_{na} = 0.016, k_{na} = 0.067$); (a) $\dot{x}(0) = 0.5$, $x(0) = \dot{x}_{na}(0) = x_{na}(0) = 0$ (b) $\dot{x}(0) = 0.6$, $x(0) = \dot{x}_{na}(0) = x_{na}(0) = 0$

Energy thresholds are not limited to absorbers with cubic springs, they are also present in absorbers with other nonlinear spring characteristics as can be distinguished in Figs. 5.4 and 5.5 where a limited number of p-values is considered. For each initial displacement $x(0)$ of the primary system (with $\dot{x}(0) = 0$), the normalized maximum relative displacement $\mu \triangleq \frac{|x - x_{\text{na}}|_{\max}}{|x(0)|}$ attained by the absorber is displayed. The normalization, i.e. division by $|x(0)|$, provides a more useful comparison between the different initial displacements.The results are obtained through simulation of (5.1) with $m = k = 1, m_{\text{na}} = k_{\text{na}} = 0.05, c = c_{\text{na}} = 0$ and initial conditions $x(0) \neq 0, \dot{x}(0) = \dot{x}_{\text{na}}(0) = x_{\text{na}}(0) = 0$.

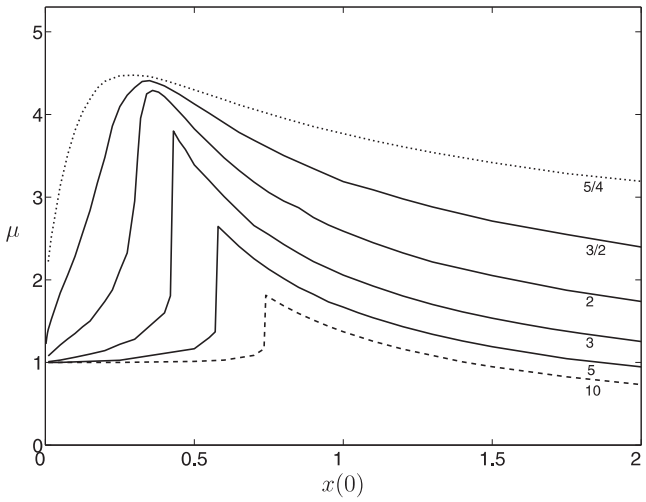

Figure 5.4: $\mu = (\frac{|x-x_{na}|_{max}}{|x(0)|})$ *as a function of* $x(0)$ *for powers* $p = [\frac{5}{4}, \frac{3}{2}, 2, 3, 5, 10]$

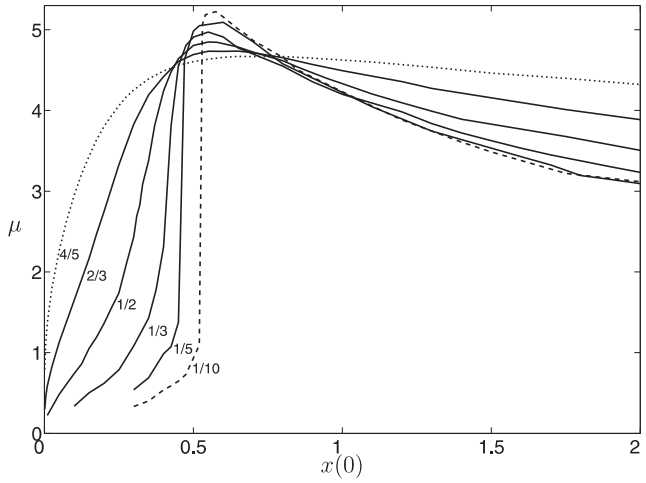

Figure 5.5: $\mu = (\frac{|x-x_{na}|_{max}}{|x(0)|})$ *as a function of* $x(0)$ *for powers* $p = [\frac{4}{5}, \frac{2}{3}, \frac{1}{2}, \frac{1}{3}, \frac{1}{5}, \frac{1}{10}]$

For hardening springs (Fig. 5.4), $\mu \to 1$ (no absorber movement) as $x(0) \to 0$ and $\mu \to 0$ (no relative movement) as $x(0) \to \infty$. In between, the different curves reach a maximum for increasing values of $x(0)$ which is more suddenly attained when further deviating from the linear spring characteristic.

For softening springs (Fig. 5.5), $\mu \to 0$ (no relative movement) as $x(0) \to 0$ and $\mu \to 1$ (no absorber movement) as $x(0) \to \infty$. The different curves also reach a maximum, although compared with hardening springs, the value of this maximum is less dependent on the power of the spring characteristic. Furthermore, it is also higher resulting in a more prominent amplitude jump at the energy threshold. Finally, for higher initial displacements, μ appears to decrease less rapidly for softening springs compared to hardening springs.

5.2.3 Theoretical analysis of the energy thresholds

To understand the existence of thresholds as numerically demonstrated in the previous section, a theoretical analysis is required. If the system is weakly damped, the analysis can be performed by considering the underlying Hamiltonian system ($c = c_{\text{na}} = 0$) of (5.1)

$$\begin{cases} \ddot{x} + \omega_0^2 x + \frac{4}{3}\epsilon\alpha(x - x_{\text{na}})^3 = 0 \\ \ddot{x}_{\text{na}} + \frac{4}{3}\alpha(x_{\text{na}} - x)^3 = 0 \end{cases} \tag{5.8}$$

with $\omega_0^2 = k/m$, $\epsilon = m_{\text{na}}/m << 1$, $\alpha = 3k_{\text{na}}/4m_{\text{na}}$. For simplicity, the analysis is limited to absorbers with cubic nonlinearity. System (5.8) is far from straightforward to analyze because it contains a strongly nonlinear term. Consequently, analyzing perturbations of the corresponding linearized system $\dot{y} = Ay$ (successively applied to many weakly nonlinear systems) is useless here as evidenced by its Jacobian matrix A evaluated in $y = (x, \dot{x}, x_{\text{na}}, \dot{x}_{\text{na}}) = (0, 0, 0, 0)$

$$A = \begin{bmatrix} 0 & 1 & 0 & 0 \\ -\omega_0^2 & 0 & 0 & 0 \\ 0 & 0 & 0 & 1 \\ 0 & 0 & 0 & 0 \end{bmatrix} \tag{5.9}$$

Besides two complex conjugate eigenvalues ($s = \pm j\omega_0$), A also has two zero eigenvalues causing a highly degenerate system supporting the complexity of its dynamics [12]. These zero eigenvalues drive the linearized system useless such that other means of analyzing (5.8) are required.

In the subsequent sections, two approaches are described. The first one, valid for a LO (linear oscillators) with natural frequency $\omega_0 = 1$ is outlined in [33]. It is reviewed in Section 5.3 and extended to general LO with $\omega_0 \neq 1$. In Section 5.4, a new approach is proposed where the 2DOF system under transient forcing is first reduced to a harmonically excited SDOF system in dimensionless form. The main advantage of this approach is its generality, i.e. all the parameters of (5.8) are joined into a single parameter that completely governs the dynamics. The novelty lies in the second approach, which is discussed in more detail.

The analysis of both approaches follows a similar procedure. First, the equations of motion are averaged which results in an accurate approximation for a limited family of response regimes. The qualitative behavior of the averaged system is then analyzed through a bifurcation analysis. This kind of analysis, which is typically used for nonlinear systems, explores the response of the nonlinear system when a certain parameter is varied. In the first approach, the bifurcation parameter is the energy-like variable r. In the second approach it is the dimensionless parameter γ. Finally, in a last step of the analysis *impulsive orbits* are considered which are defined as responses corresponding to the absorber being initially at rest ($\dot{x}_{\text{na}}(0) =$

$x_{\text{na}}(0) = 0$). Both approaches show that the threshold phenomenon is limited to impulsive orbits and only occurs when such an impulsive orbit becomes coincident with a *homoclinic orbit*.

5.3 Approximate analytical study of the energy thresholds: approach I

5.3.1 Averaged equations

A special type of the averaging method is used, namely the complexification averaging method [36] where the following transformations are applied (ρ_1, $\rho_2 \in \mathbb{C}$)

$$\rho_1 e^{j\omega_0 t} = \dot{x} + j\omega_0 x \tag{5.10}$$

$$\rho_2 e^{j\omega_0 t} = \dot{x}_{\text{na}} + j\omega_0 x_{\text{na}}. \tag{5.11}$$

Substitution of Eqs. (5.10) and (5.11) into system (5.8) yields

$$\begin{cases} \dot{\rho}_1 e^{j\omega_0 t} \\ \quad + \dfrac{j\epsilon\alpha}{6\omega_0^3}[(\rho_1 - \rho_2)e^{j\omega_0 t} - (\rho_1^* - \rho_2^*)e^{-j\omega_0 t}]^3 = 0 \\ \dot{\rho}_2 e^{j\omega_0 t} + \dfrac{j\omega_0}{2}\rho_2 e^{j\omega_0 t} - \dfrac{j\omega_0}{2}\rho_2^* e^{-j\omega_0 t} \\ \quad + \dfrac{j\alpha}{6\omega_0^3}[(\rho_2 - \rho_1)e^{j\omega_0 t} - (\rho_2^* - \rho_1^*)e^{-j\omega_0 t}]^3 = 0 \end{cases} \tag{5.12}$$

or

$$\begin{cases} \dot{\rho}_1 = -\dfrac{j\epsilon\alpha}{6\omega_0^3}[(\rho_1 - \rho_2)^3 e^{2j\omega_0 t} - 3(\rho_1 - \rho_2)^2(\rho_1^* - \rho_2^*) \\ \quad + 3(\rho_1^* - \rho_2^*)^2(\rho_1 - \rho_2)e^{-2j\omega_0 t} - (\rho_1^* - \rho_2^*)^3 e^{-4j\omega_0 t}] \\ \dot{\rho}_2 = -\dfrac{j\omega_0}{2}\rho_2 + \dfrac{j\omega_0}{2}\rho_2^* e^{-2j\omega_0 t} - \dfrac{j\alpha}{6\omega_0^3}[(\rho_2 - \rho_1)^3 e^{2j\omega_0 t} \\ \quad - 3(\rho_2 - \rho_1)^2(\rho_2^* - \rho_1^*) + 3(\rho_2^* - \rho_1^*)^2(\rho_2 - \rho_1)e^{-2j\omega_0 t} \\ \quad - (\rho_2^* - \rho_1^*)^3 e^{-4j\omega_0 t}] \end{cases} \tag{5.13}$$

where ρ_i^* denotes the complex conjugate of $\rho_i, i = 1, 2$. The outcome of System (5.13) is still exact (up till now we have only transformed the original system), but (5.13) is in a more appropriate form to apply the method of averaging. In this method, the running average of $\dot{\rho}_1$ and $\dot{\rho}_2$ is taken over one period $2\pi/\omega_0$ of the oscillation

$$\frac{\omega_0}{2\pi}\int_{t-\frac{\pi}{\omega_0}}^{t+\frac{\pi}{\omega_0}} \dot{\rho}_1(\tau)d\tau \triangleq \frac{d\bar{\rho}_1}{dt} \tag{5.14}$$

$$\frac{\omega_0}{2\pi}\int_{t-\frac{\pi}{\omega_0}}^{t+\frac{\pi}{\omega_0}} \dot{\rho}_2(\tau)d\tau \triangleq \frac{d\bar{\rho}_2}{dt} \tag{5.15}$$

When taking the running average of the left- and right-hand sides of system (5.13) the key approximation in the method of averaging is to replace ρ_1 and ρ_2 by their running averages $\bar{\rho}_1$ and $\bar{\rho}_2$. In other words ρ_1 and ρ_2 are assumed to be slowly varying (approximately constant) over one period of oscillation[3]. The resulting averaged equations or the so called *slow flow* equations become

$$\begin{cases} \frac{d\bar{\rho}_1}{dt} = -\frac{j\epsilon\alpha}{6\omega_0^3}[-3(\bar{\rho}_1 - \bar{\rho}_2)^2(\bar{\rho}_1^* - \bar{\rho}_2^*)] \\ \frac{d\bar{\rho}_2}{dt} = -\frac{j\omega_0}{2}\bar{\rho}_2 - \frac{j\alpha}{6\omega_0^3}[-3(\bar{\rho}_2 - \bar{\rho}_1)^2(\bar{\rho}_2^* - \bar{\rho}_1^*)]. \end{cases} \tag{5.16}$$

The meaning of Eqs. (5.10) and (5.11) is also clear now. Both oscillators are assumed to vibrate with the same frequency ω_0 on a fast time scale while their amplitudes ρ_1 and ρ_2 are assumed to be slowly varying, i.e. they vary on a slow time scale. As long as this is true, (5.16) provides an accurate approximation of the exact response. By writing the complex valued functions $\bar{\rho}_1$ and $\bar{\rho}_2$ in polar form, i.e. $\bar{\rho}_1 = a_1 e^{j\theta_1}$ and $\bar{\rho}_2 = a_2 e^{j\theta_2}$ and introducing ϕ as the phase difference $\phi = \theta_1 - \theta_2$, the averaged equations of (5.16) can be recast into

$$\begin{cases} \dot{a_1} = -\frac{\epsilon\alpha}{2\omega_0^3}(a_1^2 + a_2^2 - 2a_1a_2\cos\phi)a_2\sin\phi \\ \dot{a_2} = \frac{\alpha}{2\omega_0^3}(a_1^2 + a_2^2 - 2a_1a_2\cos\phi)a_1\sin\phi \\ \dot{\phi} = \frac{\omega_0}{2} - \frac{\alpha}{2\omega_0^3}(a_1^2 + a_2^2 - 2a_1a_2\cos\phi)[(1 - \frac{a_1}{a_2}\cos\phi) - \epsilon((1 - \frac{a_2}{a_1}\cos\phi))]. \end{cases} \tag{5.17}$$

By identifying two conserved quantities r and h (i.e. $\dot{r} = 0$, $\dot{h} = 0$)

$$a_1^2 + \epsilon a_2^2 = r^2 \tag{5.18}$$

$$\frac{a_1^2}{2}\omega_0 + \frac{\epsilon a_2^2}{4}\omega_0 + \frac{\epsilon\alpha}{8\omega_0^3}(a_1^2 + a_2^2 - 2a_1a_2\cos\phi)^2 = h \tag{5.19}$$

and introducing ψ as

$$\tan(\frac{\psi}{2} + \frac{\pi}{4}) = \frac{a_1}{\sqrt{\epsilon}a_2}, \quad \psi \in [-\frac{\pi}{2}, \frac{\pi}{2}] \tag{5.20}$$

two new coordinates r and ψ can be used instead of a_1 and a_2 in (5.17). The coordinate r is a measure of the energy in the system while ψ denotes the localization of the energy. For $\psi = \pi/2$ the energy is localized to the LO, while for $\psi = -\pi/2$ it is localized to the nonlinear attachment. Further differentiating r and ψ with respect to time

$$\dot{r} = \frac{a_1\dot{a}_1 + \epsilon a_2\dot{a}_2}{r}, \quad \dot{\psi} = \frac{2\sqrt{\epsilon}}{r^2}(\dot{a_1}a_2 - a_1\dot{a_2}) \tag{5.21}$$

[3]Note that the method of averaging is applied here *ad hoc* as this assumption cannot be proved a priori

yields the slow flow equations of motion in terms of r, ψ and ϕ as follows

$$\begin{cases} \dot{r} = 0 \\ \dot{\psi} = -\frac{\alpha r^2}{2\sqrt{\epsilon}\omega_0^3}[(1+\epsilon) - (1-\epsilon)\sin\psi - 2\sqrt{\epsilon}\cos\psi\cos\phi]\sin\phi \\ \dot{\phi} = \frac{\omega_0}{2} - \frac{\alpha r^2}{4\epsilon\omega_0^3}[(1+\epsilon) - (1-\epsilon)\sin\psi - 2\sqrt{\epsilon}\cos\psi\cos\phi] \\ \qquad\qquad \times[(1-\epsilon) - 2\sqrt{\epsilon}\frac{\sin\psi\cos\phi}{\cos\psi}]. \end{cases} \tag{5.22}$$

Figures 5.6, 5.7 and 5.8 compare the response $x_{\rm na}$ of the nonlinear attachment given by (5.22) to that of the exact system given by (5.8) for different values of ϵ, ω_0 and r while keeping $\alpha = 1$. All figures correspond to impulsive orbits (energy initially completely localized to the LO, i.e. $\psi = \pi/2$ or $\dot{x}_{\rm na}(0) = x_{\rm na}(0) = 0$). Apparently, an acceptable approximation is only obtained for a narrow interval of r. For initial r outside this interval, the approximation is no longer acceptable. The most important phenomena however, like the critical energy threshold that we are interested in, live within this interval and can be revealed by performing a bifurcation analysis on the averaged system as shown in the next section.

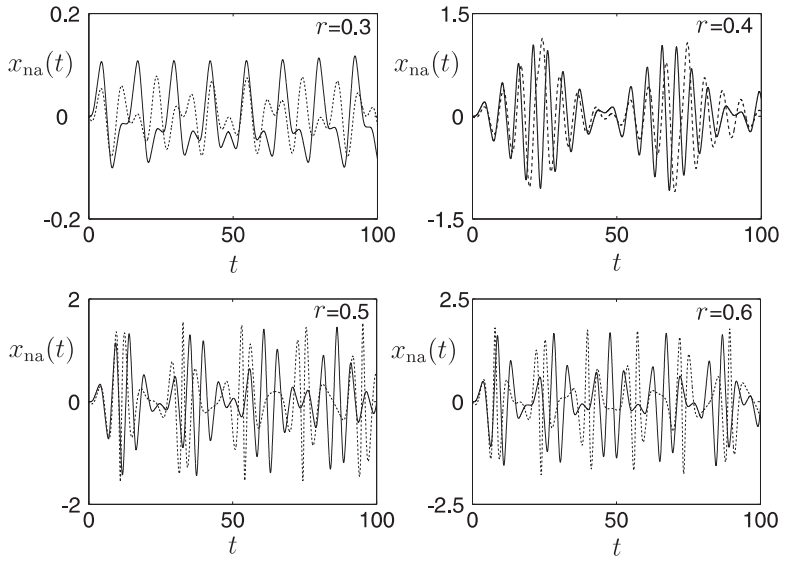

Figure 5.6: Averaged (− − −) vs exact (——) response x_{na} of the nonlinear attachment for $\epsilon = 0.1$, $\omega_0 = 1$ and $r = 0.3$, $r = 0.4$, $r = 0.5$, $r = 0.6$

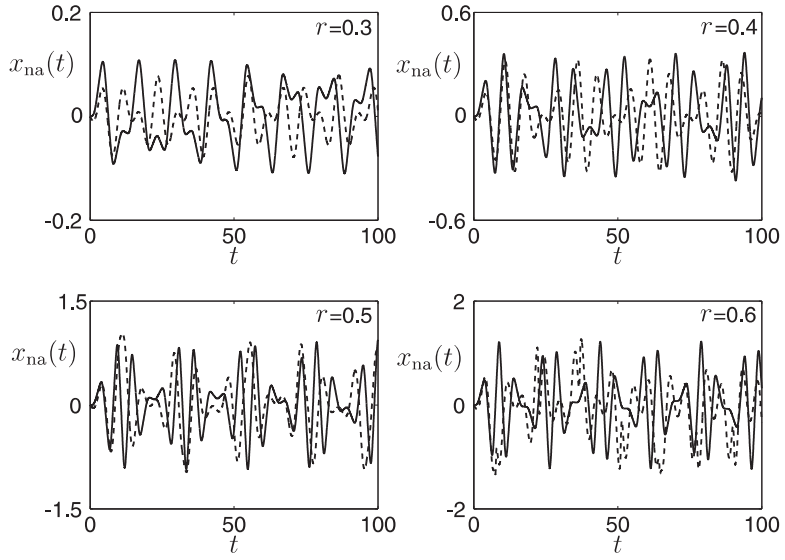

Figure 5.7: Averaged (− − −) vs exact (——) response x_{na} of the nonlinear attachment for $\epsilon = 0.2$, $\omega_0 = 1$ *and* $r = 0.3$, $r = 0.4$, $r = 0.5$, $r = 0.6$

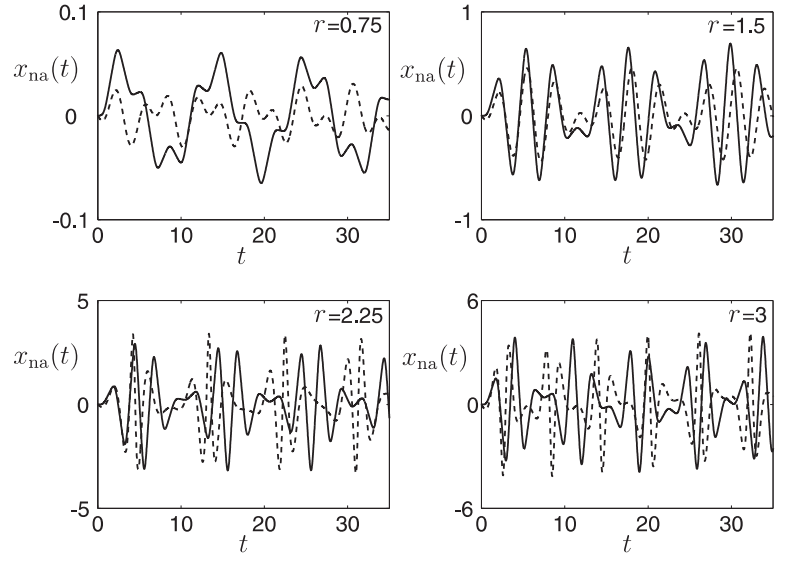

Figure 5.8: Averaged (− − −) vs exact (——) response x_{na} of the nonlinear attachment for $\epsilon = 0.1$, $\omega_0 = 2$ *and* $r = 0.75$, $r = 1.5$, $r = 2.25$, $r = 3$

5.3.2 Bifurcation analysis

The main goal of this section is to investigate the qualitative behavior of system (5.22) as a function of the bifurcation parameter r. The most appropriate way to do this, is by analyzing the corresponding *phase portraits* as a function of r. Figure 5.9 displays the phase portraits for three different values of r, i.e. $r = 0.25$, $r = 0.375$ and $r = 1$ keeping ϵ, ω_0 and α fixed. In these plots, the evolution in time of ψ and ϕ for different initial conditions $\psi(0), \phi(0)$ is shown. The main features of these plots are the fixed points or equilibrium points (small black dots corresponding to $\dot{r} = 0, \dot{\psi} = 0, \dot{\phi} = 0$) and the closed orbits (corresponding to periodic solutions). Their variation (number and qualitative nature) with respect to r is denoted as a *bifurcation* and is crucial in the understanding of the dynamics of a nonlinear system. The most remarkable variation is visible for $r = 0.375$ where two extra fixed points cause a type of trajectories not present in the phase portraits of $r = 0.25$ and $r = 1$. This variation lies at the basis of the threshold phenomenon and is clarified in the subsequent analysis of the fixed points and the closed orbits.

Remark Instead of representing the phase portraits in a Cartesian coordinate system, the spherical coordinates ψ and ϕ are projected onto the unit disk for different values of r such that a clearer picture is obtained. In this projection displayed in Fig. 5.10, $\psi = \pi/2$ (or energy localized to the LO) corresponds to the center of the unit disk while $\psi = -\pi/2$ (or energy localized to the nonlinear attachment) corresponds to the outer circle of the unit disk.

Fixed points

The equilibrium points of system (5.22) are given by

$$\sin \phi_{eq} = 0 \Rightarrow \phi_{eq} = 0 \text{ or } \phi_{eq} = \pi \tag{5.23}$$

$$\omega_0 \cos \psi_{eq} - \frac{\alpha r^2}{2\epsilon\omega_0^3}(1+\epsilon)^2(1 - \sin(\psi_{eq} + \lambda_{eq}))\cos(\psi_{eq} + \lambda_{eq}) = 0 \tag{5.24}$$

with

$$\tan \lambda_{eq} = \frac{2\sqrt{\epsilon}\cos\phi_{eq}}{1-\epsilon}. \tag{5.25}$$

and are displayed in Fig. 5.11 for $\epsilon = 0.1$, $\omega_0 = 1$ and $\alpha = 1$ as a function of r. Two curves can be distinguished which respectively correspond to in-phase ($\phi = \phi_{eq} = 0$) and out-of-phase ($\phi = \phi_{eq} = \pi$) motion of the LO and the nonlinear attachment[4]. The fixed points corresponding to the phase portraits of Fig. 5.9 are highlighted. For $r = 0.25$ there are two fixed points. As evidenced by Fig. 5.9 these

[4]These plots were obtained with MATCONT [37], a continuation and bifurcation toolbox compatible with Matlab®

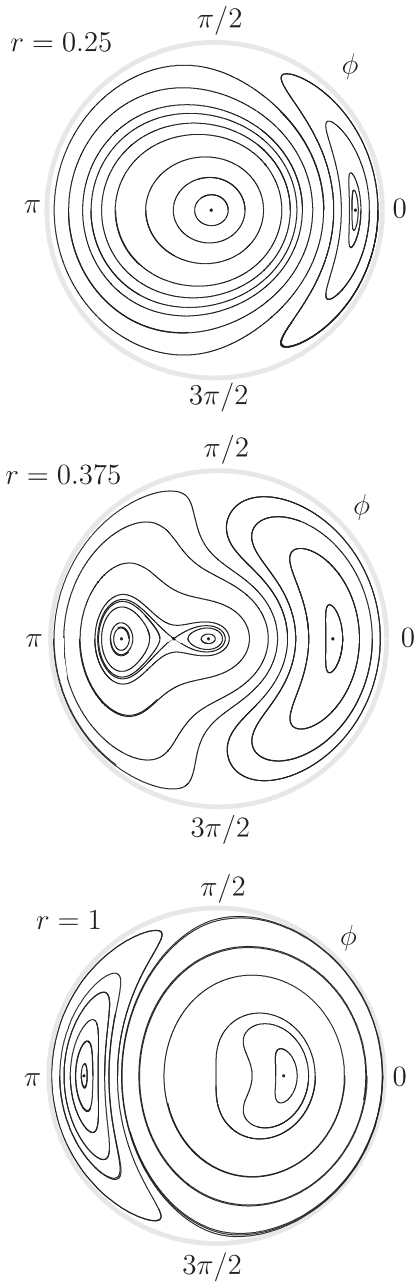

Figure 5.9: Phase portraits system (5.22) for different values of r; $\epsilon = 0.1, \omega_0 = 1, \alpha = 1$

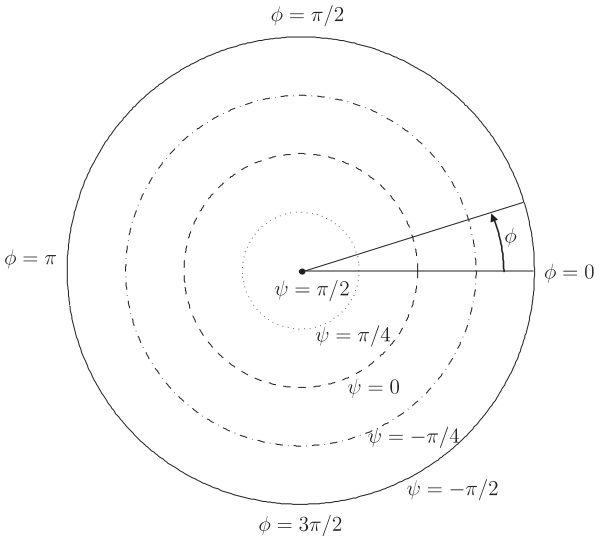

Figure 5.10: Projection of ψ and ϕ onto the unit disk

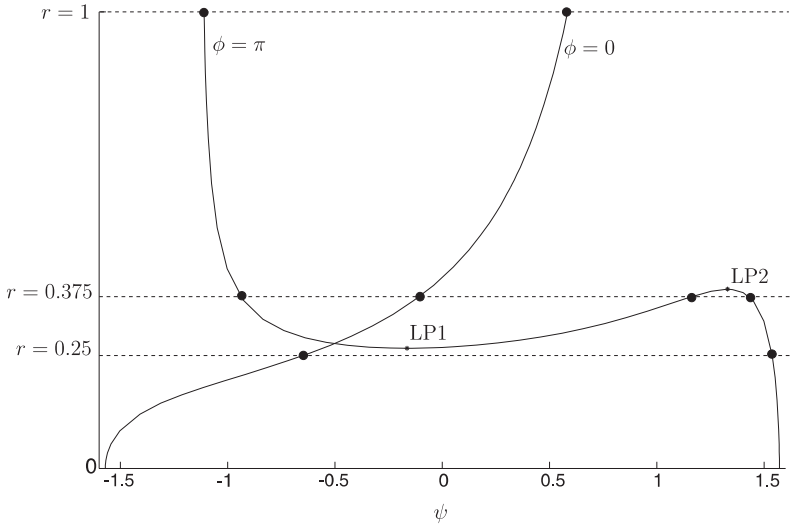

Figure 5.11: S11- and S11+ curve for $\epsilon = 0.1$ and $\omega_0 = 1$

are both nonlinear centers. If r is further increased a saddle-node bifurcation occurs in the $\phi = \pi$-curve (denoted by LP1 in Fig. 5.11) creating two extra fixed points, one nonlinear center and one saddle as shown in Fig. 5.9 for $r = 0.375$. Increasing r even further, a second saddle-node bifurcation in the $\phi = \pi$-curve (denoted by LP2 in Fig. 5.11) destroys two fixed points and only two nonlinear centers remain as evidenced by Fig. 5.9 for $r = 1$. Now that the qualitative nature of the fixed points is clarified, we can turn to the analysis of the closed orbits.

Closed orbits

Of all the orbits displayed in Fig. 5.9, the most important one regarding the existence of an energy threshold is a homoclinic orbit [5]. This homoclinic orbit is clearly visible in Fig. 5.9 ($r = 0.375$) where it starts and ends at the saddle. It is the only orbit of Fig. 5.9 that is not a periodic solution because the saddle is reached in an infinite time. The existence of the homoclinic orbit depends on the existence of the saddle and is therefore restricted to the small interval of r values in between the two saddle-node bifurcations denoted by LP1 and LP2 in Fig. 5.11.

[5] A homoclinic orbit is defined as an orbit that starts and ends at the same fixed point

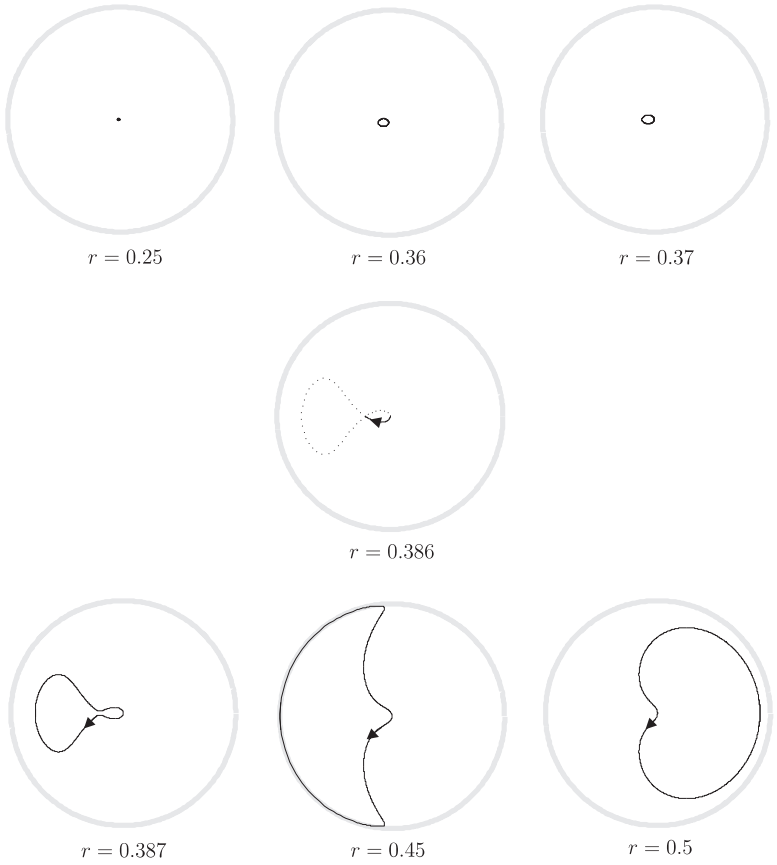

Figure 5.12: Impulsive orbits (——) as a function of r and homoclinic orbit ($\cdots$)

5.3.3 Impulsive orbits

The existence of an energy threshold can now be explained by means of Fig. 5.12 where a special type of orbit, namely an impulsive orbit (energy initially localized to the LO), is displayed as a function of r. All orbits start at the origin of the unit disk[6] and continue in the direction of the arrow. The energy threshold occurs when the impulsive orbit becomes coincident with the homoclinic orbit displayed in the middle plot ($r = 0.386$). At this point the impulsive orbit's period becomes infinite. It starts at the center of the disk and reaches the saddle for $t \to \infty$. For r slightly larger than $r = 0.386$ however, the impulsive orbit is no longer coincident with the homoclinic connection. Besides a finite period, this causes the orbit to experience

[6] As explained in Section 5.4.4 the energy threshold phenomenon can also be experienced in nearly impulsive orbits.

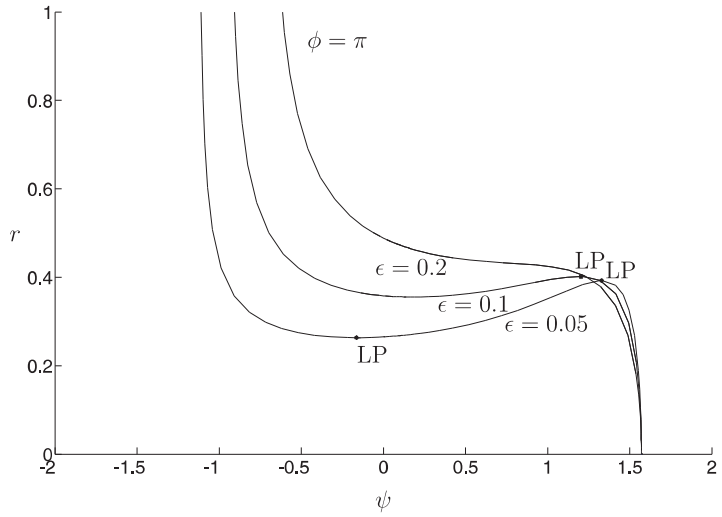

Figure 5.13: S11- curve for different ϵ with $\omega = 1$

large excursions in phase space (Fig. 5.12, lower plots) explaining the jump in amplitude for increasing values of the initial energy (Fig. 5.3).

For larger ϵ (e.g. $\epsilon = 0.2$) no energy threshold is present as no homoclinic connection exists. Indeed, Fig. 5.13 displays the $\phi = \pi$-curve showing that no saddle-node bifurcations occur for $\epsilon = 0.2$ preventing the creation of a homoclinic orbit. The influence of ω_0 is displayed in Figure 5.14 showing that the saddle-node bifurcations (and consequently also the energy threshold) occur for larger r as ω_0 increases. Notice that this corresponds to Fig. 5.8 where a good approximation of the averaged equations is achieved for larger r as ω_0 increases.

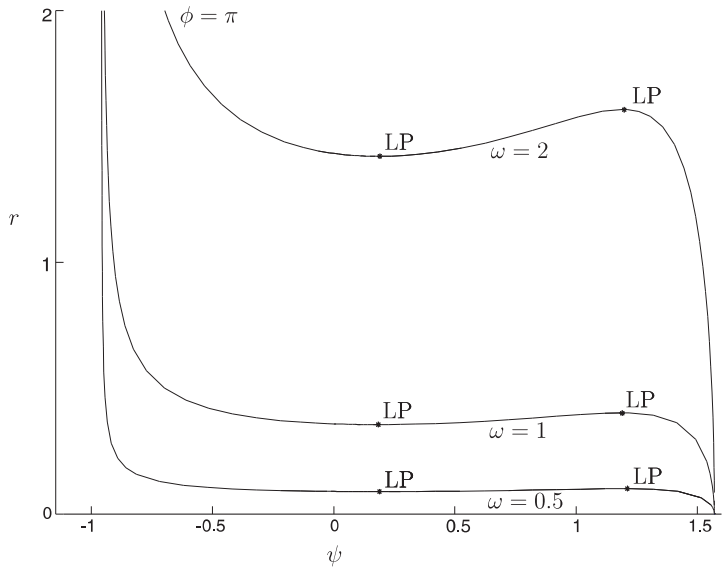

Figure 5.14: S11- curve for different ω with $\epsilon = 0.1$

5.4 Approximate analytical study of the energy thresholds: approach II

The averaging procedure of approach I revealed that the energy threshold occurs when an impulsive orbit becomes coincident with a homoclinic connection. The qualitative effect of ϵ and ω_0 on the threshold value can be determined from Figures 5.13 and 5.14. However, when quantitative measures are required, the entire analysis has to be repeated whenever a parameter (ϵ, α, ω_0) is changing. In approach II a different approximation is applied which results in an analytical formula for the energy threshold as a function of ϵ, α and ω_0. The main advantage is that one single bifurcation analysis is covering every single combination of parameters. Moreover, as will be shown in Section 5.6, the same approach can be used for noncubic absorbers, nonlinear main systems and even harmonically forced linear systems.

For convenience, system (5.8) is repeated here

$$\begin{cases} \ddot{x} + \omega_0^2 x + \frac{4}{3}\epsilon\alpha(x - x_{\text{na}})^3 = 0 \\ \ddot{x}_{\text{na}} + \frac{4}{3}\alpha(x_{\text{na}} - x)^3 = 0. \end{cases}$$

with initial conditions $\dot{x}(0), x(0), \dot{x}_{na}(0), x_{\text{na}}(0)$. Numerical simulations confirm the validity of approximating the response of the main system by that of the main system without absorber , i.e. $x(t) \approx x(0)\cos(\omega_0 t) + \frac{\dot{x}(0)}{\omega_0}\sin\omega_0 t$. Therefore, the

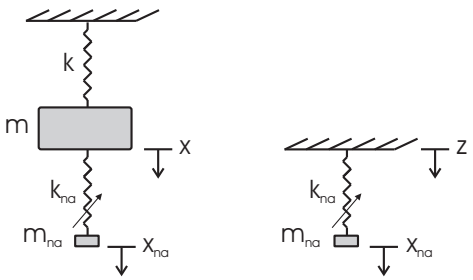

Figure 5.15: Main system replaced with sinusoidally moving ground z

main system can be regarded as a sinusoidally moving ground z as shown in Fig. 5.15. The equation of motion of this simplified system becomes

$$\ddot{x}_{\text{na}} + \frac{4}{3}\alpha(x_{\text{na}} - z)^3 = 0 \tag{5.26}$$

with $z = x(0)\cos(\omega_0 t) + \frac{\dot{x}(0)}{\omega}\sin\omega t$. Introducing the relative displacement $x_{\text{r}} = x_{\text{na}} - z$ changes Eq. (5.26) into

$$\ddot{x}_{\text{r}} + \frac{4}{3}\alpha x_{\text{r}}^3 \triangleq X\sin(\omega_0 t + \phi) \tag{5.27}$$

with

$$X = \sqrt{\omega_0^4 x(0)^2 + \omega_0^2 \dot{x}(0)^2} \tag{5.28}$$

$$\phi = \arctan\left(\frac{\omega_0 x(0)}{\dot{x}(0)}\right) + k\pi; \quad k \in \mathbb{Z} \tag{5.29}$$

and initial conditions $x_{\text{r}}(0) = x_{\text{na}}(0) - x(0), \dot{x}_{\text{r}}(0) = \dot{x}_{na}(0) - \dot{x}(0)$. Equation (5.27) shows that the original two-degree-of-freedom system in free response is approximated by a harmonically excited single-degree-of-freedom system. Again, for this second approximation method, the response of the nonlinear attachment obtained with Eq. (5.27) is compared to the exact response given by (5.8). The result is shown in Figures 5.16-5.18 for different values of ϵ and ω_0 while keeping $\alpha = 1$. For each combination of ϵ, ω_0 and $\alpha = 1$, four different values of $\dot{x}(0)$ are chosen. The approximation works quite well for larger $\dot{x}(0)$ although the threshold seems to be attained for smaller $\dot{x}(0)$ compared to that of the exact response. A large discrepancy occurs in Fig. 5.17 ($\epsilon = 0.2, \omega_0 = 1$) revealing the limits of this approximation method as it is only valid for sufficiently small ϵ.

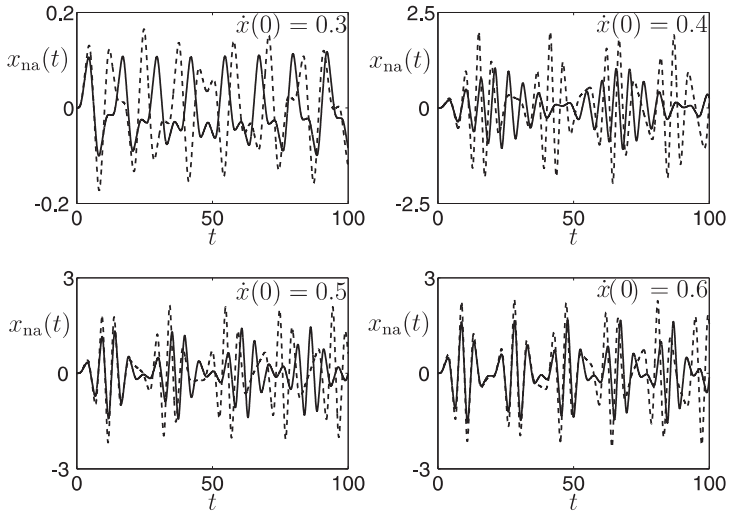

Figure 5.16: Approximate (– – –) vs exact response (——) of the nonlinear attachment for $\epsilon = 0.1$, $\omega_0 = 1$ *and* $\dot{x}(0) = 0.3$, $\dot{x}(0) = 0.4$, $\dot{x}(0) = 0.5$, $\dot{x}(0) = 0.6$

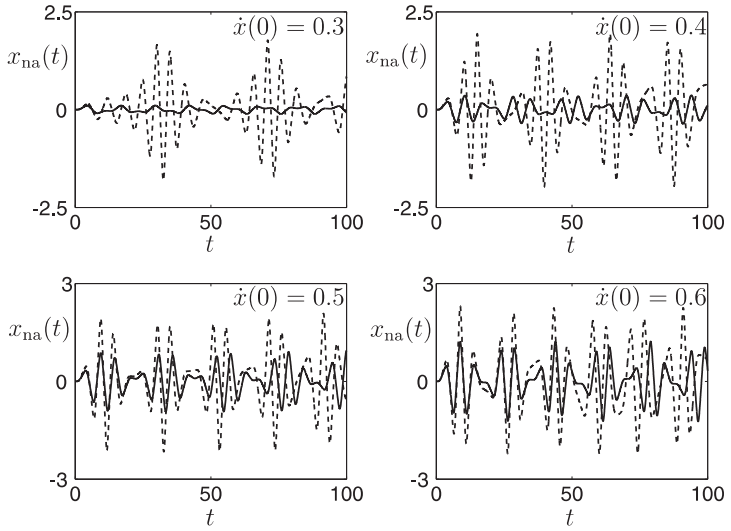

Figure 5.17: Approximate (– – –) vs exact response (——) of the nonlinear attachment for $\epsilon = 0.2$, $\omega_0 = 1$ *and* $\dot{x}(0) = 0.3$, $\dot{x}(0) = 0.4$, $\dot{x}(0) = 0.5$, $\dot{x}(0) = 0.6$

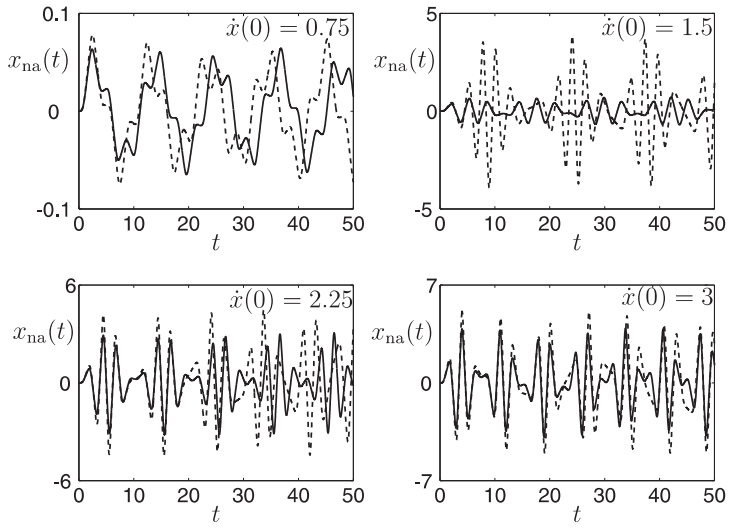

Figure 5.18: Approximate (− − −) vs exact response (——) of the nonlinear attachment for $\epsilon = 0.1$, $\omega_0 = 2$ *and* $\dot{x}(0) = 0.75$, $\dot{x}(0) = 1.5$, $\dot{x}(0) = 2.25$*),* $\dot{x}(0) = 3$

5.4.1 Dimensionless system

Analyzing Eq. (5.27) is not straightforward because it contains 4 different parameters, namely $\alpha, \omega_0, x(0)$ and $\dot{x}(0)$. Expressing Eq. (5.27) in dimensionless form severely facilitates the analysis as these parameters can be joined together into only one dimensionless group. First a dimensionless time $\tau = \omega_0 t$ is introduced. In this new time τ, first and second derivatives of x_{r} become

$$\begin{cases} \dot{x}_{\mathrm{r}} = \frac{dx_{\mathrm{r}}}{dt} = \frac{dx_{\mathrm{r}}}{d\tau}\frac{d\tau}{dt} = \frac{dx_{\mathrm{r}}}{d\tau}\omega_0 \\ \ddot{x}_{\mathrm{r}} = \frac{d}{dt}\frac{dx_{\mathrm{r}}}{d\tau}\omega_0 = \frac{d^2x_{\mathrm{r}}}{d\tau^2}\omega_0^2 \end{cases} \tag{5.30}$$

changing Eq. (5.27) into:

$$\omega_0^2 \frac{d^2x_{\mathrm{r}}}{d\tau^2} + \frac{4}{3}\alpha x_{\mathrm{r}}^3 = X\sin(\tau + \phi) \tag{5.31}$$

with initial conditions $x_{\mathrm{r}}(0) = x_{\mathrm{na}}(0) - x(0)$, $\frac{dx_{\mathrm{r}}}{d\tau}(0) = \frac{\dot{x}_{na}(0) - \dot{x}(0)}{\omega_0}$. Secondly, a dimensionless coordinate x_{d} is introduced:

$$x_{\mathrm{d}} = \frac{x_{\mathrm{r}}\omega_0^2}{X}. \tag{5.32}$$

Finally, substituting Eq. (5.32) into Eq. (5.31), the dimensionless form of Eq. (5.27) becomes

$$\frac{d^2x_{\mathrm{d}}}{d\tau^2} + \gamma x_{\mathrm{d}}^3 = \sin(\tau + \phi) \tag{5.33}$$

with initial conditions

$$\begin{cases} x_d(0) & = \frac{(x_{\text{na}}(0)-x(0))\omega_0^2}{\sqrt{\omega_0^4 x(0)^2+\omega_0^2\dot{x}(0)^2}} \\ \frac{dx_d}{d\tau}(0) & = \frac{(\dot{x}_{na}(0)-\dot{x}(0))\omega_0}{\sqrt{\omega_0^4 x(0)^2+\omega_0^2\dot{x}(0)^2}}. \end{cases} \tag{5.34}$$

Note that $\alpha, \omega_0, x(0)$ and $\dot{x}(0)$ are joined into one dimensionless parameter $\gamma > 0$

$$\gamma = \frac{4}{3}\alpha\frac{X^2}{\omega_0^6} \tag{5.35}$$

$$= \frac{4}{3}\alpha\frac{(x(0)^2\omega_0^2 + \dot{x}(0)^2)}{\omega_0^4}. \tag{5.36}$$

5.4.2 Averaged equations

Equation (5.33) involves a nonlinear oscillator undergoing strong harmonic forcing and is far from straightforward to analyze. Again, as in Section 5.3, we assume that the response x_d can be written as a sine function (fast time scale) with a slowly varying amplitude (slow time scale) such that (complexification) averaging over the fast time scale can be performed. By introducing a complex function ρ

$$\rho(\tau)e^{i\tau} = \frac{dx_d(\tau)}{d\tau} + ix_d(\tau) \tag{5.37}$$

x_d, $\frac{dx_d}{d\tau}$ and $\frac{d^2x_d}{d\tau^2}$ become (dependence on τ is omitted from here on)

$$\begin{cases} x_d & = \frac{\rho e^{i\tau}-\rho^* e^{-i\tau}}{2i} \\ \frac{dx_d}{d\tau} & = \frac{\rho e^{i\tau}+\rho^* e^{-i\tau}}{2} \\ \frac{d^2x_d}{d\tau^2} & = \frac{d\rho}{d\tau}e^{i\tau} + \rho i e^{i\tau} - i(\frac{dx_d}{d\tau}) \end{cases} \tag{5.38}$$

where ρ^* denotes the complex conjugate of ρ. Substitution of (5.38) into Eq. (5.33) yields

$$\frac{d\rho}{d\tau}e^{i\tau} + \frac{i}{2}\rho e^{i\tau} - \frac{i}{2}\rho^* e^{-i\tau} + \frac{i\gamma}{8}\left[\rho^3 e^{i3\tau} - 3\rho^2\rho^* e^{i\tau} + 3\rho{\rho^*}^2 e^{-i\tau} - {\rho^*}^3 e^{-3i\tau}\right] = \frac{e^{i(\tau+\phi)} - e^{-i(\tau+\phi)}}{2i}. \tag{5.39}$$

By assuming that ρ is slowly varying compared to the fast time scale τ we can average Eq. (5.39) over this fast time scale and obtain

$$\frac{d\rho}{d\tau} + \frac{i}{2}\rho - \frac{3\gamma i}{8}|\rho|^2\rho = \frac{1}{2i}e^{i\phi}; \quad \rho(0) = \frac{dx_d}{d\tau}(0) + ix_d(0). \tag{5.40}$$

Finally, by writing $\rho = \rho_{re} + i\rho_{im}$, Eq. (5.40) can be divided into its real and imaginary part

$$\begin{cases} \frac{d\rho_{re}}{d\tau} & = \frac{\rho_{im}}{2} - \frac{3\gamma}{8}({\rho_{re}}^2 + {\rho_{im}}^2)\rho_{im} + \frac{\sin\phi}{2} \\ \frac{d\rho_{im}}{d\tau} & = -\frac{\rho_{re}}{2} + \frac{3\gamma}{8}({\rho_{re}}^2 + {\rho_{im}}^2)\rho_{re} - \frac{\cos\phi}{2} \end{cases} \tag{5.41}$$

with initial conditions

$$\begin{cases} \rho_{re}(0) & = \frac{dx_d}{d\tau}(0) \\ \rho_{im}(0) & = x_d(0). \end{cases} \tag{5.42}$$

Remark A solution $(\tau \mapsto \rho_{re}(\tau), \tau \mapsto \rho_{im}(\tau))$ of the averaged Eqs. in (5.41) corresponds to a solution $t \mapsto x_r(t)$ of Eq. (5.27) as follows

$$x_r(t) = \frac{X}{\omega_0^2}\sqrt{{\rho_{re}}^2(\omega_0 t) + {\rho_{im}}^2(\omega_0 t)}\,\sin(\omega_0 t + \phi_d(\omega_0 t)) \tag{5.43}$$

$$\tan(\phi_d(\omega_0 t)) = \frac{\rho_{im}(\omega_0 t)}{\rho_{re}(\omega_0 t)}. \tag{5.44}$$

Before we head into the bifurcation analysis, two important properties of system (5.41) are presented: rotational symmetry and reversibility.

Rotational symmetry

Consider the rotation matrix R

$$R(\phi) = \begin{bmatrix} \cos(\phi) & -\sin(\phi) \\ \sin(\phi) & \cos(\phi) \end{bmatrix} \tag{5.45}$$

which rotates a vector $[\rho'_{re}\ \rho'_{im}]$ counterclockwise by an angle ϕ. The new vector $[\rho_{re}\ \rho_{im}]$ becomes

$$\begin{bmatrix} \rho_{re} \\ \rho_{im} \end{bmatrix} = \begin{bmatrix} \cos(\phi) & -\sin(\phi) \\ \sin(\phi) & \cos(\phi) \end{bmatrix} \begin{bmatrix} \rho'_{re} \\ \rho'_{im} \end{bmatrix} \tag{5.46}$$

By substituting Eq. (5.46) into (5.41) one obtains

$$\begin{cases} \frac{d\rho'_{re}}{d\tau}\cos(\phi) - \frac{d\rho'_{im}}{d\tau}\sin(\phi) = \frac{\rho'_{re}\sin(\phi) + \rho'_{im}\cos(\phi)}{2} \\ -\frac{3}{8}\gamma({\rho_{re}}^2 + {\rho_{im}}^2)(\rho'_{re}\sin(\phi) + \rho'_{im}\cos(\phi)) + \frac{\sin(\phi)}{2} \\ \frac{d\rho'_{re}}{d\tau}\sin(\phi) + \frac{d\rho'_{im}}{d\tau}\cos(\phi) = \frac{-\rho'_{re}\cos(\phi) + \rho'_{im}\sin(\phi)}{2} \\ +\frac{3}{8}\gamma({\rho_{re}}^2 + {\rho_{im}}^2)(\rho'_{re}\cos(\phi) - \rho'_{im}\sin(\phi)) - \frac{\cos(\phi)}{2}. \end{cases} \tag{5.47}$$

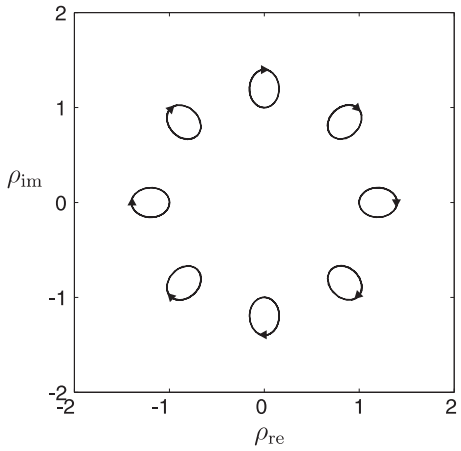

Figure 5.19: Phase portrait of system (5.41) for $\phi = k\pi/4,\ k = 1, ..., 8$ and initial conditions $\rho_{re}(0) = \cos(\phi)$ and $\rho_{im}(0) = \sin(\phi)$

Solving for $\frac{d\rho'_{re}}{d\tau}$ and $\frac{d\rho'_{im}}{d\tau}$ yields

$$\begin{cases} \frac{d\rho'_{re}}{d\tau} & = \frac{\rho'_{im}}{2} - \frac{3\gamma}{8}({\rho'_{re}}^2 + {\rho'_{im}}^2)\rho'_{im} \\ \frac{d\rho'_{im}}{d\tau} & = -\frac{\rho'_{re}}{2} + \frac{3\gamma}{8}({\rho'_{re}}^2 + {\rho'_{im}}^2)\rho'_{re} + \frac{1}{2} \end{cases} \tag{5.48}$$

which is equivalent to the original system (5.41) with $\phi = 0$ and initial conditions $\rho'_{re}(0)$ and $\rho'_{im}(0)$. As a result, the phase portraits of (5.41) in the (ρ_{re}, ρ_{im}) phase plane are exactly the same as those of (5.48) rotated counterclockwise by angle ϕ. This is exemplified in Fig. 5.19 for $\phi = k\pi/4,\ k = 1, ..., 8$ with initial conditions $\rho_{re}(0) = \cos(\phi)$ and $\rho_{im}(0) = \sin(\phi)$. In other words, the qualitative behavior of (5.41) does not change as a function of ϕ which leaves γ as the only bifurcation parameter. Without loss of generalization only $\phi = 0$ will be considered from hereon.

Reversibility

We prove that system (5.48) is reversible, i.e. it features a time-reversal symmetry [38]. Physically this means that the dynamics are equivalent for forward and backward running times. More generally :

Consider any mapping $R : \mathbb{R}^n \mapsto \mathbb{R}^n$ satisfying $R^2(x) = x,\ x \in \mathbb{R}^n$. Then the system $\dot{x} = f(x)$ is reversible if it is invariant under the change of variables $\tau \to -\tau$ and $x \to R(x)$.

Applied to (5.48), consider a mapping R that defines a reflection about the x-axis

$$R = \begin{bmatrix} 1 & 0 \\ 0 & -1 \end{bmatrix} \tag{5.49}$$

which satisfies $R^2(x) = x$ because $R^2 = I$. The change of variables $\tau \rightarrow -\tau$ and $(\rho'_{re}, \rho'_{im}) \rightarrow (\rho'_{re}, -\rho'_{im})$ leaves (5.48) unaltered meeting in this way the requirements for reversibility. The reversibility property proves to be very useful throughout the entire bifurcation analysis. For instance, regarding fixed points, the linearization process is also valid for centers. This means that a linear center is also a nonlinear center which is generally not the case. Another advantage of reversible systems is that one can easily prove the existence of periodic solutions, i.e. closed orbits in the phase plane.

5.4.3 Bifurcation analysis

We study the qualitative behavior of system (5.41) (with $\phi = 0$ due to rotational symmetry) as a function of γ, which serves as the bifurcation parameter. For different initial conditions, the solutions can be visualized as trajectories moving on the (ρ_{re}, ρ_{im}) phase plane. As an example, the phase portraits for $\gamma = 0.15$ and $\gamma = 0.198$ are shown in Fig. 5.20. Compared to $\gamma = 0.198$, two extra fixed points (small black dots) can be noticed for $\gamma = 0.15$. The resulting closed orbits near these fixed points are remarkably different for both values of γ. These observations lie at the heart of the existence of a threshold value and are explained in detail in what follows.

Fixed points and linearization

The fixed points can be obtained by setting $\frac{d\rho_{re}}{d\tau} = 0$ and $\frac{d\rho_{im}}{d\tau} = 0$ in (5.41) and solving for ρ_{re} and ρ_{im}. The equilibrium points $(\rho_{re})_{eq}$ and $(\rho_{im})_{eq}$ are found to be given by

$$\frac{3}{8}\gamma(\rho_{re})_{eq}^3 - \frac{(\rho_{re})_{eq}}{2} - \frac{1}{2} = 0 \tag{5.50}$$

$$(\rho_{im})_{eq} = 0. \tag{5.51}$$

In Fig. 5.21 the fixed points $(\rho_{re})_{eq}$ (obtained with MATCONT [37]) are displayed as a function of γ. The fixed points corresponding to the phase portraits of Fig. 5.20 ($\gamma = 0.15$ and $\gamma = 0.198$) are highlighted. Two curves can be distinguished separated by an interval $-1 < (\rho_{re})_{eq} < 0$ where no equilibrium points exist. Similar to Fig. 5.11 the fixed points correspond to either in-phase or out-of-phase motion. Indeed, according to Eqs. (5.37,5.38) the absorber's response x_{na}

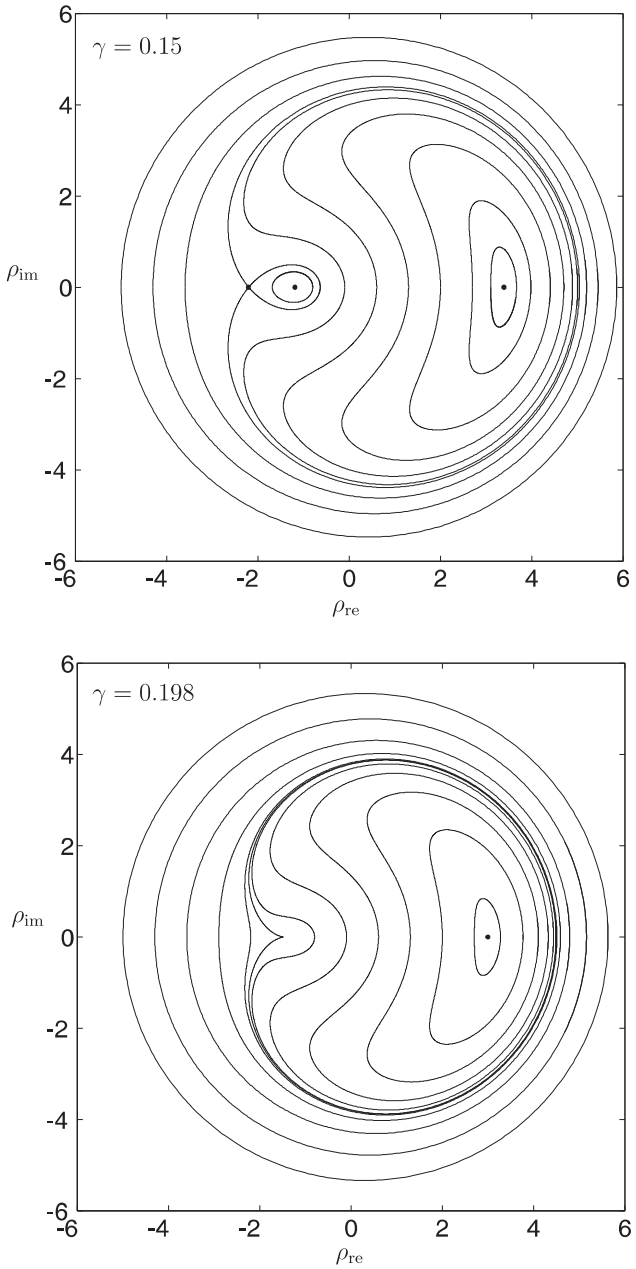

Figure 5.20: Phase portraits of system (5.41) for $\phi = 0$, Upper: $\gamma = 0.15$; Lower: $\gamma = 0.198$

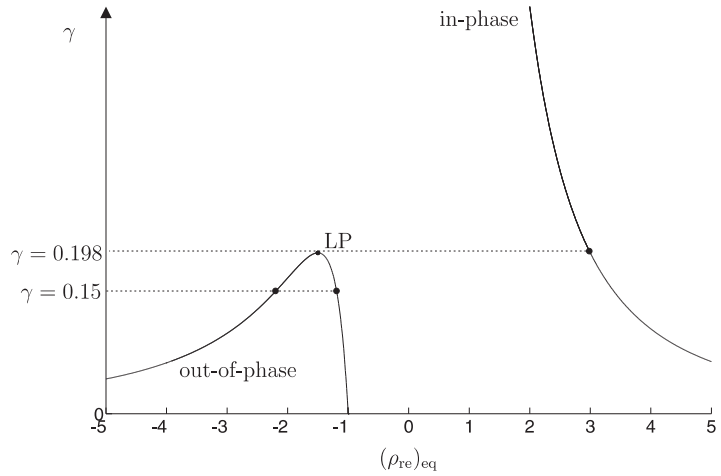

Figure 5.21: Equilibrium points $(\rho_{re})_{eq}$ as a function of γ

(for $\phi = 0$ and thus $x(0) = 0$) in the fixed points becomes

$$x_{\text{na}} = \frac{\dot{x}(0)^2}{\omega_0}(1 + (\rho_{re})_{eq}) \sin(\omega_0 t) \tag{5.52}$$

whereas the response of the LO is given by

$$x = \frac{\dot{x}(0)^2}{\omega_0} \sin(\omega_0 t). \tag{5.53}$$

Consequently, $(\rho_{re})_{eq} < -1$ corresponds to out-of-phase motion while for $(\rho_{re})_{eq} > -1$ in-phase motion occurs. For small γ there are three fixed points (two corresponding to out-of-phase and one to in-phase motion). As γ increases, a saddle-node bifurcation at $\gamma \approx 0.198$ (denoted by LP in Fig. 5.21) destroys the fixed points corresponding to the out-of-phase motion and only one fixed point (corresponding to in-phase motion) remains for $\gamma > 0.198$. This makes sense as a large γ (e.g. large $\dot{x}(0)$) corresponds to a very stiff linear spring forcing the in-phase motion.

The nature of the fixed points $(\rho_{re})_{eq}$ and $(\rho_{im})_{eq}$, although apparent from Fig. 5.20, can be explicitly determined by linearizing

$$\begin{cases} \frac{d\rho_{re}}{d\tau} & = f(\rho_{re}, \rho_{im}) = \frac{\rho_{im}}{2} - \frac{3\gamma}{8}({\rho_{re}}^2 + {\rho_{im}}^2)\rho_{im} \\ \frac{d\rho_{im}}{d\tau} & = g(\rho_{re}, \rho_{im}) = -\frac{\rho_{re}}{2} + \frac{3\gamma}{8}({\rho_{re}}^2 + {\rho_{im}}^2)\rho_{re} - \frac{1}{2}. \end{cases} \tag{5.54}$$

The Jacobian matrix A_J at the fixed points becomes

$$A_J = \begin{bmatrix} \frac{df}{d\rho_{re}} & \frac{df}{d\rho_{im}} \\ \frac{dg}{d\rho_{re}} & \frac{dg}{d\rho_{im}} \end{bmatrix}_{(\rho_{re})_{eq},(\rho_{im})_{eq}} = \begin{bmatrix} 0 & \frac{1}{2} - \frac{3}{8}\gamma(\rho_{re})_{eq} \\ -\frac{1}{2} + \frac{3}{8}\gamma(\rho_{re})_{eq} & 0 \end{bmatrix}. \tag{5.55}$$

For $\gamma < 0.198$ there are three fixed points (Fig. 5.21). The corresponding eigenvalues of A show that these are two linear centers and one saddle. Because the system is reversible the linear centers are also nonlinear centers [38]. For $\gamma \geq 0.198$ only one nonlinear center remains. These findings agree with the numerical simulations of Fig. 5.20 where for $\gamma = 0.15$ clearly one saddle and two nonlinear centers exist while for $\gamma = 0.198$ only one nonlinear center remains.

Remark When comparing Figs. 5.11 and 5.21 a difference can be noticed in the number of fixed points. While Fig. 5.21 displays maximum three fixed points, there are up to four fixed points in Fig. 5.11. Furthermore, for large r two fixed points exist (one for $\phi = \pi$ and one for $\phi = 0$) while for large γ there is only one fixed point. This difference is caused by the initial assumptions of both approximation methods. While the motion of the LO is restricted to $x(t) = X\sin(\omega_0 t + \phi)$ in Method II, a more general motion is possible in Method I where $x(t) = a_1(t)\sin(\omega_0 t + \theta_1(t))$. Consequently, the assumption in Method II prevents the energy from being localized to the nonlinear attachment. As a result, fixed points corresponding to ψ_{eq} close to $-\pi/2$ in Fig. 5.11 are not present in Fig. 5.21. The initial energy of the orbits corresponding to these *extra* fixed points is however mainly localized to the nonlinear attachment and therefore less interesting from a practical viewpoint.

Closed orbits

Because the system is reversible, it can be easily shown that all orbits in Fig. 5.20 are closed orbits. Using the same argument the existence of a homoclinic orbit [7] for $\gamma < 0.198$ is also apparent.

5.4.4 Impulsive orbits

We focus on a special type of orbit, namely an impulsive orbit which was also focussed on in Section 5.3. These impulsive orbits are physically important because they correspond to energy initially localized to the LO (for $\phi = 0$ this means $\dot{x}(0) \neq 0, x(0) = x_{\text{na}}(0) = \dot{x}_{\text{na}}(0) = 0$ in (5.8) or $\rho_{re}(0) = -1$ and $\rho_{im}(0) = 0$ in (5.54). These are also the orbits that experience the threshold phenomenon. They are displayed in Fig. 5.22 for different values of γ. The top three plots show impulsive orbits below the energy threshold ($\gamma < \gamma_c$). At the energy threshold ($\gamma = \gamma_c$) the impulsive orbit (solid line) becomes coincident with a homoclinic orbit driving the orbit's period infinite. The dotted line shows a different larger homoclinic orbit starting and ending at the same saddle point. For $\gamma > \gamma_c$ the impulsive orbit runs very close to the small homoclinic orbit (Fig. 5.23, $\gamma = 0.180$). When it approaches the saddle point, the unstable manifold of the larger homoclinic orbit blows it away

[7] A homoclinic orbit is an orbit that starts and ends at the same fixed point

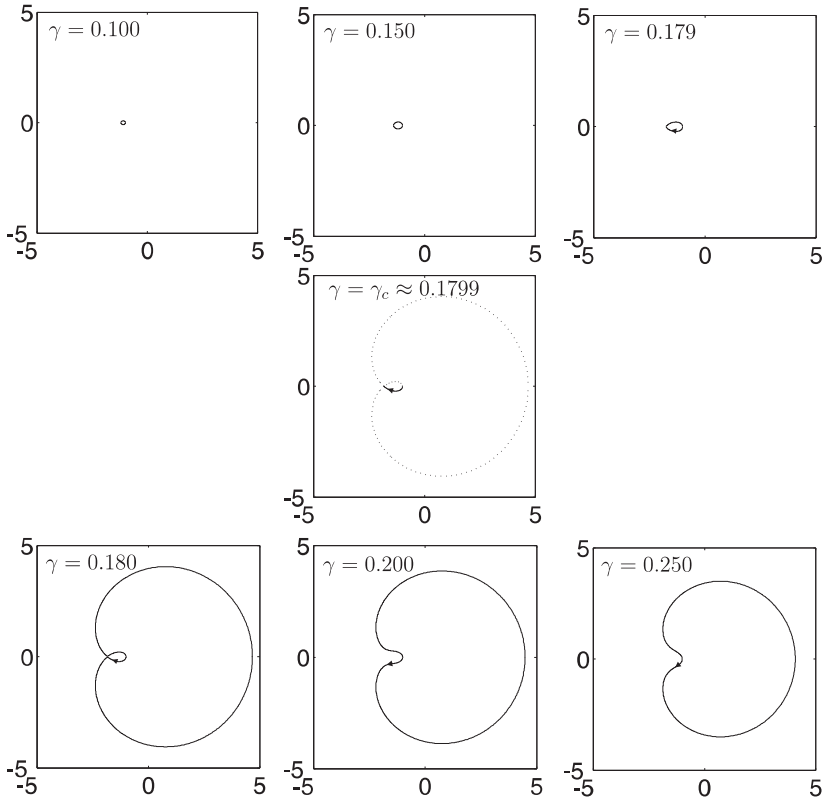

Figure 5.22: Impulsive orbits (——) in the (ρ_{re}, ρ_{im})-plane as a function of γ and homoclinic orbit $(\cdots)$

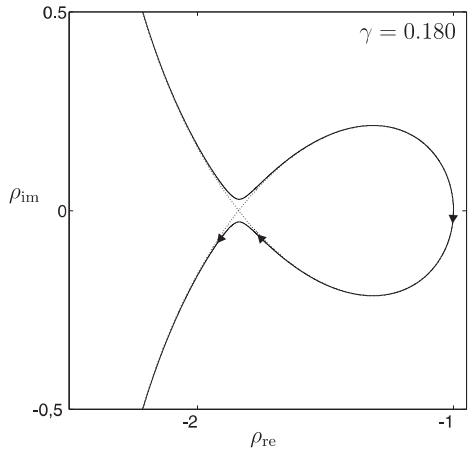

Figure 5.23: Impulsive orbit (——) in the (ρ_{re}, ρ_{im})-plane for $\gamma = 0.180$ and homoclinic orbit $(\cdots)$

towards much larger amplitudes explaining in this way the jump in amplitude occurring at the energy threshold.

Up till now we have only considered the absorber initially at rest. In this case, Eqs. (5.34) and (5.42) show that the trajectories in the (ρ_{re}, ρ_{im}) plane all start at the unit circle (cfr. the rotational symmetry discussed in section 5.4.3)

$$(\rho_{re}(0))^2 + (\rho_{im}(0))^2 = \left(\frac{dx_d}{d\tau}(0)\right)^2 + (x_d(0))^2 \tag{5.56}$$

$$= 1 \tag{5.57}$$

Now, consider the phase portrait for the threshold value of $\gamma \approx 0.18$ as displayed in Fig. 5.24. Trajectories that lie close but within the unit circle still experience large excursions in phase space corresponding to strong absorber movement. On the contrary, trajectories that lie close but outside the unit circle are confined within the homoclinic orbit and correspond to weak absorber movement. Consequently, when the absorber has small nonzero initial conditions, strong absorber movement for $\gamma \approx 0.18$ still occurs when

$$\left(\frac{dx_d}{d\tau}(0)\right)^2 + (x_d(0))^2 < 1 \tag{5.58}$$

or

$$\frac{(x_{\rm na}(0) - x(0))^2\omega_0^4 + (\dot{x}_{na}(0) - \dot{x}(0))^2\omega_0^2}{\omega_0^4 x(0)^2 + \omega_0^2 \dot{x}(0)^2} < 1 \tag{5.59}$$

As a function of $(x(0), \dot{x}(0))$, Eq. (5.59) shows in which region of $(x_{\rm na}(0), \dot{x}_{\rm na}(0))$

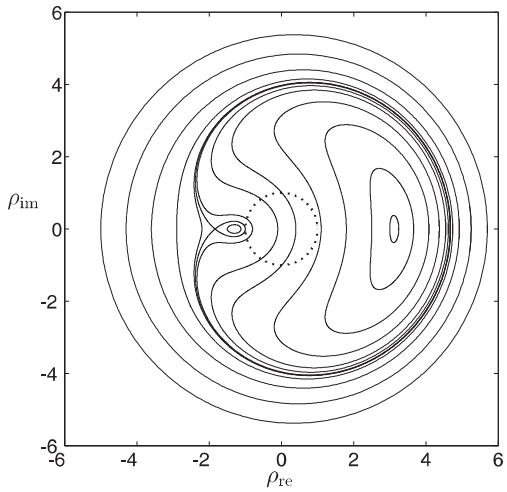

Figure 5.24: Phase portrait of system (5.41) for $\phi = 0$, $\gamma = 0.18$ and the unit circle ($\cdots$)

efficient vibration reduction can be achieved. Values on the boundary of this region can be interpreted as threshold values of $x_{\mathrm{na}}(0)$ and $\dot{x}_{\mathrm{na}}(0)$.

5.5 Discussion

Both approximation methods succeed in capturing the energy threshold phenomenon which is crucial in designing a nonlinear vibration absorber. The averaging procedure in approach I allows a full analysis of the system dynamics even for weakly damped systems. In [33] this is exploited to determine the conditions that lead to an optimal energy transfer from the LO to the nonlinear attachment.

Although the second approach cannot be extended to lightly damped systems, it is of great value because it results in an analytical expression for the energy threshold

$$\gamma = \frac{4}{3}\alpha\frac{(x(0)^2\omega_0^2 + \dot{x}(0)^2)}{\omega_0^4} > \gamma_c \approx 0.18 \tag{5.60}$$

adding insight to the design procedure of nonlinear vibration absorbers.

First of all, the sensitivity in the absorber design towards changes in α, ω_0 and initial energy of the LO becomes apparent. For an impulsively excited LO ($\dot{x}(0) \neq 0$, $x(0) = 0$), it shows that the design is most sensitive to changes in ω_0 (4th order), followed by changes in the initial velocity (2nd order) and changes in k_{na} and m_{na} (1st order).

Secondly, Eq. (5.60) shows that the concept of an energy threshold should be extended to a more general parameter threshold where each parameter (initial energy,

α and ω_0) is characterized by its own threshold value as a function of the other parameter values. In other words, Eq. (5.60) provides the boundaries of a subset of the parameter space that is capable of providing efficient vibration reduction, crucial information in the design procedure of the absorber.

From Eq. (5.60) it is also clear now that the capability of the cubic spring absorber in reducing vibrations at virtually any frequency ω_0 comes with a price. Indeed, for the same nonlinear absorber (fixed $\alpha = 3k_{\text{na}}/4m_{\text{na}}$), a change in ω_0 requires a change in initial conditions $x(0)$ or $\dot{x}(0)$. Hence, it suffers from a strong amplitude dependency. To circumvent this problem, one could think of a main system where ω_0 itself is a function of the initial conditions $x(0)$ or $\dot{x}(0)$. This is exactly what happens in nonlinear primary systems and is besides other advantages further discussed in Section 5.6.

Remark In [39], published very recently, an analytical formula similar to Eq. (5.60) has been derived based on multiple scales expansion [34]. The focus lies on achieving efficient targeted energy transfer from the linear oscillator to a damped nonlinear attachment. As shown by [40], this is accomplished for initial energies that lie just above the saddle-node bifurcation. In the context of Section 5.4, this corresponds to $\gamma > 0.198$ as shown in Fig. 5.21 and results in the exact same formula as that obtained in [39] for zero relative damping.

5.6 Further advantages of Method II

Besides this analytical expression for cubic springs, approach II has other important advantages to offer. Indeed, it is shown that it can be extended to handle noncubic spring characteristics, nonlinear main systems and even harmonically forced linear main systems.

5.6.1 Noncubic spring characteristic

For general spring characteristics the dimensionless system of (5.33) becomes

$$\frac{d^2x_{\text{d}}}{d\tau^2} + \gamma\ \text{sgn}(x_{\text{d}})|x_{\text{d}}|^p = \sin(\tau + \phi) \tag{5.61}$$

with initial conditions

$$x_d(0) = \frac{(x_{\text{na}}(0) - x(0))\omega_0}{\sqrt{\omega_0^4 x(0)^2 + \omega_0^2 \dot{x}(0)^2}} \tag{5.62}$$

$$\frac{dx_d}{d\tau}(0) = \frac{\dot{x}_{na}(0) - \dot{x}(0)}{\sqrt{\omega_0^4 x(0)^2 + \omega_0^2 \dot{x}(0)^2}}. \tag{5.63}$$

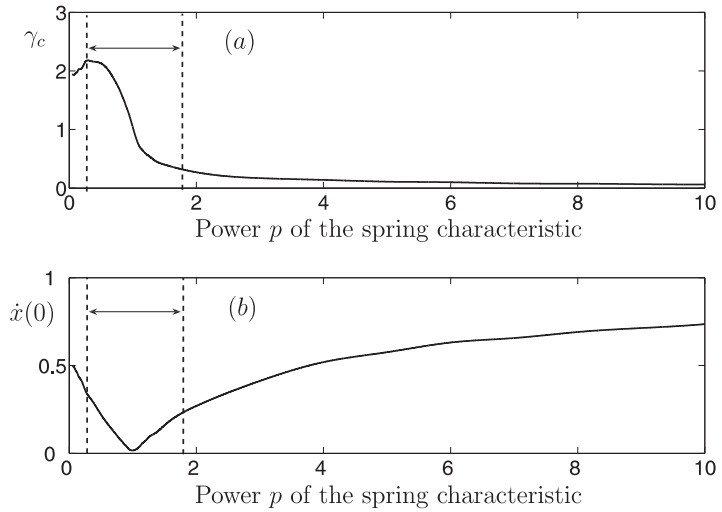

Figure 5.25: (a) γ and (b) initial velocity as a function of the power p of the spring characteristic

Again $\alpha, \omega_0, x(0)$ and $\dot{x}(0)$ are joined into one single dimensionless parameter $\gamma > 0$ which now also depends on p

$$\gamma = \frac{4}{3}\alpha \frac{X^{p-1}}{\omega_0^{2p}} \tag{5.64}$$

$$= \frac{4}{3}\alpha \frac{(x(0)^2\omega_0^2 + \dot{x}(0)^2)^{(p-1)/2}}{\omega_0^{p+1}}. \tag{5.65}$$

Without repeating the entire bifurcation analysis, the threshold value of γ (obtained by simulation of Eq. (5.61)) is displayed in Fig. 5.25 (a) for different spring characteristics. The corresponding initial velocity $\dot{x}(0) \triangleq \dot{x}_{\text{approx}}(0)$ is calculated according to Eq. (5.64) with $\omega_0 = 1, \epsilon = 0.05$, $\alpha = 3/4$ and shown in Fig. 5.25 (b). Springs inside the marked zone are not addressed because Eq. (5.61) involves a near resonant condition for these nearly linear springs which is clearly not representing the real response of (5.8). Further more, as opposed to springs outside the marked zone, there is no sudden rise in relative displacement as a function of γ or $\dot{x}(0)$ (Figs. 5.4 and 5.5). The term threshold is therefore not appropriate.

Table 5.1 compares the real value of $\dot{x}(0)$ for which the threshold is reached, i.e. $\dot{x}(0)$ corresponding to (5.8), with the value obtained through the simplified system (5.61). This is performed for different hardening and softening springs keeping $\omega_0 = 1, \epsilon = 0.05, \alpha = 3/4$. The threshold value for γ in Eq. (5.64) is also shown. The approximation is very good for powers 10, 5 and 3 while it is far worse for the softening springs. This is caused by the significantly larger relative amplitude for powers 1/3 and 1/5 compared to the other springs. Simply neglecting

Power of spring characteristic	10	5	3	2	1/10	1/5	1/3
γ	0.07	0.11	0.17	0.27	1.95	2.05	2.17
$\dot{x}_{\text{approx}}(0)$ (rad/s)	0.735	0.576	0.430	0.27	0.476	0.408	0.313
$\dot{x}_{\text{real}}(0)$ (rad/s)	0.74	0.581	0.418	0.31	0.53	0.460	0.410
Error (%)	0.6	0.86	2.72	12.9	10.19	11.37	23.66

Table 5.1: Comparison between real and approximated threshold values $\dot{x}(0)$

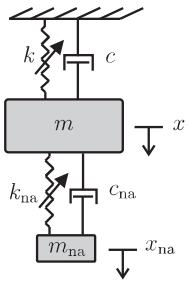

Figure 5.26: Nonlinear oscillator and nonlinear vibration absorber

$\frac{4}{3}\epsilon\alpha\ \text{sgn}(x - x_{\text{na}})|x - x_{\text{na}}|^p$ in (5.8) as done in Section 5.4 is then not acceptable any more.

5.6.2 Nonlinear main systems

Consider the transient response of a main system and attached vibration absorber, both with a nonlinear spring characteristic (Fig. 5.26). A tuning methodology for this system is presented in [41]. The approach is to tune the absorber such that it has the same frequency-energy dependence as that of the nonlinear main system. A necessary condition to meet this requirement is that both the main system and the absorber need to posses the same nonlinear functional form. For instance, for a main system with cubic nonlinearity one would attach a vibration absorber with cubic nonlinearity

$$\begin{cases} m\ddot{x} + kx^3 + c_{\text{na}}(\dot{x} - \dot{x}_{\text{na}}) + k_{\text{na}}(x - x_{\text{na}})^3 = 0 \\ m_{\text{na}}\ddot{x}_{\text{na}} + c_{\text{na}}(\dot{x}_{\text{na}} - \dot{x}) + k_{\text{na}}(x_{\text{na}} - x)^3 = 0. \end{cases} \tag{5.66}$$

For an initial displacement $x_{\text{na}}(0)$, the frequency energy dependence for the cubic absorber is given by

$$E_{\text{na}}(\omega) = \frac{1}{4}k_{\text{na}}x_{\text{na}}^4(0) \tag{5.67}$$

$$= \frac{4}{9}\frac{m_{\text{na}}^2}{k_{\text{na}}}\omega^4 \tag{5.68}$$

where in the last step Eq. (5.3) is used with $A = x_{\text{na}}(0)$. Imposing $E_{\text{na}}(\omega) = E(\omega)$ results in

$$\frac{m_{na}^2}{k_{na}} = \frac{m^2}{k}. \tag{5.69}$$

This tuning procedure has an interesting outcome. The absorber is able to mitigate the vibrations of the main system regardless of its input energy, a feature which is normally only present in linear systems. The drawback of this approach is that only qualitative results are obtained. It does not succeed in pointing out the required absorber parameters to achieve optimal vibration reduction. Here, we extend the analysis of Section 5.4 to nonlinear main systems and achieve both qualitative and quantitative results.

Again the underlying Hamiltonian system ($c = 0$ and $c_{na} = 0$) is considered. Dividing (5.66) by m yields

$$\begin{cases} \ddot{x} + \frac{k}{m}x^3 + \epsilon\frac{k_{\text{na}}}{m_{\text{na}}}(x - x_{\text{na}})^3 = 0 \\ \ddot{x}_{\text{na}} + \frac{k_{\text{na}}}{m_{\text{na}}}(x_{\text{na}} - x)^3 = 0 \end{cases} \tag{5.70}$$

System (5.70) can be analyzed similarly to Section 5.4 by neglecting $\epsilon\frac{k_{\text{na}}}{m_{\text{na}}}(x - x_{\text{na}})^3$ in (5.70). According to Section 5.2.1 this means that the response of the nonlinear main system is approximated by

$$x(t) \approx \sqrt{x(0)^2 + \frac{\dot{x}(0)^2}{\omega_{eq}^2}}\sin(\omega_{eq}t + \phi); \qquad \omega_{eq}^4 = \frac{3k}{4m}\left(\omega_{eq}^2 x(0)^2 + \dot{x}(0)^2\right). \tag{5.71}$$

Similar to Section 5.3, the second equation of (5.70) can be recast into dimensionless form

$$\frac{d^2x_{\text{d}}}{d\tau^2} + \gamma x_{\text{d}}^3 = \sin(\tau + \phi) \tag{5.72}$$

with γ

$$\gamma = \frac{k_{na}}{m_{na}}\frac{(x(0)^2\omega_{eq}^2 + \dot{x}(0)^2)}{\omega_{eq}^4}. \tag{5.73}$$

Finally, substituting ω_{eq}^4 of Eq. (5.71) into Eq. (5.73) yields

$$\gamma = \frac{4}{3}\frac{\left(\frac{k_{na}}{m_{na}}\right)}{\left(\frac{k}{m}\right)}. \tag{5.74}$$

In Section 5.4 where a nonlinear absorber was attached to a linear main system, it was found that for impulsive orbits (i.e. energy initially localized to the nonlinear

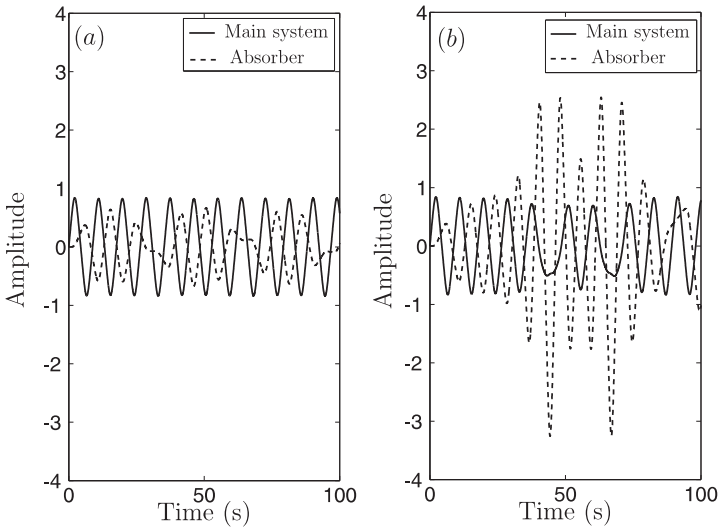

Figure 5.27: Response of cubic absorber attached to cubic main system ($m = 1, c = 0, k = 1, m_{na} = 0.05, c_{na} = 0$) *for initial conditions* $\dot{x}(0) = 0.5$, $x(0) = \dot{x}_{na}(0) = x_{na}(0) = 0$; *(a)* $k_{na} = 0.0065$ *(b)* $k_{na} = 0.0068$

main system) efficient vibration reduction is only possible for $\gamma > 0.18$. Here the same value can be used such that efficient vibration reduction can only be achieved when

$$\frac{k_{na}}{m_{na}} \geq 0.135 \frac{k}{m} \tag{5.75}$$

Up to a constant Eq. (5.75) strongly resembles the tuning procedure of a linear absorber attached to a linear main system. In other words, the threshold value for γ does not depend on the initial conditions of the main nonlinear system which agrees with the qualitative results found in [41]. Moreover, simulations for k_{na} close to the value suggested by Eq. (5.75) also confirm its quantitative validity. Indeed, as demonstrated by Fig. 5.27, a clear jump in the amplitude of the absorber is visible for $k_{na} \approx 0.0068$ while $k_{na} \approx 0.0067$ is obtained with Eq. (5.75) validating in this way the approximate analysis for nonlinear main systems as well.

5.6.3 Harmonically forced linear main system

The analysis of Section 5.4 can be used as long as the response of the primary system can be approximated by a sine function. Consequently, the same approach can be

applied for a nonlinear absorber attached to a harmonically forced LO governed by

$$\begin{cases} m\ddot{x} + c\dot{x} + kx + c_{\text{na}}(\dot{x} - \dot{x}_{\text{na}}) + k_{\text{na}}(x - x_{\text{na}})^3 = F\sin(\omega t) \\ m_{\text{na}}\ddot{x}_{\text{na}} + c_{\text{na}}(\dot{x}_{\text{na}} - \dot{x}) + k_{\text{na}}(x_{\text{na}} - x)^3 = 0. \end{cases} \tag{5.76}$$

where we assume that the system is initially at rest, i.e. $\dot{x}(0) = x(0) = x_{\text{na}}(0) = \dot{x}_{\text{na}}(0) = 0$. As opposed to the previous sections where the underlying Hamiltonian system ($c = c_{\text{na}} = 0$) was considered, we cannot put $c = 0$ here because the transient response would never fade out in this case preventing the required sinusoidal response of the LO. Taking $c_{\text{na}} = 0$ and dividing (5.76) by m yields

$$\begin{cases} \ddot{x} + 2\zeta\omega_0\dot{x} + \omega_0^2 x + \epsilon\frac{k_{\text{na}}}{m_{\text{na}}}(x - x_{\text{na}})^3 = \frac{F}{m}\sin(\omega t) \\ \ddot{x}_{\text{na}} + \frac{k_{\text{na}}}{m_{\text{na}}}(x_{\text{na}} - x)^3 = 0. \end{cases} \tag{5.77}$$

with $\zeta = \frac{c}{2m\omega_0}$. After omitting the terms in ϵ the approximated steady state response of the LO becomes

$$x(t) \approx a(\omega)F\sin(\omega t + \phi(\omega)) \tag{5.78}$$

with

$$a(\omega) = \frac{1}{m\omega_0^2}\frac{1}{\sqrt{(1 - (\frac{\omega}{\omega_0})^2)^2 + 4\zeta^2(\frac{\omega}{\omega_0})^2}} \tag{5.79}$$

$$\phi(\omega) = -\arctan\left(\frac{2\zeta\omega_0\omega}{\omega_0^2 - \omega^2}\right) \tag{5.80}$$

After substituting (5.78) into the second equation of (5.77), it can be recast into dimensionless form

$$\frac{d^2x_{\text{d}}}{d\tau^2} + \gamma x_{\text{d}}^3 = \sin(\tau + \phi(\omega)) \tag{5.81}$$

where γ is determined by substituting $X = \omega^2 a(\omega)F$ into Eq. (5.35)

$$\gamma = \frac{k_{na}}{m_{na}}\frac{a^2(\omega)F^2}{\omega^2}. \tag{5.82}$$

Again, the threshold value $\gamma \approx 0.18$ can be used to separate weak from strong absorber movement.

Remark It should be noted here that this approach is only accurate if the response of the LO is indeed sinusoidal. When large transients are present (e.g. amplitude buildup in a resonant condition) the LO response is not sinusoidal and no accurate results will be obtained.

5.7 Conclusion

A large amount of research has recently been conducted in the development of strongly nonlinear vibration absorbers in an effort to outperform the classical linear absorber. This chapter has focussed on an important feature of this new type of absorbers, namely their energy threshold values. These energy threshold values are crucial in a design procedure of the nonlinear absorber because they define a clear boundary between efficient and inefficient vibration reduction. After nondimensionizing the system, an approximate analysis revealed the influence of the different system parameters (initial energy, stiffness and mass of absorber and primary system) on the energy threshold value in a closed form expression. Using this result, we were able to extend the concept of an energy threshold to a more general parameter threshold value where each parameter is featuring its own threshold value. In other words, the analysis can point out which regions in parameter space are capable of efficient vibration reduction and which are not. Further more, it was shown that the same analysis can also be applied to nonlinear primary systems and forced linear primary systems, driving this analysis as a general applicable tool relevant in the further development of strongly nonlinear vibration absorbers.

6

Experimental results in a torsional vibration setup

6.1 Introduction

The previous chapter revealed that regarding impulsive orbits only a subspace of the parameter space (including mass, stiffness and initial conditions) corresponds to strong absorber movement. Moreover, this subspace has clearly defined boundaries and the transition to regions with weak absorber movement living outside this subspace happens in a discontinuous fashion, i.e. only a very small variation of a parameter value results in a very large variation of the absorber movement. This remarkable behavior is crucial when practically implementing a strongly nonlinear vibration absorber and is therefore experimentally verified in this chapter.

The practical implementation of the absorber 's strongly nonlinear stiffness (e.g. cubic stiffness) is generally accomplished by using two linear springs according to Fig. 6.1. Both springs are initially unloaded (otherwise a linear stiffness term is introduced) and a force F perpendicular to the direction of the springs is applied (Fig. 6.1 (a)), causing a nearly cubic relationship between F and x (Fig. 6.1 (b)), i.e. $F \approx kx^3$.

Besides using springs as in [42], other implementations involve replacing the springs by a steel wire [43], [44] or a thin steel blade [45]. In this chapter, we also use the spring steel wire, but in a torsional vibration setting rather than the rectilinear setting used in the aforementioned references.

After describing the setup in Section 6.2, both the primary system and the

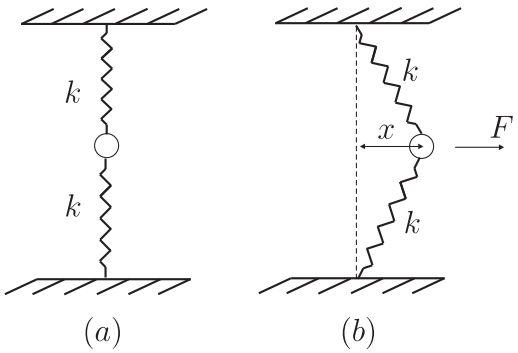

Figure 6.1: Practical implementation of a cubic stiffness

absorber are theoretically modeled in Section 6.3. This allows to determine the most influential parameters in the design. An accurate comparison between theoretical and experimental results is not presented as this requires a detailed (nonlinear) system identification which falls outside the scope of this dissertation.

Nevertheless, experiments in transient as well as steady state conditions described in Sections 6.4 and 6.5 demonstrate that the wire absorber indeed exhibits regions with weak and strong absorber movement. Moreover, in both cases the threshold phenomenon, a discontinuous transition from weak to strong absorber movement, is clearly observed.

Despite these encouraging results, some drawbacks of using a wire absorber should be noted. First of all, the degree of nonlinearity is very difficult to control. Two reasons for this are the perfect clamping requirement and the difficulty to prevent pre-tension of the wire. Secondly, the functional form is limited to a cubic nonlinearity. In a first attempt to resolve these limitations, a different implementation is proposed in Section 6.6 which could be the subject of further research.

6.2 Torsional vibration setup

The setup under study is shown in Figs. 6.2- 6.5. In Fig. 6.2, the damped primary system is highlighted in red. It is a small-scale model of a drive line acting as a benchmark system for many industrial applications. It basically consists of a steel spring shaft which serves as the torsional stiffness of the primary system with attached to it up to 4 steel disks providing the moment of inertia of the vibratory system. Damping is present both in relative and absolute form. The former describes the damping between the different disks, in this case material damping of the steel shaft. The latter denotes the damping to ground caused by the ball bearings at each of the disks.

The input to the primary system is provided by an electrical servomotor which

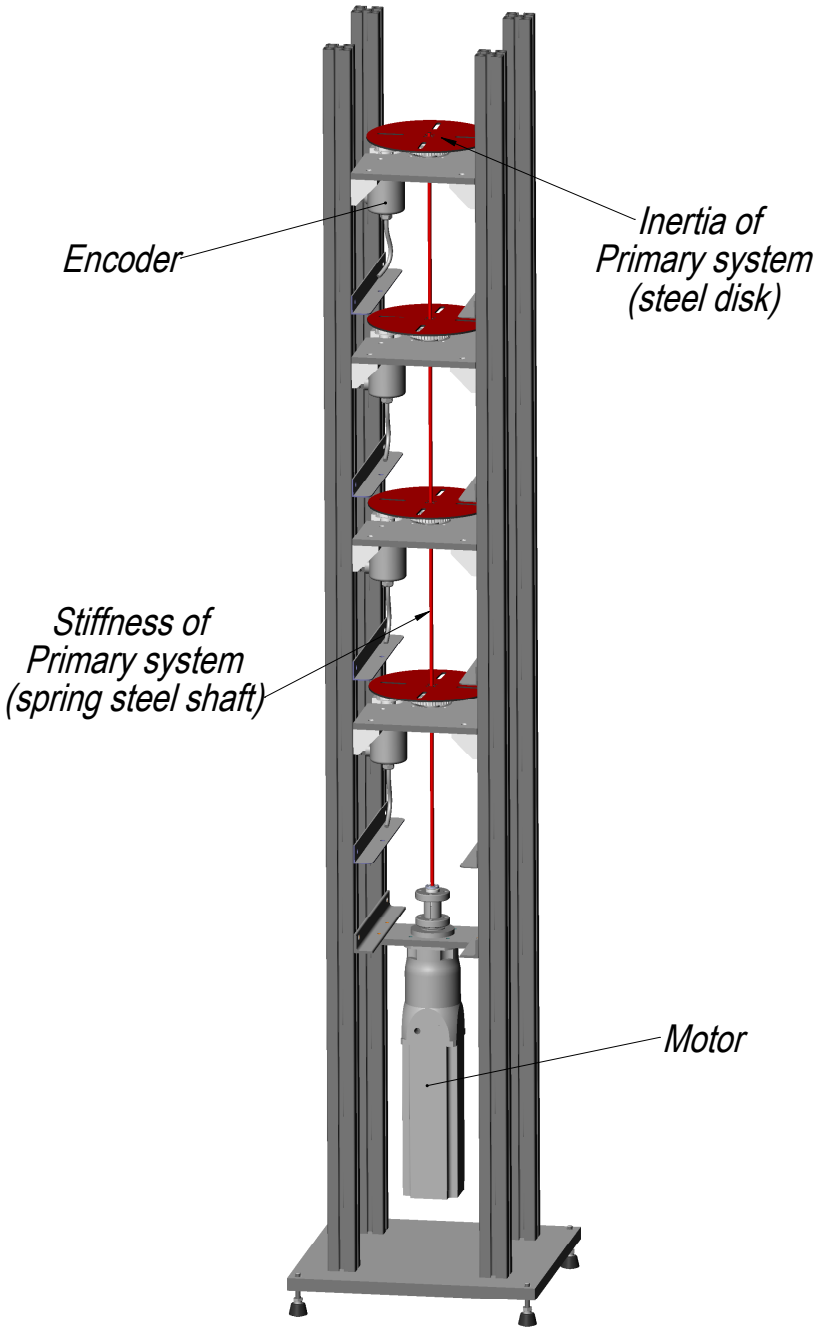

Figure 6.2: Torsional vibration setup - Primary system

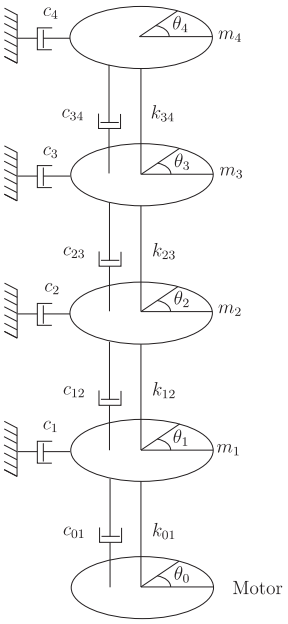

Figure 6.3: Schematic view of the primary system

is able to initiate both transient (e.g. short impulse) and steady state (e.g. sinusoidal excitation) behavior. The corresponding rotational responses of the different disks are measured with position encoders. A $1:2$ belt transmission in between disk and encoder increases the resolution of the position measurement.

A schematic view of the primary system is shown in Fig. 6.3. It can be modeled as a 4DOF system with generalized coordinates $\theta_i, \quad i = 1, ..., 4$. The rotation of the motor is denoted by θ_0. Except for c_i and c_{ij}, all parameters k_{ij} and $m_i, \quad i, j = 1, ..., 4$ can be easily varied. The different disks can be attached anywhere along the shaft (changing k_{ij}) or even completely detached from the shaft (changing the number of DOFs). Their moment of inertia can also be increased by attaching extra mass (increasing m_i).

A nonlinear absorber is attached at the top disk as shown in Fig. 6.4 (highlighted in blue), a detailed view is given in Fig. 6.5. It consists of a steel disk (inertia of the SDOF absorber) connected to the top disk of the primary system with steel wires (nonlinear stiffness of the absorber). A deep groove ball bearing transmits the axial and radial forces of the absorber to ground. Again, a large flexibility in the design of the absorber is possible. Extra mass can be added to increase its inertia while the stiffness coefficient of the nonlinear spring can be changed by adjusting the number, length, diameter and radial distance of the wires.

Damping is difficult to model theoretically and in practice it is still hard to

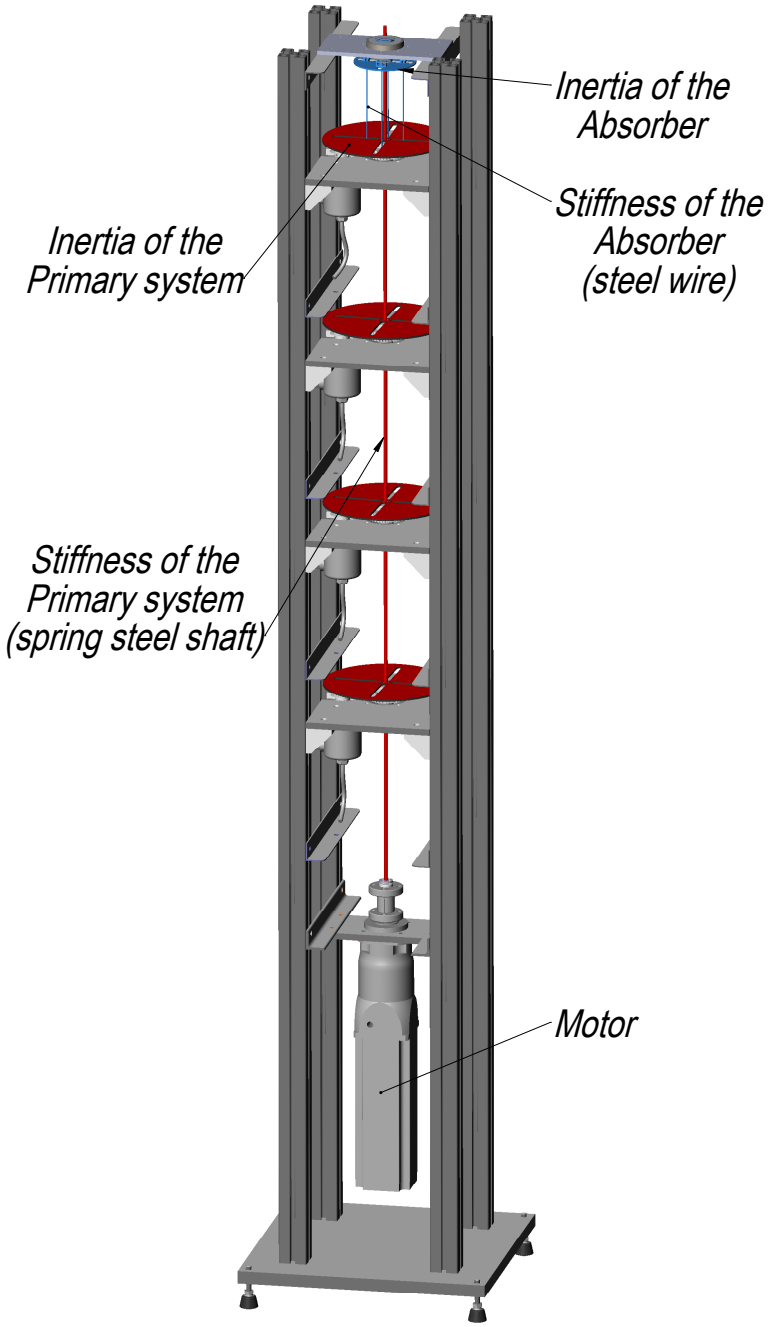

Figure 6.4: Torsional vibration setup - Primary system and absorber

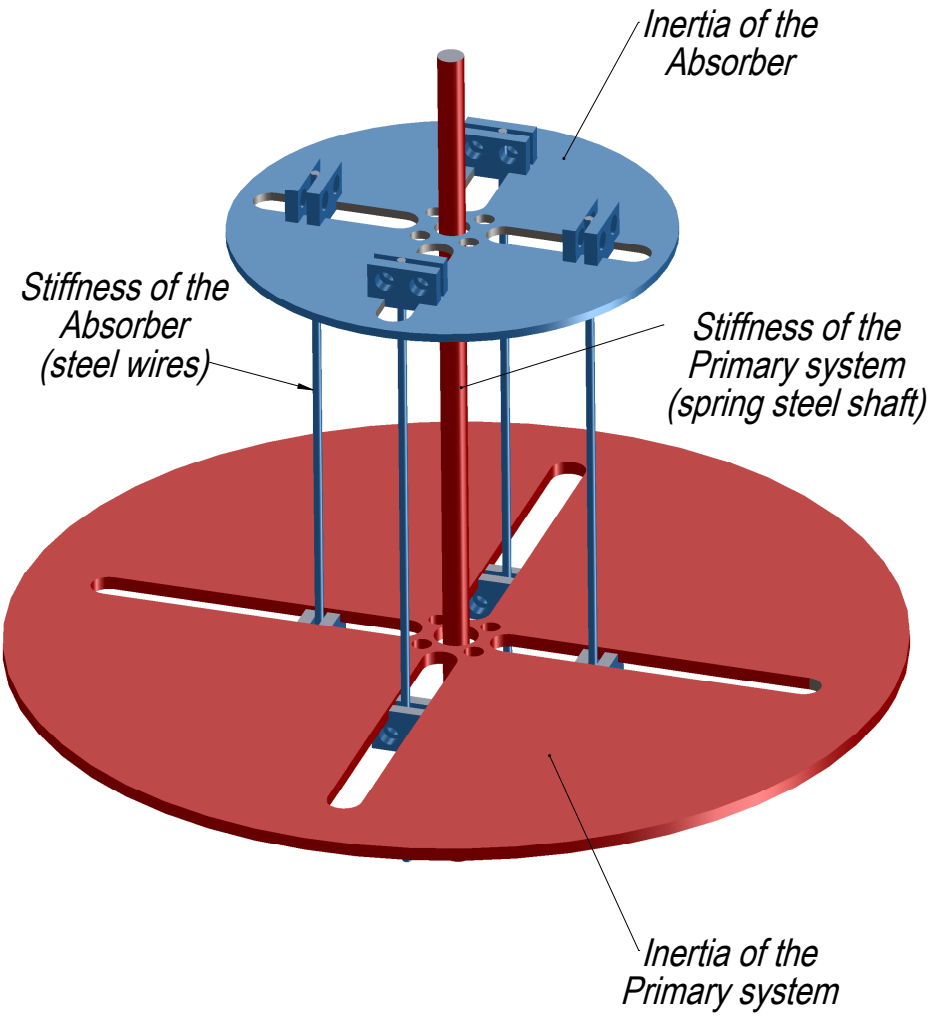

Figure 6.5: Torsional vibration setup - Primary system and absorber

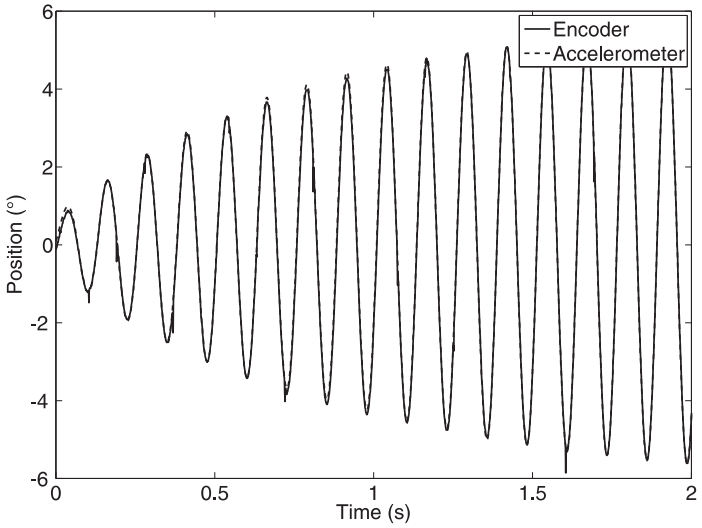

Figure 6.6: Comparison between double integrated acceleration signal and encoder signal

control. Therefore, damping in between the absorber and the primary system is not implemented. The lubrication in the deep groove ball bearing (damping to ground) has also been removed to further minimize the effect of damping. This means that efficient vibration reduction cannot be realized. However, our main goal here is to experimentally verify the existence of boundaries separating weak and strong absorber movement. As discussed in Chapter 5, these boundaries are mainly influenced by the underlying Hamiltonian system justifying the exclusion of damping.

The response of the absorber is measured by taking the averaged response of 2 diametrically opposed accelerometers, each measuring the tangential acceleration at a radial distance r_a from the center of the absorber disk. This acceleration signal is twice numerically integrated over time and divided by r_a to obtain the rotational position of the absorber. To verify this approach, the accelerometers were first attached to the top disk of the primary system in order to compare their outcome with that of the encoder. The calibration is limited to a sine excitation of 8 Hz because this is also the main frequency in the experiments. As shown in Fig. 6.6 a very good agreement is obtained.

6.3 Theoretical modeling

The agreement between theory and practice is generally not perfect. Nevertheless, a theoretical model provides crucial information on the qualitative behavior of the corresponding practical implementation. For both the primary system and the

nonlinear absorber, a theoretical model is developed pointing out the influence of the different parameters.

6.3.1 Primary system

The primary system can be accurately modeled as a 4DOF system with mass, damping and stiffness matrices M, C and K given by

$$M = \begin{bmatrix} m_1 & 0 & 0 & 0 \\ 0 & m_2 & 0 & 0 \\ 0 & 0 & m_3 & 0 \\ 0 & 0 & 0 & m_4 \end{bmatrix} \tag{6.1}$$

$$C = \begin{bmatrix} c_1 + c_{01} + c_{12} & -c_{12} & 0 & 0 \\ -c_{12} & c_2 + c_{12} + c_{23} & -c_{23} & 0 \\ 0 & -c_{23} & c_3 + c_{23} + c_{34} & -c_{34} \\ 0 & 0 & -c_{34} & c_4 + c_{34} \end{bmatrix} \tag{6.2}$$

$$K = \begin{bmatrix} k_{01} + k_{12} & -k_{12} & 0 & 0 \\ -k_{12} & k_{12} + k_{23} & -k_{23} & 0 \\ 0 & -k_{23} & k_{23} + k_{34} & -k_{34} \\ 0 & 0 & -k_{34} & k_{34} \end{bmatrix} \tag{6.3}$$

and corresponding equations of motion

$$M\ddot{\theta} + C\dot{\theta} + K\theta = 0. \tag{6.4}$$

$\theta = [\theta_1 \ \theta_2 \ \theta_3 \ \theta_4]^T$ is the vector of generalized coordinates each denoting the absolute rotation (relative to ground). The mass moments of inertia $m_i \quad i = 1, ..., 4$ as listed in Table 6.1 are determined with Solidworks®, a 3D mechanical CAD (computer-aided design) program. Each m_i consists of the disk inertia $m_{i,d}$ and the remaining inertia $m_{i,r}$ added by the encoder and the transmission gears. The torsional stiffness of the spring steel shaft is given by

$$k_{ij} = \frac{\pi G}{32 L_{ij}} D^4 \tag{6.5}$$

with G the shear modulus, D the diameter of the spring steel shaft and L_{ij} the length of the shaft in between disks i and j. The numerical values of k_{ij} used in the experiments are given in Table 6.1. Although no theoretical model of the damping is available, a viscous type of damping is assumed in (6.4). This is standard practice and allows a simplified mathematical analysis.

In the experiments described in Sections 6.4 and 6.5, the lower disks 1, 2 and 3 are detached from the shaft. Consequently, the mass matrix M becomes

$$M = \begin{bmatrix} m_{1,r} & 0 & 0 & 0 \\ 0 & m_{2,r} & 0 & 0 \\ 0 & 0 & m_{3,r} & 0 \\ 0 & 0 & 0 & m_4 \end{bmatrix} \tag{6.6}$$

Parameter	Value
$m_{i,d}$	$35.22 \cdot 10^{-4}$kg m^2
$m_{i,r}$	$1.78 \cdot 10^{-4}$kg m^2
G	$81.5 \cdot 10^{9}$ N/m^2
D	$6 \cdot 10^{-3}$ m
L_{ij}	$30 \cdot 10^{-2}$ m
m_i	$37 \cdot 10^{-4}$kg m^2
k_{ij}	34.57 Nm/rad

Table 6.1: Numerical values used in the experiments

Natural frequency	Value
ω_1	7.7 Hz
ω_2	$5.4 \cdot 10^2$ Hz
ω_3	$9.9 \cdot 10^2$ Hz
ω_4	$12.9 \cdot 10^2$ Hz

Table 6.2: Natural frequencies of the experimental setup with disks 1, 2 and 3 detached

while C and K remain unaltered. The resulting natural frequencies are listed in Table 6.2. Because ω_2 is O(10^2) larger than ω_1 and only frequencies below 10 Hz will be excited in the experiments, the system can accurately be regarded as a SDOF system.

Remark By introducing a ground rotation θ_0 forced by the servomotor, the equation of motion corresponding to θ_1 becomes

$$m_1\ddot{\theta}_1 + c_1\dot{\theta}_1 + c_{01}(\dot{\theta}_1 - \dot{\theta}_0) + k_{01}(\theta_1 - \theta_0) = 0 \tag{6.7}$$

or

$$m_1\ddot{\theta}_1 + c_1\dot{\theta}_1 + c_{01}\dot{\theta}_1 + k_{01}\theta_1 = c_{01}\dot{\theta}_0 + k_{01}\theta_0 \tag{6.8}$$

while the equations of motion corresponding to θ_2, θ_3 and θ_4 remain unaltered. Equation 6.8 shows that introducing a rotation θ_0 of the motor is equivalent to a torque $c_{01}\dot{\theta}_0 + k_{01}\theta_0$ applied to the first disk of the primary system when it is grounded at the motor (Fig. 6.7). Moving to the Laplace domain, the corresponding

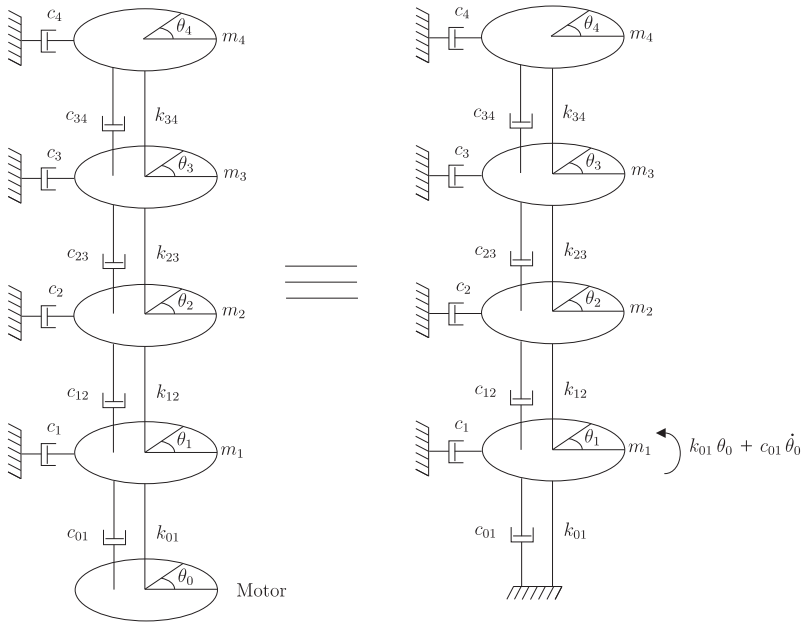

Figure 6.7: Equivalence between motor rotation θ_0 and torque at disk 1 applied to grounded primary system

transfer function between $\Theta(s)$ and $\Theta_0(s)$ becomes

$$\Theta(s) = \left(Ms^2 + Cs + K\right)^{-1} \begin{bmatrix} c_{01}s + k_{01} \\ 0 \\ 0 \\ 0 \end{bmatrix} \Theta_0(s). \tag{6.9}$$

In system identification, we are typically interested in $H(s) = \left(Ms^2 + Cs + K\right)^{-1}$. Equation (6.9) however shows that the base excitation of the motor causes an extra scaling term $c_{01}s + k_{01}$.

6.3.2 Nonlinear attachment

Here we prove that the absorber wire of Fig. 6.5 approximates a cubic spring, i.e. its elastic couple $T(\theta) \approx k_{\text{na}}\theta^3$. Consider to this end Fig. 6.8 where two disks are shown connected by a wire spring (without pre-tension) which is attached to both disks at a distance r from their center. One of the disks is rotated over an angle θ elongating in this way the wire spring from l to l_n. This elongation causes an axial force F_A in the wire which can be projected onto the plane of the disk by

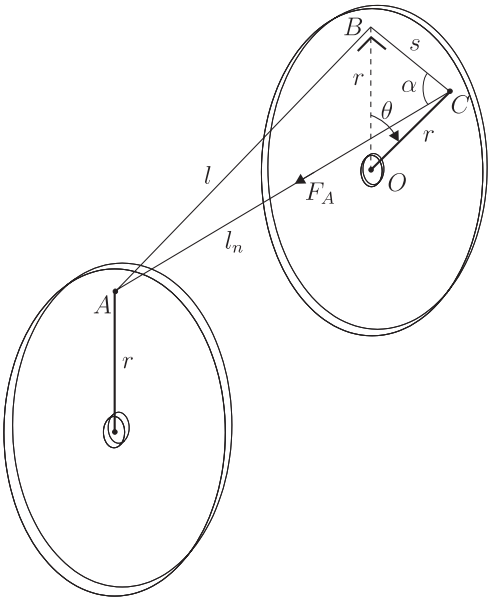

Figure 6.8: Elongation of a wire from length l to l_n due to a rotation over angle θ

considering the triangle ABC

$$F_s = F_A \cos\alpha \tag{6.10}$$
$$= F_A \frac{s}{l_n} \tag{6.11}$$

The resulting force F_s lies in the direction of s as displayed in Fig. 6.9 and causes a torque T_A around the center of the disk

$$T_A = F_s \cos\left(\frac{\theta}{2}\right) r \tag{6.12}$$
$$= F_A \frac{s}{l_n} \cos\left(\frac{\theta}{2}\right) r \tag{6.13}$$

The final task is to transform T_A of Eq. (6.13) into a function of θ. Substituting

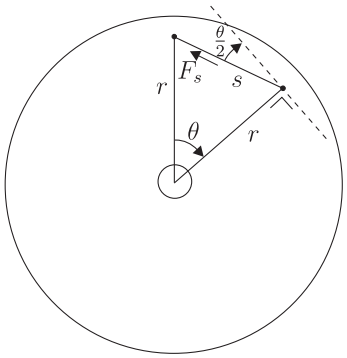

Figure 6.9: Derivation of the torque as a function of θ

$F_A = k_A(l_n - l)$ (with k_A the axial stiffness of the wire) into Eq. (6.13) yields

$$T_A = k_A \cos\left(\frac{\theta}{2}\right) rs \left[\frac{l_n - l}{l_n}\right]; \qquad l_n = \sqrt{l^2 + s^2} \tag{6.14}$$

$$= k_A \cos\left(\frac{\theta}{2}\right) rs \left[1 - \frac{l}{\sqrt{l^2 + s^2}}\right] \tag{6.15}$$

$$= k_A \cos\left(\frac{\theta}{2}\right) rs \left[1 - \left(1 - \frac{1}{2}\left(\frac{s}{l}\right)^2 - O(s^4)\right)\right] \tag{6.16}$$

$$= k_A \cos\left(\frac{\theta}{2}\right) \frac{rs^3}{2l^2} + O(s^5) \tag{6.17}$$

where a binomial series is used in the last step. With $s = 2r\sin\left(\frac{\theta}{2}\right)$, Eq. (6.17) becomes

$$T_A = \frac{4k_A r^4}{l^2} \cos\left(\frac{\theta}{2}\right) \sin^3\left(\frac{\theta}{2}\right) + O(\theta^5) \tag{6.18}$$

$$= \frac{4k_A r^4}{l^2} \left[1 - \frac{1}{2}\left(\frac{\theta}{2}\right)^2 + O(\theta^4)\right] \left[\frac{\theta}{2} - \frac{1}{6}\left(\frac{\theta}{2}\right)^3 + O(\theta^5)\right]^3 \tag{6.19}$$

$$= \frac{k_A r^4}{2l^2}\theta^3 + O(\theta^5) \tag{6.20}$$

By rewriting the axial stiffness of the wire as $k_A = \frac{EA}{l}$ with E Young's modulus and A the cross section of the wire, the final form of the elastic torque T_A becomes

$$T_A = \frac{EAr^4}{2l^3}\theta^3 + O(\theta^5) \tag{6.21}$$

showing that up to $O(\theta^5)$ the wire spring is indeed cubic.

Up till now only axial deformation of the wire has been considered. However, in practice the wire is clamped at both disks which besides axial deformation also

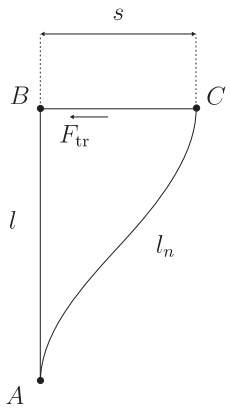

Figure 6.10: Transversal deformation of the clamped-clamped wire in the plane of ABC

causes torsional and transversal deformation of the wire. The torsional deformation adds a linear torque T_{to}

$$T_{\text{to}} = \frac{G\pi r_{\text{w}}^4}{2l}\theta \tag{6.22}$$

with G the shear modulus and r_{w} the wire's radius. The effect of the transversal deformation can be understood from Fig. 6.10 which shows the plane of the triangle ABC (Fig. 6.8) where the clamped-clamped wire is located in. The deformation $s = 2r\sin\left(\frac{\theta}{2}\right)$ results in a force F_{tr}

$$F_{\text{tr}} = k_{\text{tr}}s \tag{6.23}$$

$$= 12\frac{EI}{l^3}2r\sin\left(\frac{\theta}{2}\right) \tag{6.24}$$

which lies along the direction of s. The resulting torque T_{tr} around O becomes

$$T_{\text{tr}} = F_{\text{tr}}r\cos\left(\frac{\theta}{2}\right) \tag{6.25}$$

$$= 12\frac{EI}{l^3}r^2\left(\theta - \frac{\theta^3}{6}\right) + O(\theta^5) \tag{6.26}$$

Note that the cubic term has a negative sign opposing the cubic term of Eq. (6.21). Finally, the total torque T_{tot} is determined by adding the torques caused by axial,

Parameter	Value
E	$210 \cdot 10^9$ N/m^2
G	$70 \cdot 10^9$ N/m^2
r_{w}	$25 \cdot 10^{-5}$ m
r	$3.6 \cdot 10^{-2}$ m
l	$14.6 \cdot 10^{-2}$ m
k_{lina}	$6.1 \cdot 10^{-3}$ Nm/rad
k_{na}	11.1 Nm/rad^3
m_{na}	$1.7 \cdot 10^{-4}$ kg m^2

Table 6.3: Numerical values used in experiments

torsional and transversal deformation

$$T_{\text{tot}} = T_A + T_{\text{to}} + T_{\text{tr}} \tag{6.27}$$

$$= \left(\frac{G\pi r_{\text{w}}^4}{2l} + 12\frac{EI}{l^3}r^2\right)\theta + \left(\frac{EAr^4}{2l^3} - 2\frac{EI}{l^3}r^2\right)\theta^3 + O(\theta^5) \tag{6.28}$$

$$= \left(\frac{G\pi r_{\text{w}}^4}{2l} + 3\frac{E\pi r_{\text{w}}^4}{l^3}r^2\right)\theta + \left(\frac{E\pi r_{\text{w}}^2 r^4}{2l^3} - \frac{E\pi r_{\text{w}}^4}{2l^3}r^2\right)\theta^3 + O(\theta^5) \tag{6.29}$$

$$= \frac{E\pi r_{\text{w}}^4 r^2}{2l^3}\left[\left(\frac{G}{E}\frac{l^2}{r^2} + 6\right)\theta + \left(\frac{r^2}{r_{\text{w}}^2} - 1\right)\theta^3\right] + O(\theta^5) \tag{6.30}$$

$$= k_{\text{lina}}\theta + k_{\text{na}}\theta^3. \tag{6.31}$$

Consequently, by choosing for instance l/r of $O(1)$ and r/r_{w} of $O(10^2)$, the wire can be approximated as a cubic spring

$$T_{\text{tot}} \approx \frac{E\pi r_{\text{w}}^2 r^4}{2l^3}\theta^3 \tag{6.32}$$

$$= k_{\text{na}}\theta^3 \tag{6.33}$$

The numerical values of the different parameters used in the experiments (including the absorber inertia m_{na}) are listed in Table 6.3 showing that the nonlinear stiffness k_{na} is an order 10^3 larger than the linear stiffness k_{lina}. Hence, assuming a cubic spring is justified.

Experimental verification

A static test is used to verify the theoretically calculated nonlinear characteristic of the wire spring. The nonlinear absorber is clamped at the top, while at the bottom

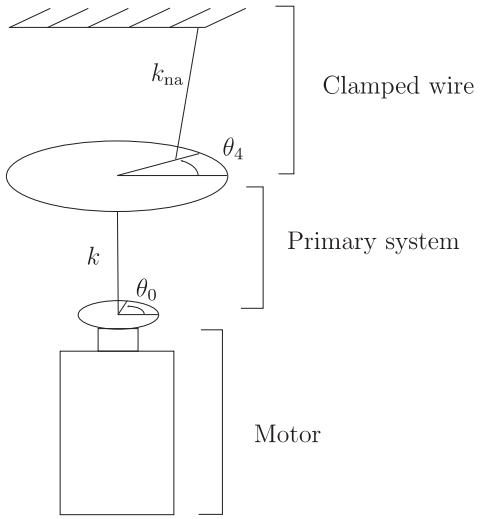

Figure 6.11: Scheme of the experimental determination of the wire spring characteristic

of the setup (Fig. 6.11) the rotation of the motor is increased in small steps (θ_0). After each step the position at the top disk of the primary system (θ_4) is measured with the encoder. In each step, the torque T_d at the disk (with k known) is

$$T_d = k(\theta_0 - \theta_4). \tag{6.34}$$

The same torque is applied to the clamped wire. Consequently, the spring characteristic of the wire can be visualized by plotting T_d as a function of θ_4 (Fig. 6.12, $---$). The corresponding least squares approximation by a third order polynomial $p = 4.67\theta_2^3 - 0.019\theta_2^2 + 0.13\theta_2 + 0.0014$ shows that the wire indeed behaves like a cubic spring with a small linear term. The quantitative agreement with the theoretical modeling of the wire (Table 6.3) is however less accurate as in theory a larger cubic term ($k_{\mathrm{na}} = 11.1$ Nm/rad^3) is obtained. One possible reason is the assumption of a perfect clamping. In practice, this is not realizable causing a lower stiffness value.

In the experimentally derived curve, some artefacts are clearly present for smaller θ_4. In this region the counteracting torque created by the wire is very small because its stiffness is mainly cubic. Consequently, other effects like static friction and the wire not being perfectly straight take the upper hand. For larger θ_4 however the influence of these side effects is negligible resulting in an excellent agreement with the third order polynomial.

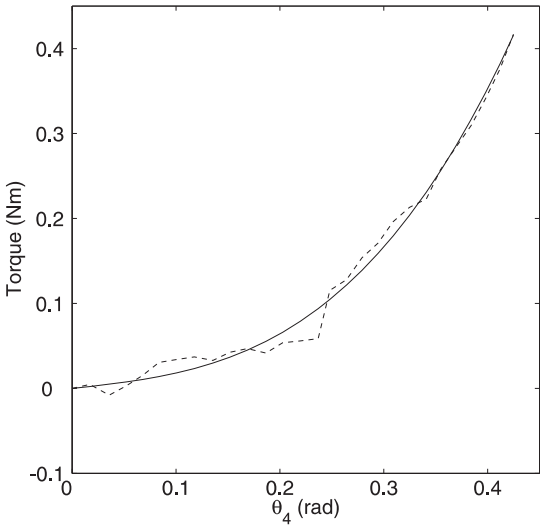

Figure 6.12: Experimentally (− − −) derived nonlinear spring characteristic of the wire and least squares approximation (——)

6.4 Experiments in transient conditions

These experiments were performed with disks 1, 2 and 3 detached from the shaft. As discussed in Section 6.3 this results in a nearly SDOF primary system with natural frequency $\omega_0 \approx 8Hz$. The inertia of the absorber as listed in Table 6.3 is increased to $m_{\text{na}} = 2.5 \cdot 10^{-4}$ kg m^2. The other parameters are left unchanged.

The experiments are used to verify the existence of an energy threshold. To this end, the motor exerts a short impulse which is varied only slightly in intensity as displayed in Fig. 6.13. The corresponding responses of the primary system and the absorber ,shown in Figs. 6.14 and 6.15, demonstrate the existence of an energy threshold and the accompanying jump in amplitude. Indeed, compared to Fig. 6.14, the amplitude of the absorber displayed in Fig. 6.15 is more than doubled while the intensity of the motor impulse (integration of motor impulse over time) is only 1% larger.

Both absorber responses are shown more clearly in Fig. 6.16. Below the energy threshold, the absorber almost immediately runs into lower frequencies while a clear 1:1 resonance capture is present above the threshold for $t < 0.5$s, i.e. both the absorber and the primary system vibrate at the same frequency. For $t > 0.5$s, the 1:1 resonance capture no longer exists and lower frequencies are introduced.

These observations are more clearly illustrated in Figs. 6.17-6.18 by means of the corresponding Morlet wavelet transforms showing the evolution of frequency with respect to time. In these plots, a larger frequency content corresponds to a

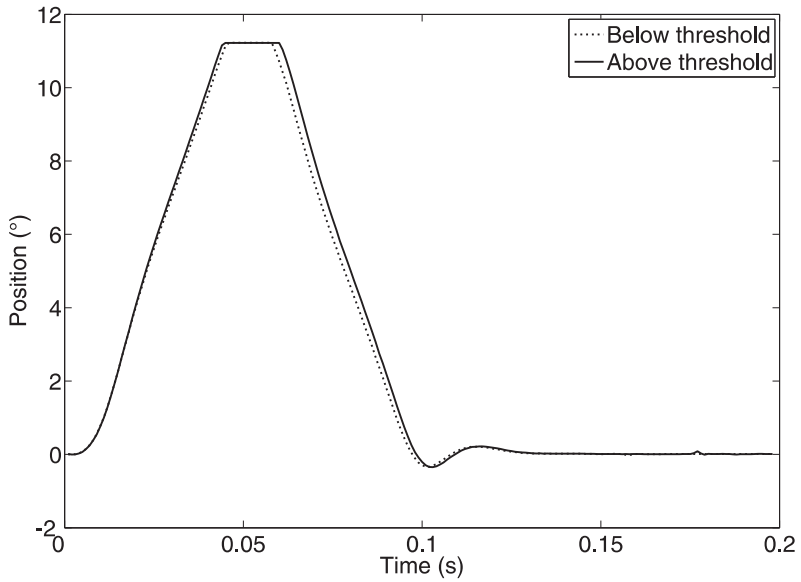

Figure 6.13: Motor impulse below (· · ·) and above (——) the energy threshold with a difference of only 1% in intensity

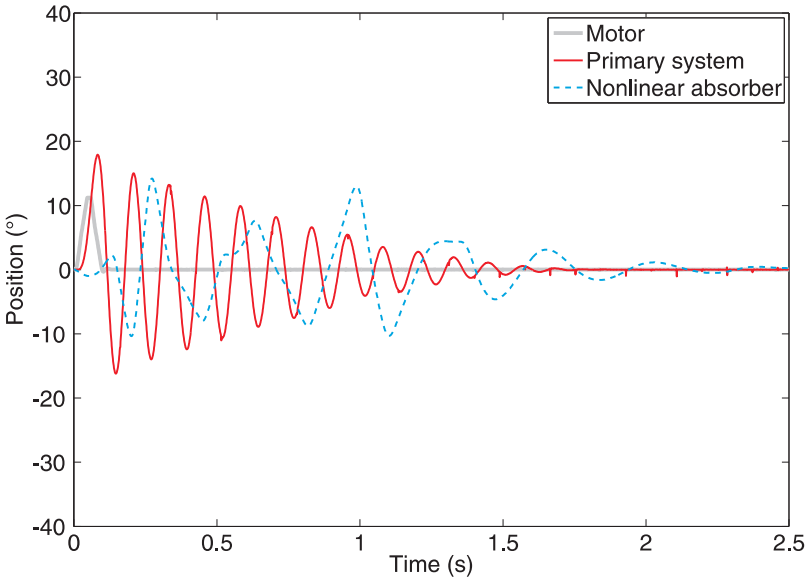

Figure 6.14: Primary system and absorber response to a motor impulse below the energy threshold

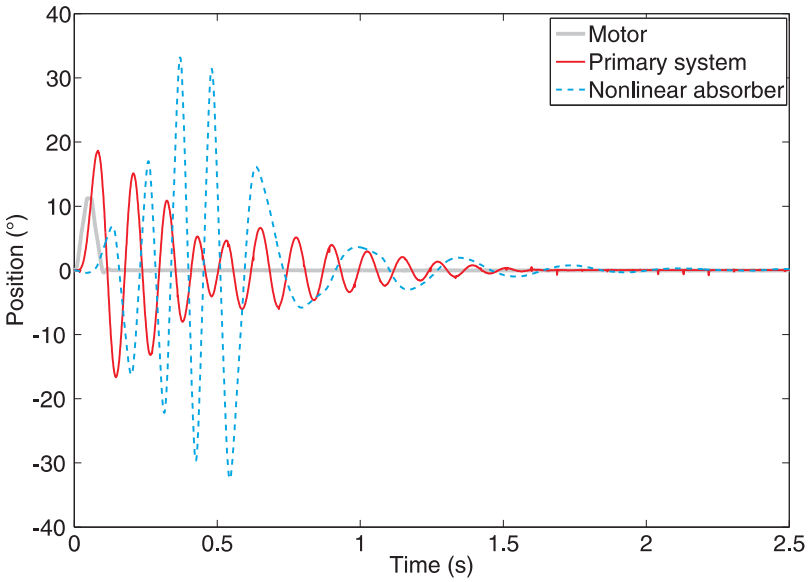

Figure 6.15: Primary system and absorber response to a motor impulse above the energy threshold

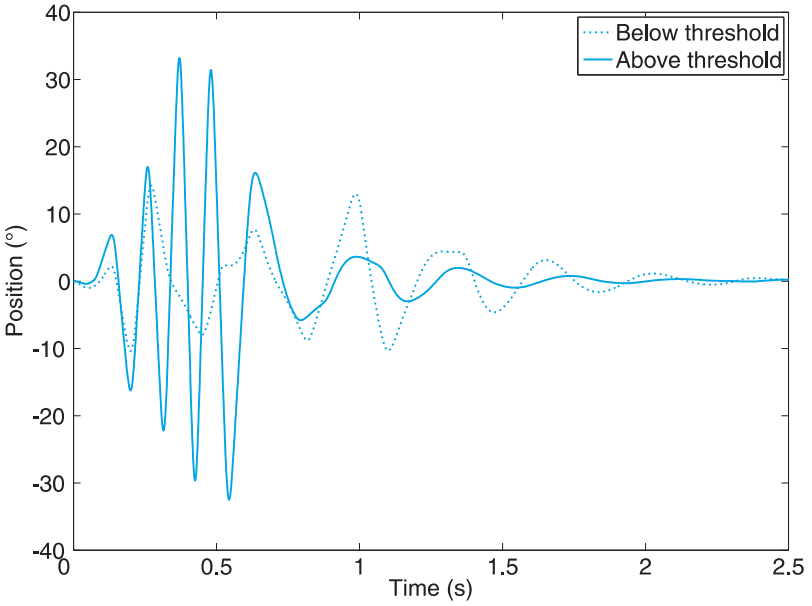

Figure 6.16: Response of the absorber below (· · ·) and above (——) the energy threshold

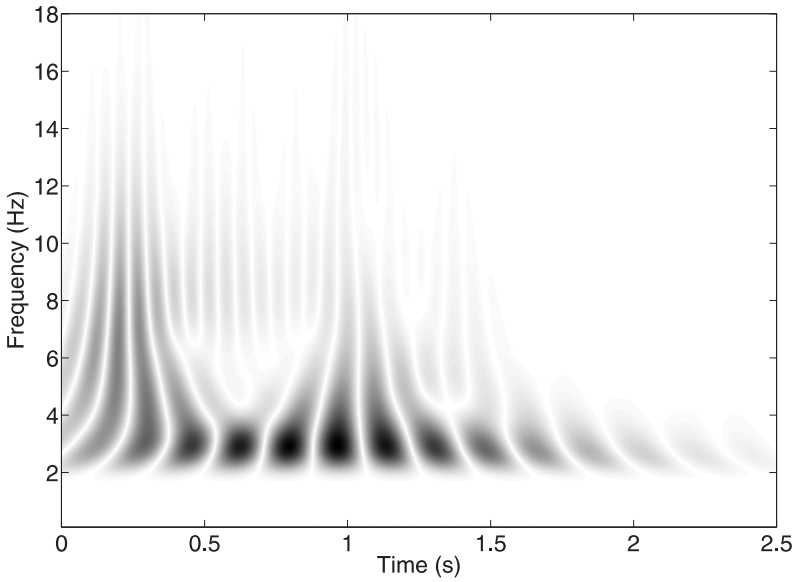

Figure 6.17: Frequency as a function of time: Wavelet transform of the absorber response below the energy threshold

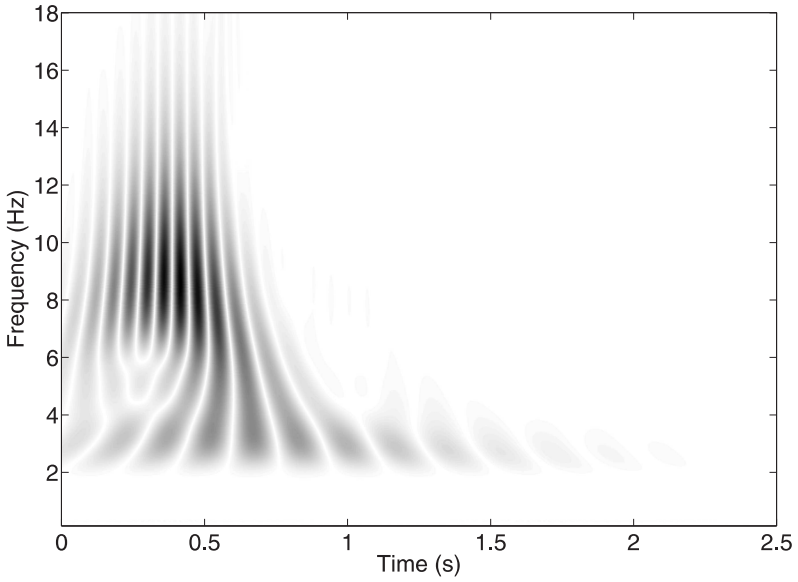

Figure 6.18: Frequency as a function of time: Wavelet transform of the absorber response above the energy threshold

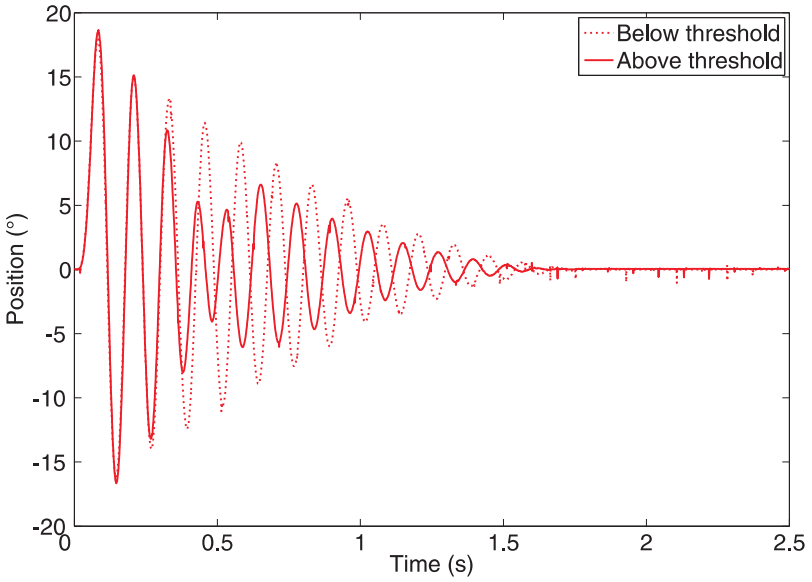

Figure 6.19: Response of the primary system below (· · ·) and above (——) the energy threshold

darker shade of gray. Below the energy threshold, the energy is mainly located at lower frequencies (around 3 Hz). Above the energy threshold however, the energy is located near the natural frequency of the primary system (around 8 Hz) demonstrating a 1:1 resonance capture.

The response of the primary system in both cases is also compared and shown in Fig. 6.19. Above the threshold, a sudden decrease of the primary system's amplitude can be seen (beating phenomenon) while almost nothing happens below the threshold.

6.5 Experiments in steady state conditions

The primary system is the same nearly SDOF system (with natural frequency ω_0) as used in the experiments for transient conditions. Only resonant conditions are studied, i.e. the motor exerts a sinusoidal excitation of frequency $\omega \approx \omega_0$ onto the primary system. As theoretically and numerically described in [46], the resulting response regimes can be strongly quasi-periodic. Here, the existence of these quasi-periodic regimes and the threshold values required to obtain them are experimentally verified. The experiments confirm the validity of the simplified analysis presented in Section 5.6 of Chapter 5.

The inertia of the absorber and the amplitude of the excitation are varied aiming

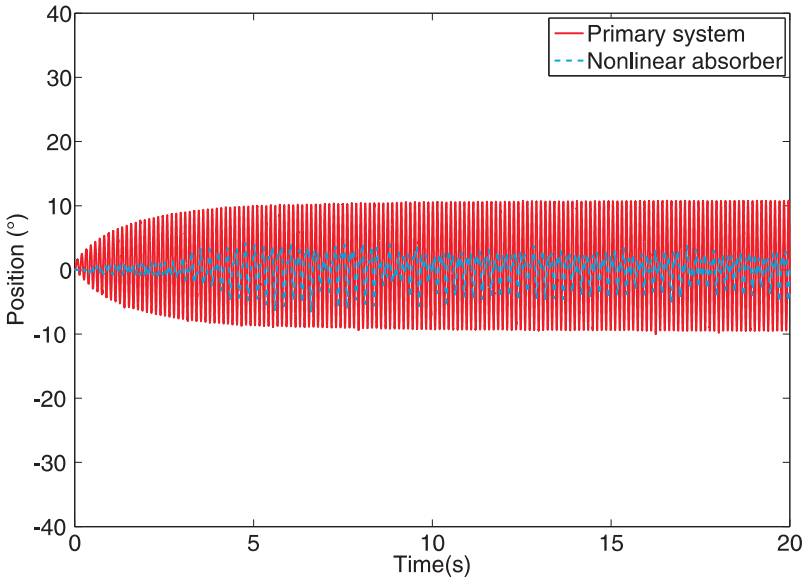

Figure 6.20: Response of the primary system and the absorber, $\Theta_1 = 1.10°$, $m_{na} = 1.7 \cdot 10^{-4}$ *kg* m^2

to determine regions with strong and weak absorber movement. Figs. 6.20 and 6.21 show the responses of the primary system and the nonlinear attachment for two different excitation amplitudes, i.e. $\theta_0(t) = \Theta_i \sin(\omega_0 t) \quad i = 1, 2$ keeping all other parameters fixed.

For $\Theta_1 = 1.10°$ (Fig. 6.20) almost no absorber movement occurs. In Fig. 6.21 a slightly larger excitation amplitude ($\Theta_2 = 1.15°$) is used, demonstrating that a region with strong absorber movement is entered. This observation enhances the validity (at least qualitatively) of extending the analysis for transient conditions to periodically forced LO as presented in Section 5.6. Indeed, Eq. (5.82) states that the excitation amplitude F (here Θ_i) should be above a certain value to obtain strong absorber movement. According to the same formula, in order to reach the threshold value, a larger absorber mass should require a larger F. This is evidenced by Fig. 6.22 where almost no absorber movement is visible for $\Theta_1 = 1.15°$ when m_{na} is increased from $1.7 \cdot 10^{-4}$ kg m^2 to $2.5 \cdot 10^{-4}$ kg m^2. Finally, keeping $m_{\text{na}} = 1.7 \cdot 10^{-4}$ kg m^2 and further increasing the excitation amplitude to $\Theta = 1.75°$ causes the beating period to decrease (Fig. 6.23). Consequently, improved vibration reduction capabilities are expected in this region of Θ.

Remark The very long buildup in Fig. 6.21 (approximately 5s or 45 periods of oscillation) before strong absorber movement suggests the existence of a homoclinic orbit living on the boundary between weak and strong absorber movement. So again,

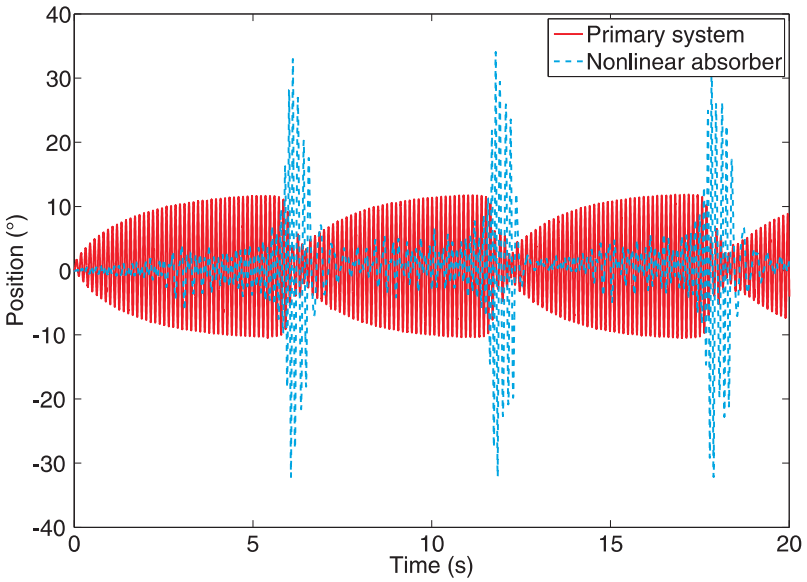

Figure 6.21: Response of the primary system and the absorber, $\Theta_1 = 1.15°$, $m_{na} = 1.7 \cdot 10^{-4}$ *kg* m^2

as explained for the LO and nonlinear attachment in transient conditions in Chapter 5, a homoclinic orbit seems to be responsible for the existence of a threshold value for the excitation amplitude $\Theta_2 \approx 1.15°$.

6.6 Conclusions and further research

This chapter described the design of a strongly SDOF nonlinear vibration absorber. A steel wire absorber, typically used in a rectilinear setting, was redesigned here for the purpose of reducing torsional vibrations. After verifying the cubic nature of its spring characteristic, experiments both in transient and in steady state conditions were performed when attached to a SDOF primary system. In both cases, we were able to observe clear boundaries between weak and strong vibration absorber movement validating in this way the theoretical analysis of Chapter 5.

Although the clamped-clamped wire design succeeds in capturing the important phenomena, its degree of nonlinearity is hard to control. To overcome this problem, a different design principle is proposed which might be the subject of future research. The idea is to use a linear spring, but to force its pathway such that it behaves like a nonlinear spring. To settle the thoughts, some guidance for the practical implementation is also given. An effective realization of the design however lies beyond the scope of this thesis.

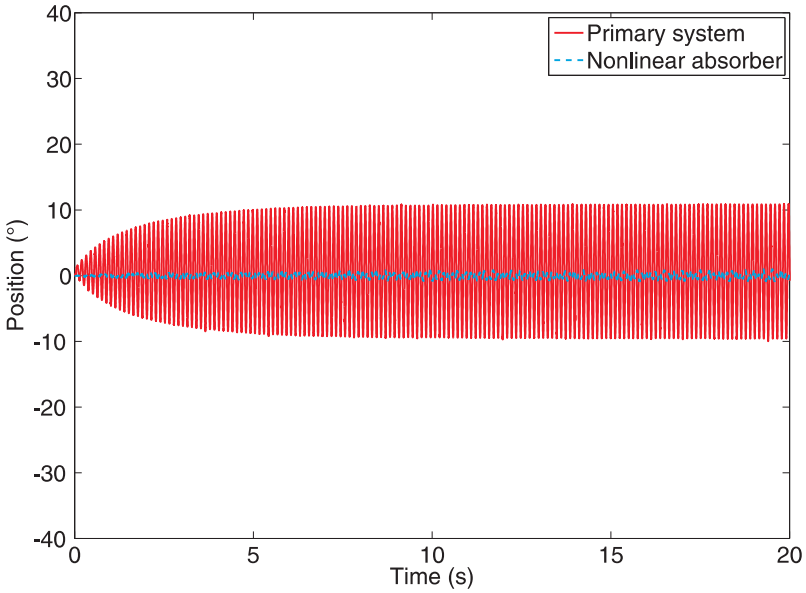

Figure 6.22: Response of the primary system and the absorber, $\Theta_1 = 1.15°$, $m_{na} = 2.5 \cdot 10^{-4}$ *kg* m^2

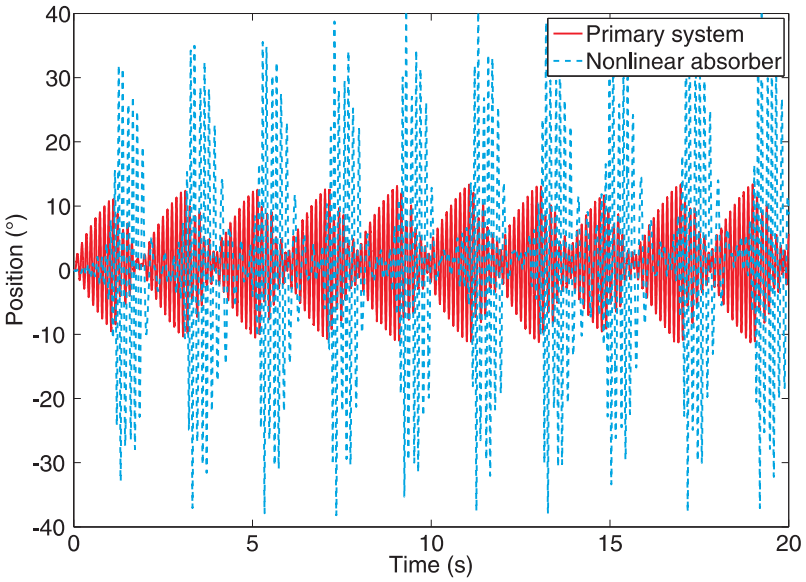

Figure 6.23: Response of the primary system and the absorber, $\Theta_1 = 1.75°$, $m_{na} = 1.7 \cdot 10^{-4}$ *kg* m^2

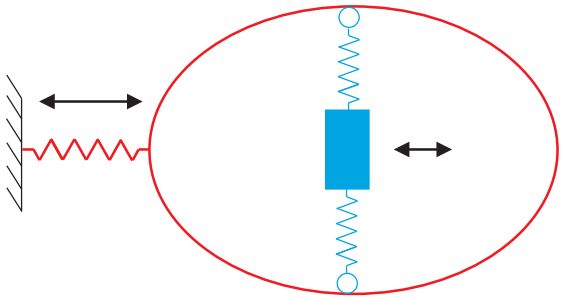

Figure 6.24: Primary system (red) and absorber (blue)

For simplicity, only rectilinear vibrations are considered in the horizontal plane which can be applied to two other experimental setups developed in the course of this PhD (Appendix 10). Both the primary system (in red) and the absorber (in blue) are shown in Fig. 6.24 and are restricted to move along a straight line (e.g. by using linear bearings). The wheels attached to the springs of the absorber are forced to move along the curved path of the primary system (e.g. by using a double roller cam follower). We further assume that the linear springs remain vertical at all times (springs are for instance guided as in a car suspension system) and that the contact between the absorber and the primary system is frictionless. We also assume that the inertia of the wheels and the springs can be neglected compared to the inertia of the central mass, i.e. the absorber behaves as a SDOF system. For a SDOF primary system, the resulting undamped equations of motion become

$$\begin{cases} m\ddot{x}_{\text{pr}} + kx_{\text{pr}} + g(x_{\text{pr}} - x_{\text{na}}) = 0 \\ m_{\text{na}}\ddot{x}_{\text{na}} + g(x_{\text{na}} - x_{\text{pr}}) = 0 \end{cases} \tag{6.35}$$

where 'pr' refers to the primary system and 'na' to the nonlinear attachment. The spring characteristic of the absorber is represented by the function g and can be determined according to Fig. 6.25. We fix the primary system to ground and determine the force F as a function of the horizontal (relative) displacement x, i.e. $F = g(x)$. Exploiting the symmetry, we can focus on the forces acting upon the lower part of the system as displayed in Fig. 6.26. The force balance becomes

$$\begin{cases} \text{Vertical} & R\cos\theta = F_s \\ \text{Horizontal} & R\sin\theta = \frac{F}{2} \end{cases} \tag{6.36}$$

Elimination of R yields

$$F = 2F_s \tan\theta \tag{6.37}$$

$$= 2kf(x)\frac{df(x)}{dx} \tag{6.38}$$

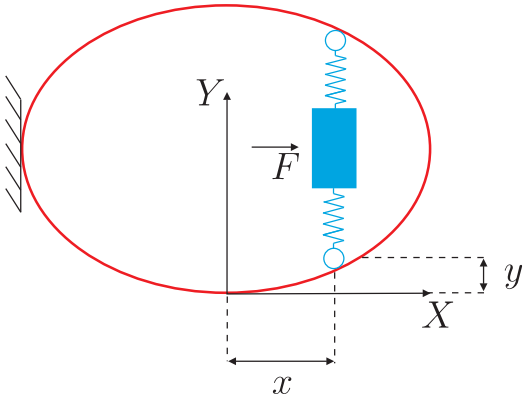

Figure 6.25: Determining $F = g(x)$ by grounding the primary system

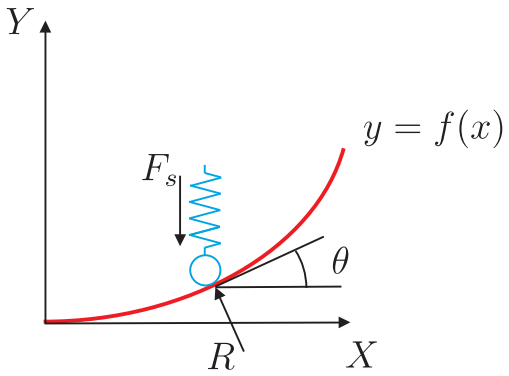

Figure 6.26: Equilibrium of forces

The desired spring characteristic depends solely on f. For instance, if a cubic nonlinear absorber is desired, f should be a quadratic function of x. The advantage of this approach is the possibility to design many different spring characteristics while the steel wire is limited to a cubic nonlinearity. Moreover, as opposed to the steel wire absorber, there are no higher order disturbances. The downside is the practical implementation which involves much more mechanical components (e.g. bearings, double roller cam follower) than the steel wire configuration where the only issue is the realization of the clamping.

Part III

Towards an industrial implementation

7

A computationally efficient selection procedure for the master degrees of freedom in condensation

7.1 Introduction

With the ever increasing dimensions of finite element method (FEM) models in vibration engineering, the field of model reduction gains more and more importance. Indeed, for the vibration control engineer, large complex FEM models are impractical. Reduced models on the other hand succeed in highlighting the dominating low-frequency behavior, crucial in a vibration control design. Moreover, a significant reduction of the computing time in both transient and steady state simulations is obtained.

A large variety of model reduction techniques exists in literature, namely Guyan reduction [47], dynamic reduction [48], CMS [49], SEREP [50], IRS [51], Krylov subspace method [52], Ritz vector technique [53], etc. Generally, these techniques involve a well-chosen coordinate transformation between the full set of coordinates and a reduced set. Depending on the type of transformation, different types of coordinates can be distinguished, e.g. physical, modal and Ritz coordinates. For a detailed comparison of the different reduction methods, see [54].

In this chapter, we restrict our study to the numerical implementation of the Guyan reduction technique, a technique which results in a reduced set of physical coordinates. Today, it is still one of the most popular methods used and implemented

in many commercial FEM software packages. It also serves as an initial approximation of more accurate dynamic condensation methods (dynamic, SEREP, IRS, CMS) where it delivers the required set of master degrees of freedom (DOFs).

When applying Guyan reduction, the full set of DOFs is divided into master and slave DOFs. The slave coordinates are eliminated such that reduced mass and stiffness matrices are obtained, which accurately model the low frequency behavior. The main challenge is to determine which slave DOFs should be eliminated or conversely, which set of masters should be retained to provide the most accurate results.

This question is addressed by [55] who developed an iterative scheme, automatically selecting the slave DOFs. In every step, one slave coordinate is selected and eliminated with Guyan reduction. Although reliable results are obtained, this sequential elimination method (SEM) becomes computationally expensive when more complex FEM models are considered (e.g. FEM models with 8-node solid elements) because the sparse mass and stiffness matrices suffer from very high fill-in in this case.

Here, a sequential selection method (SSM) is proposed, where the master DOFs are automatically selected one by one instead of the slave DOFs. Compared to SEM, the number of iterations is significantly decreased because the number of master DOFs is generally much lower than the number of slave DOFs. It is shown that the new method succeeds in reducing the storage needs and computing time when more complex FEM models are considered. For FEM models with tridiagonal matrices however the classical approach remains favorable. Unlike other sequential selection methods which are based on energy considerations [56–58], this new method relies on exactly the same principle as the one developed by [55], resulting in comparable accuracy.

After a short introduction on Guyan reduction in Section 7.2 and an overview of some of the existing SEM and SSM in Section 7.3, the new sequential selection method (SSM) is introduced in Section 7.4. A detailed comparison with the classical approach developed by [55] is presented in Sections 7.5 and 7.6.

7.2 Guyan reduction

Consider the equations of motion of an undamped model with n degrees of freedom

$$M_n \ddot{q}_n + K_n q_n = f_n \tag{7.1}$$

where M_n and $K_n \in \mathbb{R}^{n \times n}$ are the mass and stiffness matrices and $f_n \in \mathbb{R}^{n \times 1}$ is the force vector. The degrees of freedom of the full model are subdivided into master and slave degrees of freedom (subscripts m and s respectively). It is assumed that no force is applied to the slave degrees of freedom, such that Eq. (7.1) can be

rewritten as follows

$$\begin{bmatrix} M_{mm} & M_{ms} \\ M_{sm} & M_{ss} \end{bmatrix} \begin{Bmatrix} \ddot{q_m} \\ \ddot{q_s} \end{Bmatrix} + \begin{bmatrix} K_{mm} & K_{ms} \\ K_{sm} & K_{ss} \end{bmatrix} \begin{Bmatrix} q_m \\ q_s \end{Bmatrix} = \begin{Bmatrix} f_m \\ 0 \end{Bmatrix}. \tag{7.2}$$

Static reduction implies that the inertia forces of the slave degrees of freedom given in Eq. (7.2) are neglected

$$M_{sm}\ddot{q}_m + M_{ss}\ddot{q}_s = 0. \tag{7.3}$$

In this way, the slave degrees of freedom q_s can be eliminated or condensed out by considering their deformation as a static function of the deformation of the master degrees of freedom q_m

$$K_{sm}q_m + K_{ss}q_s = 0 \quad \Rightarrow q_s = S_d q_m \tag{7.4}$$

where $S_d = -K_{ss}^{-1}K_{sm}$. A reduced model can now be obtained with mass and stiffness matrices M_m, $K_m \in \mathbb{R}^{m\times m}$

$$M_m = S_f^T M_n S_f \quad K_m = S_f^T K_n S_f \tag{7.5}$$

where $m < n$ is the number of master degrees of freedom. The transformation matrix S_f describes the static transformation between the degrees of freedom of the full model and the master degrees of freedom

$$\begin{bmatrix} q_m \\ q_s \end{bmatrix} = \begin{bmatrix} I \\ -K_{ss}^{-1}K_{sm} \end{bmatrix} \{q_m\} = S_f \{q_m\}. \tag{7.6}$$

Since the slave degrees of freedom are condensed out using the static deformation, the reduced model is only correct at frequency zero. As the frequency increases, the dynamic forces become more significant, decreasing the accuracy of the reduced model.

7.3 Selection of master degrees of freedom

7.3.1 Sequential elimination method (SEM)

A crucial part of the Guyan reduction procedure lies in the choice of which and how many master degrees of freedom should be included. The most popular method is the sequential elimination method (SEM), which was originally proposed by [55] and refined by both [59] and [60]. This method starts by selecting the maximum k_{ii}/m_{ii} where k_{ii} and m_{ii} are diagonal entries of the full n by n K_n and M_n matrices. The corresponding degree of freedom is condensed out by Guyan reduction, transforming K_n and M_n into $n-1$ by $n-1$ matrices. The cycle then recommences by selecting the maximum k_{ii}/m_{ii} of the reduced K_{n-1} and M_{n-1} matrices. In

this way, the slave degrees of freedom are eliminated one by one leading to a set of master degrees of freedom. The reasoning behind this method is that a high value of k_{ii}/m_{ii} will not influence the lower frequency dynamics of interest.

The number of iterations in this procedure and hence the amount of master degrees of freedom required is addressed by [59] where a cut-off frequency ω_c is introduced which is at least three times larger than the maximum frequency of interest. The process outlined above is repeated until the maximum k_{ii}/m_{ii} is smaller than ω_c.

The main drawback of SEM is that it becomes computationally expensive when more complex FEM models are considered. This is caused by the long iteration process where the slave degrees of freedom are condensed out one by one. As the number of slave degrees of freedom is much higher than the remaining master degrees of freedom, the question arises whether it is possible to go the other way around, i.e. selecting one by one the master degrees of freedom instead of the slave degrees of freedom. As opposed to the sequential elimination method (SEM), this so called sequential selection method (SSM) severely reduces the amount of iterations required.

7.3.2 Sequential selection method (SSM)

Three different types of SSM are presented: a straightforward expansion of SEM based on the minimum value of k_{ii}/m_{ii}, a selection method based on energy considerations introduced by [56] and a new method based on the Guyan reduction technique itself which forms the main contribution and which is presented in Section 7.4.

Straightforward expansion of SEM In SEM, the degree of freedom corresponding to the maximum k_{ii}/m_{ii} is selected as a slave degree of freedom because it does not influence the lower frequency dynamics. With a similar reasoning, the degree of freedom corresponding to the minimum k_{ii}/m_{ii} could be selected as a master degree of freedom because it has a high influence on the lower frequency dynamics. Unfortunately, this proposition fails for two reasons:

1. In SEM the effect of an eliminated slave degree of freedom is redistributed to the remaining degrees of freedom by applying Guyan reduction in each iteration step as stated by [61]. As opposed to SEM, the straightforward expansion is not an iterative procedure. Consequently, the effect of selecting a master degree of freedom is not taken into account in the selection of the remaining ones, thereby reducing the accuracy of the selection procedure.

2. Consider the longitudinal vibration of the spring-mass system in the upper

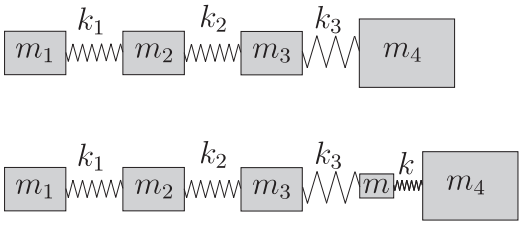

Figure 7.1: Upper: Spring mass structure with 4 DOFs; Lower: Spring mass structure with small m and large k inserted

part of Fig. 7.1. Regarding the diagonal elements k_{ii}/m_{ii} we assume that:

$$\frac{k_3}{m_4} << \frac{k_1}{m_1} \approx \frac{k_1+k_2}{m_2} \approx \frac{k_2+k_3}{m_3} \tag{7.7}$$

Clearly, m_4 should be selected as a master degree of freedom because it dominates the low frequency behavior. As the minimum k_{ii}/m_{ii} is equal to k_3/m_4, the straightforward expansion of SEM succeeds in selecting the correct master. However, when a very small mass m is added and connected to m_4 by a very large stiffness k, as shown in the lower part of Fig. 7.1, the method falls short. Indeed, k and m can be determined such that:

$$\frac{k_1}{m_1} \approx \frac{k_1+k_2}{m_2} \approx \frac{k_2+k_3}{m_3} < \frac{k}{m_4} < \frac{k+k_3}{m} \tag{7.8}$$

This means that m_1, m_2 or m_3 will be erroneously selected as masters rather than m_4. Indeed, m_4 still dominates the lower frequency dynamics because in the limit $k \to \infty$ and $m \to 0$, adding m and k does not alter the dynamics at all.

Energy based selection method This method proposed by [56] selects the master degrees of freedom based on the energy distribution matrix G:

$$G = \Phi \otimes M_n \Phi \qquad \text{or} \qquad G(i,j) = \sum_{k=1}^{n} \Phi(i,j) M_n(i,k) \Phi(k,j) \quad i = 1...n, j = 1...n \tag{7.9}$$

where $\Phi \in \mathbb{R}^{n \times n}$ is the mass normalized modal matrix and where $\otimes$ represents the cross multiplication of matrices:

$$C = A \otimes B \qquad \text{or} \qquad C(i,j) = A(i,j)B(i,j) \quad i = 1...n, j = 1...n \tag{7.10}$$

Each row of G corresponds to a degree of freedom and indicates the relative contribution of the different vibration modes to the total energy of that degree of

freedom. Each column on the other hand corresponds to a certain vibration mode, and describes how much the different degrees of freedom contribute to the total energy of that mode. Because the modal matrix Φ is mass normalized the sum of each column and the sum of each row of G are unity

$$\sum_{i=1}^{n} G(i,j) = 1 \quad j = 1...n \qquad \text{and} \qquad \sum_{j=1}^{n} G(i,j) = 1 \quad i = 1...n \tag{7.11}$$

Consequently, a partial row sum given by

$$\sum_{j=1}^{l} G(i,j) \qquad (l < n) \quad i = 1...n \tag{7.12}$$

can be used to determine the relative importance of the different degrees of freedom in the first l vibration modes. Hence, if a reduced model is required with an accurate estimate up to vibration mode l, the degrees of freedom with the highest partial row sums $\sum_{j=1}^{l} G(i,j), i = 1...n$, are selected as masters. The accuracy of each vibration mode is determined according to the energy that remains in the $n - m$ degrees of freedom that were not selected as masters

$$\sum_{i=1}^{n-m} G(i,j) \qquad (m < n) \quad j = 1...l \tag{7.13}$$

Although this energy approach has an interesting basic principle, making an accurate selection of the master degrees of freedom promising, some drawbacks have to be taken into consideration.

To determine the energy distribution matrix, the eigenvectors are required. Because these are not known a priori, Ritz vectors [53] are calculated which unfortunately tend to contain higher modes. To put more emphasis on the lower modes, a weighting factor w_j is introduced in Eq. (7.12) when selecting the masters DOFs

$$\sum_{j=1}^{l} G(i,j) w_j \qquad (l < n) \quad i = 1...n \tag{7.14}$$

$$w_j \approx 1 - \frac{\lambda_j}{\lambda_{l+1}} \quad j = 1...l \tag{7.15}$$

where λ_j is an eigenvalue of the reduced system governed by K_m and M_m. The choice of w_j is however questionable because it is based on an eigenvalue error which is assumed to be equivalent with an error in the energy distribution matrix. Further more, after selecting the master degrees of freedom by means of energy considerations, the reduced model is obtained through Guyan reduction which does not imply the same energy considerations.

Therefore, isn't it possible to select the master degrees of freedom based on the Guyan reduction principle itself? This question is answered in the next section where the main contribution is outlined: a sequential selection method (SSM) based on Guyan reduction itself.

7.4 New sequential selection method

7.4.1 The basic principle

Case 1: $M_{ms} = M_{sm} = 0$. Consider the n degree of freedom system of Eq. (7.2) with $M_{ms} = M_{sm} = 0$.

$$\begin{bmatrix} M_{mm} & 0 \\ 0 & M_{ss} \end{bmatrix} \begin{Bmatrix} \ddot{q_m} \\ \ddot{q_s} \end{Bmatrix} + \begin{bmatrix} K_{mm} & K_{ms} \\ K_{sm} & K_{ss} \end{bmatrix} \begin{Bmatrix} q_m \\ q_s \end{Bmatrix} = \begin{Bmatrix} f_m \\ 0 \end{Bmatrix} \tag{7.16}$$

According to the second part of Eq. (7.16), the slave degrees of freedom are related to the master degrees of freedom as follows:

$$M_{ss}\ddot{q_s} + K_{sm}q_m + K_{ss}q_s = 0 \tag{7.17}$$

In the frequency domain, Eq. (7.17) can be rewritten as:

$$Q_s(\omega) = -[K_{ss} - M_{ss}\omega^2]^{-1}K_{sm}Q_m(\omega) \tag{7.18}$$

where Q_s and Q_m denote the fourier transforms of q_m and q_s respectively. In Guyan reduction, the inertia forces of the slave degrees of freedom are neglected ($M_{ss}\ddot{q_s} = 0$), such that Q_s in Eq. (7.18) is estimated by $\hat{Q}_s(\omega)$ as follows:

$$\hat{Q}_s(\omega) = -[K_{ss}]^{-1}K_{sm}Q_m(\omega) \tag{7.19}$$

assuming that K_{ss} is not singular. By manipulating Eq. (7.19), the difference between Eqs. (7.18) and (7.19) can be determined in closed form:

$$\begin{aligned} \hat{Q}_s(\omega) &= -[K_{ss}]^{-1}K_{sm}Q_m(\omega) && (7.20)\\ &= -[K_{ss}]^{-1}[K_{ss} - M_{ss}\omega^2][K_{ss} - M_{ss}\omega^2]^{-1}K_{sm}Q_m(\omega) && (7.21)\\ &= -[I_s - K_{ss}^{-1}M_{ss}\omega^2][K_{ss} - M_{ss}\omega^2]^{-1}K_{sm}Q_m(\omega) && (7.22)\\ &= [I_s - \underbrace{K_{ss}^{-1}M_{ss}\omega^2}_{Error}]Q_s(\omega) && (7.23) \end{aligned}$$

with $I_s \in \mathbb{R}^{s\times s}$ the identity matrix. Equation (7.23) shows that the error between the real Q_s and the Guyan reduced $\hat{Q}_s$ is equal to $K_{ss}^{-1}M_{ss}\omega^2$. Based on this error, which is further discussed in section 7.4.2, the master degrees of freedom can be selected.

Case 2: $M_{sm} \neq 0$ and $M_{ms} \neq 0$. Equation (7.18) changes into:

$$Q_s(\omega) = -[K_{ss} - M_{ss}\omega^2]^{-1}[K_{sm} - M_{sm}\omega^2]Q_m(\omega) \tag{7.24}$$

In this case, the error introduced by Guyan reduction cannot be determined in closed form. However, assuming from now on that element-wise $|M_{sm}(i,j)\omega^2| << |K_{sm}(i,j)|$, reduces Eq. (7.24) to (7.18) such that the error can still be approximated by $K_{ss}^{-1}M_{ss}\omega^2$.

7.4.2 The error $K_{ss}^{-1}M_{ss}\omega^2$

We rewrite Eq. (7.23):

$$\hat{Q}_s(\omega) - Q_s(\omega) = -K_{ss}^{-1}M_{ss}\omega^2 Q_s(\omega). \tag{7.25}$$

The basic problem is to determine which of the slave degrees of freedom in Q_s causes the largest error when applying Guyan reduction and should consequently become a master degree of freedom. The solution is however not straightforward because this error is influenced by all slave degrees of freedom $Q_{si}, \quad i = 1 \ldots s$. Therefore, we propose an approximate selection method in which only the diagonal elements of $K_{ss}^{-1}M_{ss}\omega^2$ are considered. As also demonstrated in Section 7.6, this approach proves to be justifiable in many engineering applications.

In this case, a true relative error on component level can be determined according to Eq. (7.25):

$$\frac{\hat{Q}_{si}(\omega) - Q_{si}(\omega)}{Q_{si}(\omega)} = (K_{ss}^{-1}M_{ss}\omega^2)(i,i) \tag{7.26}$$

Consequently, the master coordinate can be selected according to the maximum diagonal element $(K_{ss}^{-1}M_{ss})(i,i)$. This result is used in the selection procedure described in Section 7.4.3.

Remarks

1. A special case of Eq. (7.26) is when only one slave degree of freedom is considered such that both K_{ss} and M_{ss} are scalars. This is exactly what happens in the classical procedure developed by [55] where the slaves are selected one by one (SEM). Indeed, for the selection of one slave degree of freedom, the minimum relative error over all possible slave degrees of

freedom is determined as follows:

$$\arg\min_i |\frac{Q_{si}(\omega) - \hat{Q}_{si}(\omega)}{Q_{si}(\omega)}| = \arg\min_i |(K_{ss}^{-1} M_{ss})(i,i)\omega^2| \tag{7.27}$$

$$= \arg\max_i |\frac{K_{ss}(i,i)}{M_{ss}\omega^2(i,i)}| \tag{7.28}$$

$$= \arg\max_i |\frac{K_{ss}(i,i)}{M_{ss}(i,i)}| \tag{7.29}$$

2. In the classical selection procedure, [59] proposed to determine the number of eliminated slaves according to ω_c, a cut-off frequency which is approximately three times larger than the largest frequency of interest ω_{max}. Slave degrees of freedom are condensed out as long as $\max_i |K_{ss}(i,i)/M_{ss}(i,i)| > \omega_c^2$. According to Eq. (7.29), this means that the maximum allowed relative error is given by:

$$|\frac{Q_{si}(\omega_{\text{max}}) - \hat{Q}_{si}(\omega_{\text{max}})}{Q_{si}(\omega_{\text{max}})}| = |\frac{M_{ss}(i,i)\omega_{\text{max}}^2}{K_{ss}(i,i)}| \tag{7.30}$$

$$< \frac{\omega_{\text{max}}^2}{\omega_c^2} = \frac{1}{9} \tag{7.31}$$

A similar approach is implemented in the selection procedure of the new sequential selection method described in Section 7.4.3. Master degrees of freedom are selected until:

$$|\frac{Q_{si}(\omega_{\text{max}}) - \hat{Q}_{si}(\omega_{\text{max}})}{Q_{si}(\omega_{\text{max}})}| = |(K_{ss}^{-1} M_{ss})(i,i)|\omega_{\text{max}}^2 \tag{7.32}$$

$$< 0.1 \tag{7.33}$$

7.4.3 Selection procedure

In a first step all the degrees of freedom are considered to be slave degrees of freedom such that the initial K_{ss} and M_{ss} are equal to K_n and M_n of the full model. The master degrees of freedom are then selected one by one according to the maximum element $|K_{ss}^{-1} M_{ss}(i,i)|$ as explained in Section 7.4.2. After each master degree of freedom selection, K_{ss} and M_{ss} are recomputed. In summary:

1. Select K_n and M_n of the full model as initial K_{ss} and M_{ss} matrices.
2. Select the degree of freedom, corresponding to the maximum element $|K_{ss}^{-1} M_{ss}(i,i)|$, as a master.
3. Reorganize K_n and M_n according to Eq. (7.2) to obtain the new K_{ss} and M_{ss} matrices.
4. Repeat steps 2 and 3 until $|(K_{ss}^{-1} M_{ss})(i,i)|\omega_{\text{max}}^2 < 0.1$

7.4.4 Systems with rigid body modes

For systems with a singular K_n matrix (systems with rigid body modes), an adapted version of the selection procedure is required because in this case K_{ss} is initially singular.

For systems with only one rigid body mode (e.g. Example 2), this problem can be circumvented by introducing a virtual master according to the maximum k_{ii}/m_{ii}, where k_{ii} and m_{ii} are diagonal entries of K_n and M_n. After reorganizing K_n and M_n according to Eq. (7.2), the first real master is determined according to the maximum $|K_{ss}^{-1}M_{ss}(i,i)|$, where K_{ss} and M_{ss} are nonsingular matrices of dimension $n-1 \times n-1$. The remaining masters are selected according to the procedure described above. For systems with multiple rigid body modes, multiple virtual masters could be introduced until K_{ss} becomes nonsingular. This is however not discussed further on.

Another way to avoid the problem of rigid body modes is by transforming M_n and K_n by elementary operations such that K_n contains as much zero rows as there are rigid body modes. Consequently, the remaining submatrix of K_n corresponds to the elastic motion of the structure and is nonsingular which means that the selection procedure can be applied on this submatrix. However, care must be taken with the outcome of this procedure as each row of the submatrices corresponds to a linear combination of the coordinates of the original system. It is therefore not clear which of the original coordinates should be selected as a master.

The most appropriate way to bypass the singularity problem is probably by applying the so called frequency shift technique [62]. In this technique, ψM_n ($\psi > 0$) is added to the original stiffness matrix K_n, changing the eigenfrequencies ω^2 of the original system into $\omega^2 + \psi$:

$$K_n\phi = \omega^2 M_n\phi \tag{7.34}$$

$$(K_n + \psi M_n)\phi = \omega^2 M_n\phi + \psi M_n\phi \tag{7.35}$$

$$K_n'\phi = \omega'^2 M_n\phi \tag{7.36}$$

with $K_n' = K_n + \psi M_n$ and $\omega'^2 = \omega^2 + \psi$. The value of ψ must be large enough to avoid numerical problems, but small enough to guarantee the accuracy of the selection procedure, i.e. $\psi << \omega_1^2$ with ω_1 the frequency of the first elastic mode.

7.5 Discussion: Classical approach vs new approach

In this section the accuracy and the computational efficiency of the classical and the new algorithm for Guyan reduction are compared. Regarding the computational efficiency both the storage requirements and the computational complexity are considered in two cases: full and sparse K_n and M_n.

7.5.1 Computational efficiency: full K_n, M_n

The computational complexity of both methods can be compared according to the number of multiplications. The classical approach involves $s = n - m$ reduction steps and the calculation of $K_m(i,i)/M_m(i,i)$ in each step. The new approach on the other hand involves m steps (instead of $n - m$) and the calculation of $K_{ss}^{-1}M_{ss}$ in each step. After this procedure, K_n and M_n are reduced in one step as opposed to the step by step reduction in the classical approach.

The required number of multiplications for the step by step Guyan reduction (without calculation of $K_m(i,i)/M_m(i,i)$ in each step) can be obtained by rewriting $K_m = S_f^T K_n S_f$ and $M_m = S_f^T M_n S_f$ as given by Eq. (7.5):

$$K_m = K_{mm} - \underbrace{K_{ms}K_{ss}^{-1}K_{sm}}_{\frac{m(m+1)}{2}+m} \tag{7.37}$$

$$M_m = M_{mm} + \underbrace{K_{ms}K_{ss}^{-1}M_{ss}K_{ss}^{-1}K_{sm}}_{\frac{m(m+1)}{2}+m+2} - \underbrace{M_{ms}K_{ss}^{-1}K_{sm} - K_{ms}K_{ss}^{-1}M_{sm}}_{m^2+m} \tag{7.38}$$

with K_{ss} and M_{ss} scalars, yielding the following total number of multiplications:

$$\sum_{p=m}^{n-1} 2p^2 + 4p + 2 \tag{7.39}$$

For the one step Guyan reduction (without the calculation of $K_{ss}^{-1}M_{ss}$ in each step), Eq. (7.5) becomes:

$$K_m = K_{mm} + \underbrace{K_{ms}S_d}_{m^2 s} \tag{7.40}$$

$$M_m = M_{mm} + \underbrace{S_d^T M_{ss} S_d}_{(s^2+s)\left(\frac{m(m+1)}{2}\right)} + \underbrace{M_{ms}S_d + S_d^T M_{sm}}_{m^2 s} \tag{7.41}$$

with $S_d \in \mathbb{R}^{s\times m}$. The calculation of $S_d = -K_{ss}^{-1}K_{sm}$ by applying Gaussian elimination requires $(s^3 - s)/3 + ms^2$ multiplications [63] and brings the total number of multiplications for this one step Guyan reduction to:

$$\frac{s^3}{3} + s^2\left(\frac{m^2}{2} + \frac{3m}{2}\right) + s\left(\frac{5m^2}{2} + \frac{m}{2} - \frac{1}{3}\right) \tag{7.42}$$

Table 7.1 presents a comparison between the multiplications required by the step by step Guyan reduction and its block form alternative given by Eqs.(7.39,7.42) respectively. For a low number of masters ($m < 10^3$) the same order of multiplications is obtained. When the number of masters increases beyond $m = 10^3$, much

n \ m	1	10	10^2	10^3	10^4	10^5
10^2	0.51	1.17	-	-	-	-
10^3	0.50	0.58	6.65	-	-	-
10^4	0.50	0.51	1.24	61.38	-	-
10^5	0.50	0.50	0.58	7.86	608	-
10^6	0.50	0.50	0.51	1.25	74	6082

Table 7.1: Ratio (A/B) between number of multiplications required in the one step Guyan reduction (A) and the step by step Guyan reduction (B) as a function of m and n

more multiplications are required when implementing Guyan reduction in block form (one step).

Besides the implementation of Guyan reduction itself, both methods also require extra calculations for the selections of the master DOFs. In the classical approach, each step involves m multiplications for calculating $K_m(i,i)/M_m(i,i)$ bringing the total number of multiplications for the entire procedure to:

$$\sum_{p=m}^{n-1} 2p^2 + 5p + 2 \tag{7.43}$$

The new approach on the other hand requires the calculation of $K_{ss}^{-1}M_{ss}$ in each step. By applying Gaussian elimination this yields for m steps:

$$\sum_{p=n-m+1}^{n} \frac{4s^3 - s}{3} \tag{7.44}$$

multiplications [63]. The total number of multiplications in the new approach is then given by adding Eq. (7.44) to Eq. (7.42).

Table 7.2 lists the ratio between the total number of multiplications required in the new and the classical approach for various values of m and n. In all cases the new approach requires more multiplications than the classical approach. The minimum ratio is approximately 2.5 and obtained for the extreme (theoretical) case where $m = 1$ and $n = 10^6$. This ratio further increases primarily as a function of m. Indeed, increasing m with a factor 10 from 10^2 to 10^3 (with $n = 10^5$ in both cases), increases the ratio with approximately a factor 10 as shown by columns 3 and 4. On the other hand, keeping m constant and changing n has a much smaller effect on the ratio as demonstrated by columns 4 and 5. In conclusion, for full K_n and M_n, it is expected that the required computing time is much larger in the new approach when a significant set of masters is considered.

	$m = 1$ $n = 10^6$	$m = 10$ $n = 10^5$	$m = 10^2$ $n = 10^5$	$m = 10^3$ $n = 10^5$	$m = 10^3$ $n = 10^4$
$\frac{\text{SSM}}{\text{SEM}}$	2.5	20.5	200.3	1978	1782

Table 7.2: Ratio between number of multiplications required in the classical vs new approach

For full K_n and M_n, the memory consumption, considered here as the number of nonzero elements, is comparable because both methods start with a system of dimension n which is reduced by one after each iteration step (K_{mm}, M_{mm} in the classical approach versus K_{ss}, M_{ss} in the new approach).

7.5.2 Computational efficiency: sparse K_n, M_n

In the above, K_n and M_n were considered to be full while in practice they are sparse. Consequently, the number of multiplications and the storage requirements are drastically reduced. It seems reasonable to expect that the sparsity of K_n and M_n will not change the above derived conclusions regarding computing time and memory, i.e. the computing time required in the new approach still exceeds by far that of the classical approach while the storage needs are equivalent for both methods. For elementary FEM models (e.g. tridiagonal systems) this is indeed correct. However, for more complex FEM models, every step of the classical approach creates new nonzero elements in the initially sparse mass and stiffness matrices (so called fill-in), driving this procedure computationally expensive as shown hereafter.

Consider Eq. (7.37) of the classical approach on a component level:

$$K_m(i,j) = K_{mm}(i,j) - \frac{K_{ms}(i)K_{sm}(j)}{K_{ss}} \quad i,j = 1,..,m \tag{7.45}$$

If the coupling between elements i and j is zero prior to a reduction step ($K_{mm}(i,j) = 0$), Eq. (7.45) shows that a new nonzero element is created after the reduction step ($K_m(i,j) \neq 0$) when both master coordinates i and j are coupled with the slave coordinate ($K_{ms}(i) \neq 0, K_{sm}(j) \neq 0$). The same conclusion holds for $M_m(i,j)$ derived from Eq. (7.38):

$$M_m(i,j) = M_{mm}(i,j) + M_{ss}\frac{K_{ms}(i)K_{sm}(j)}{K_{ss}^2} - \frac{[M_{ms}(i)K_{sm}(j) + K_{ms}(i)M_{sm}(j)]}{K_{ss}} \tag{7.46}$$

In the simplest case, i.e. K_m tridiagonal and M_m diagonal ($m = n$ initially), each reduction step creates two extra nonzero elements in K_m and M_m according to Eqs. (7.45-7.46). As every reduction step reduces the size of K_m and M_m with one,

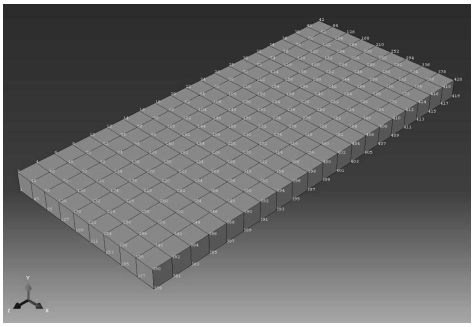

Figure 7.2: FEM of a plate with 420 nodes and 1260 DOFs

this results in three less nonzero elements for K_m and one extra nonzero element for M_n. In the end, both matrices are tridiagonal such that the classical approach remains favorable. However, when the FEM becomes more complex, the higher number of couplings between the elements drastically increases the number of nonzero elements in each reduction step as shown in the following example.

Consider a FEM model of a plate shown in Fig. 7.2, consisting of 180 hexahedral elements (8-node solid elements) yielding 420 nodes with three DOFs each, resulting in a total of 1260 DOFs. The first slave DOF in the classical algorithm is coupled with 31 DOFs from which each element is only coupled with half of the other elements. After one iteration this results in 425 nonzero elements extra. After 300 iterations, the initial density of K_n and M_n, 3% and 0.08% respectively, has increased for both matrices to 92%, amplifying the initial number of nonzero elements with a factor 18 and 672 respectively. For very large mechanical systems it is clear that besides increased storage needs this fill-in also substantially augments the required number of computations.

In the new approach Guyan reduction is performed in one step preventing in this way the above discussed fill-in problem. Consequently, for complex sparse mechanical systems the one step Guyan reduction used in the new algorithm is far less computationally demanding than its step by step alternative. The new approach however also requires the calculation of $K_{ss}^{-1}M_{ss}$ in each step which is equivalent to solving following linear system:

$$K_{ss}X = M_{ss} \tag{7.47}$$

The question arises whether the advantage of avoiding fill-in in the new approach remains after calculating Eq. (7.47).

A vast amount of books and papers have been dedicated to the numerical implementation of Eq. (7.47), see for instance [64, 65] and the references therein. The numerical techniques can be divided into two categories: direct and iterative.

The main disadvantage of the direct solvers (e.g. LU, Choleskey factorization) is fill-in in the factorization step thereby increasing the computing time and the memory consumption. While the fill-in caused by the step by step Guyan reduction procedure is independent of the ordering of the DOFs, different re-ordering techniques exist to minimize the fill-in caused by factorization. Despite these advances, there is a tendency to prefer iterative methods when dealing with large mechanical structures. One of the most popular iterative techniques is the conjugant gradient (CG) method generally combined with a preconditioner to speed up the convergence. A detailed comparison between iterative and direct solvers is given in [64] where it is shown that iterative solvers can provide advantages in both storage and computation time especially when 8-node hexahedral elements are considered.

It is not possible to derive general conclusions regarding the computational efficiency of solving Eq. (7.47) because this highly depends on the solver and the sparsity pattern of K_n and M_n [64]. To give some idea, we apply a direct solver (LU factorization without reordering) on the plate given in Fig. 7.2. The number of nonzero elements after factorization is only 6.6 times higher than initially and can be further reduced to 3.3 by reordering. Compared to the number of nonzero elements after 300 iterations in the step by step Guyan reduction procedure, this is approximately a factor 10 lower. Besides this decreased storage need, the new approach also results in a factor 10 lower in computing time which can be even further reduced by applying iterative solvers.

7.5.3 Accuracy

Applying Guyan reduction in each iteration step ensures that the effect of a condensed slave is redistributed over the remaining degrees of freedom. This is a crucial feature of the classical selection procedure which significantly increases the accuracy compared to the case where the slave DOFs are all selected at once. This redistribution is also achieved in the new approach by redefining K_{ss} and M_{ss} in each step, thereby taking into account the previously determined master DOFs.

Furthermore, both methods are based on Eq. (7.26), which is derived from the Guyan reduction procedure itself. As demonstrated by the examples in Section 7.6, this results in a comparable accuracy.

7.6 Examples

7.6.1 A uniform structure: cantilever beam

Table 7.3 presents the natural frequencies of a cantilever beam [63], limited to transversal vibrations in the vertical direction as displayed in Fig. 7.3. The beam is Guyan reduced from 5000 to 20 DOFs with both the classical and the new approach. The corresponding master degrees of freedom are listed in Table 7.4 showing that

Mode No.	SSM	SEM	SEM in one step	Theory
1	405.99	398.40	406.08	397.87
2	2494.8	2493.5	2494.8	2493.2
3	6982.4	6981.9	6982.4	6982.2
4	13683	13683	13683	13681
5	22622	22626	22626	22616
6	33813	33828	33818	33784
7	47282	47273	47273	47187
8	62986	63030	63030	62823
9	81112	81216	81216	80692
10	101982	101271	101271	100796

Table 7.3: Natural frequencies (in Hz) of a cantilever beam calculated with the classical SEM and the new SSM. Length: 20 mm, width: 2 mm, thickness: 0.2 mm, E-modulus: 19010^3 *N/mm*^{2}*, density:* 7.8310^{-6} *kg/mm*^{3}

	1	2	3	4	5	6	7	8	9	10
SSM	4999	2929	1615	4055	890	2285	3506	4571	491	1261
SEM	3788	4976	1770	2898	882	4520	2358	1394	3482	490
	11	12	13	14	15	16	17	18	19	20
SSM	1959	2615	3225	3788	4320	4805	271	695	1081	1787
SEM	4202	2026	3106	1138	2562	4789	272	3982	746	1594

Table 7.4: Set of master DOFs of the new SSM and the classical SEM

both methods yield a completely different set of masters. Despite this distinction, the resulting natural frequencies shown in Table 7.3 are quite similar, except for the lowest natural frequency where a difference of 2% is noticeable. Interestingly, this exception is not caused by the difference in the master's set. It stems from applying Guyan reduction in each iteration step, whereas in the new approach the slave DOFs are condensed out all at once. Indeed, when the beam is Guyan reduced in one step according to the master's set of the classical approach, the anomaly in the lowest frequency between SSM and SEM (in one step) disappears as shown in Table 7.3.

7.6.2 A nonuniform structure: dredger drive line

In the previous example, a uniform structure was studied that resulted in a completely different set of master DOFs for the new and the classical approach. The

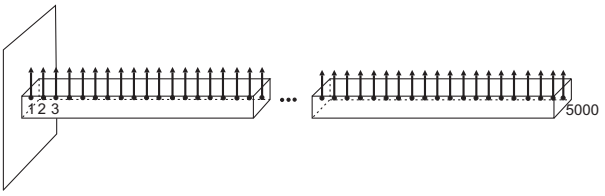

Figure 7.3: Vertical vibration of a cantilever beam with 5000 DOFs

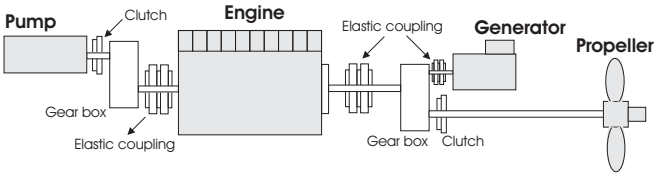

Figure 7.4: The drive line of a hopper dredger

next example is a nonuniform example to prove that in this case both methods do end up with the same master DOFs selection.

Figure 7.4 shows a possible layout of the drive line of a hopper dredger. Typically, the drive line of a such a ship consists of a centrifugal pump, a propeller and a generator which are all driven by a diesel engine. These main elements are connected with each other through flexible couplings, clutches, gear boxes and shafts. When limited to torsional vibrations, the continuous drive line is generally modelled as a lumped parameter model according to methods explained in [66]. Figure 7.5 shows an example of such a lumped parameter model with 39 DOFs. All inertias are connected with each other through torsional springs. The flexible couplings are emphasized in the figure because they feature a much lower torsional stiffness. The highest inertia is localized at DOF 26 and the part with the lowest stiffness lies in between DOFs 28-29 and 29-30. In proportion to these, the stiffness and inertia of the remaining parts are listed in Table 7.5 providing the degree of nonuniformity of the structure.

Inertia	1	0.81	0.60	0.54	< 0.2
at DOF	26	3	39	35	other
Stiffness	1	2.11	2.12	2.24	> 5
Between DOFs	28-29-30	11-12-13-14	23-24-25	38-39	other

Table 7.5: Inertia and stiffness in proportion to highest inertia and lowest stiffness

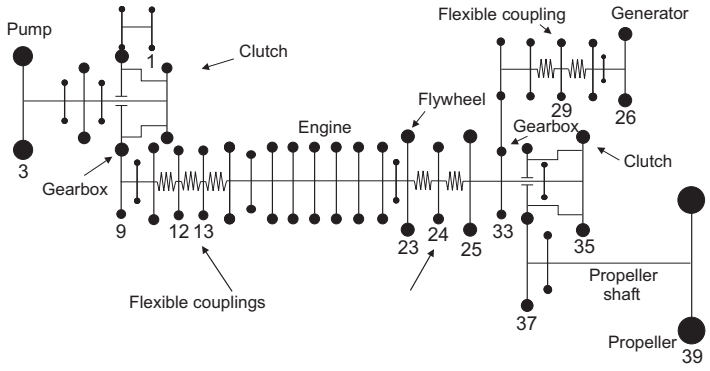

Figure 7.5: A lumped parameter model of the torsional vibrations of the drive line

	1	2	3	4	5	6	7	8	9	10
SSM	3	26	39	23	35	9	12	13	29	24
SEM	23	26	3	35	39	9	12	13	29	24

Table 7.6: The first 10 master DOFs for the new SSM and the classical SEM

Table 7.6 shows that the classical and the new algorithm end up with the same set of 10 master DOFs, although the order of selection varies for the first 5 masters. For a reduced model of 10 masters both methods yield the same natural frequencies. If only the 4 first masters (Table 7.6) are retained in the reduced model, the difference in the master's set causes the natural frequencies to differ, as shown in Table 7.7. The new approach ends up with the flywheel and the end rotors (generator, pump and propeller) as masters, while the classical approach selects DOF 35 (a clutch) instead of 39 (the propeller). Both methods yield almost the same natural frequencies except for vibration mode 4 where the new SSM reaches a 1% lower value than SEM. As opposed to the Example 1, there is no difference between SEM and SEM in one step.

7.6.3 A FEM with hexahedral elements: plate

In section 7.5 we already studied the example of a plate modelled with 8-node hexahedral elements or solid elements. The plate is Guyan reduced from 1260 to 20 DOFs. Table 7.8 shows that again comparable results are obtained although in the new approach a slightly better approximation of the lower elastic modes is achieved.

Mode No.	SSM	SEM	SEM in one step	Unreduced
1	0	0	0	0
2	1.6266	1.6245	1.6245	1.6096
3	2.5288	2.5235	2.5235	2.4916
4	3.6026	3.6587	3.6587	3.4738

Table 7.7: Comparing the natural frequencies for a reduced model of 4 masters

Mode No.	SSM	SEM	Theory
1	136.3	136.4	136.1
2	254.5	255.1	253.5
3	372.8	376.0	367.9
4	531.8	541.7	520.1
5	650.3	656.6	621.6

Table 7.8: First elastic modes (in Hz) of a plate modelled with 8-node solid elements

7.7 Conclusion

The classical algorithm for Guyan reduction developed by [55] leads to very high fill-in when complex FEM models (e.g. with 8-node solid elements) are considered. As a result, the computing time and required storage needs are substantially increased. To overcome this problem, a new method is proposed where the master DOFs are sequentially selected instead of the slave DOFs drastically reducing in this way the required number of iterations.

It is shown that the classical as well as the new selection procedure are based on the same measure $|K_{ss}^{-1} M_{ss}|$, which denotes the relative error introduced by selecting a certain DOF as a slave. Consequently, a comparable accuracy of the reduced models is obtained.

Furthermore, an alternative approach based on the frequency shift technique is proposed for systems with rigid body modes because K_{ss} is singular in this case.

8

Vibration absorbers attached to the drive line of a hopper dredger

8.1 Introduction

As the activities of dredger ships are increasing throughout the world, their durability and maintenance is receiving considerable attention. However, the drive line of a dredger still suffers from early damage at vital components like elastic couplings and gear boxes which connect the dredger's main equipment, namely the propeller, the generator, the diesel engine and the pump. This early damage is primarily caused by excessive torsional vibrations that originate from both steady state and transient behavior.

Regarding steady state torsional vibrations, the main excitation source is the irregular driving torque of the diesel engine. In a worst case scenario, this input torque would resonate with the mass-elastic propulsion system leading to unacceptable levels of internal stresses and in some cases even shaft failure. To prevent such shortcomings, classification societies require extensive torsional vibration calculations (TVC) of the ship before commissioning. A TVC-analysis is usually carried out by the manufacturer of the diesel engine which gathers the necessary technical information from the different suppliers of the other drive line components. Using this information, the drive line of the ship (a damped mass-elastic system) is modelled as a lumped parameter model as described in [66]. When the stresses arising from the varying torques of the diesel engine and the propeller meet the requirements of the classification societies, the ship can be put into operation.

Vibrations due to transient conditions on the other hand are generally not taken into account in a TVC-analysis. Transient loads involve among others starting/stopping the engine, engaging/disengaging clutches and altering the vessel's speed and are known to be a source of severe damage to couplings and gear boxes. They can also induce unstable interaction between the speed governor and the mass-elastic system known as governor instability [67, 68], which further enhances their importance.

In this chapter we focus on the transient loads as they cause a multimodal response, i.e. different vibration modes are excited, which calls for the application of a strongly nonlinear absorber. As an example, we consider an impulsive load at the propeller as described in Section 8.3. The goal is to reduce the vibration amplitudes at the propeller gearbox by attaching to it a vibration absorber. Two types are considered, namely the classical linear vibration absorber and a strongly nonlinear one with cubic nonlinearity. As explained in Section 8.4, the parameters of both absorbers are tuned according to SDOF methods, i.e. they are tuned to the vibration mode that dominates the multimodal response. In Section 8.5, the feasibility of the nonlinear absorber to sequentially dissipate energy from different vibration modes is studied. The resulting vibration reduction through these so called resonance capture cascades [13] is compared to the reduction achieved by the classical linear absorber. First, a general introduction to the drive line of a hopper dredger is presented in Section 8.2.

8.2 A trailing suction hopper dredger

A hopper dredger has become an indispensable ship in the maritime world [69]. It is mainly used to deepen waterways (harbors, rivers) in order to keep them navigable. However, the most well-known use is probably land reclamation which is gaining more and more interest.

8.2.1 Layout of a dredger

Figure 8.1 shows a possible layout of the drive line of a hopper dredger. In most cases a hopper dredger contains two such drive lines working independently of each other, one at the port side and one at the starboard side.
The main tool of a hopper dredger is a centrifugal pump. This pump sucks up mud through a trailing suction pipe and collects it in the hopper. The propeller is considered to be a controllable pitch propeller (CPP). This enables the diesel engine to run at a constant speed. Hence, the engine can drive the pump and the generator as well. Further more, by adjusting the pitch of the propeller, the diesel engine can deliver its full power in different operating conditions which is an important advantage. The generator requires an output frequency in between $50Hz$ and $60Hz$

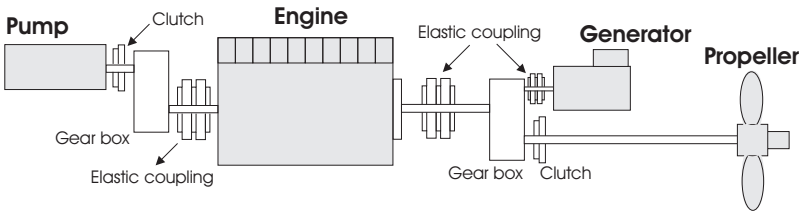

Figure 8.1: Outline of a hopper dredger

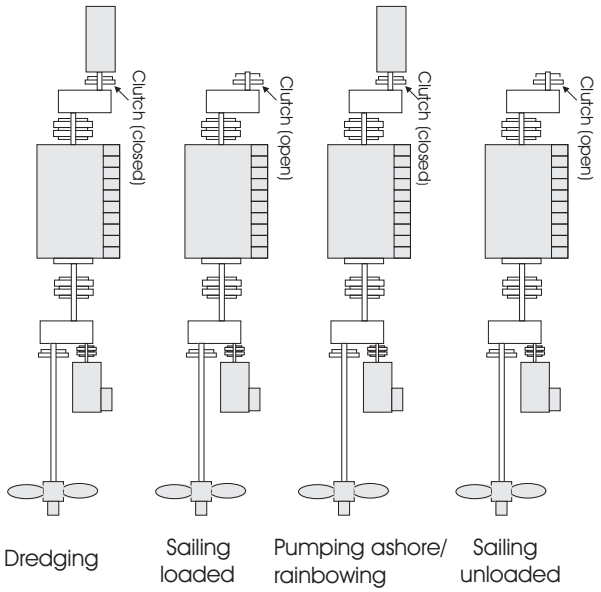

Figure 8.2: Dredge cycle of a hopper dredger

which limits the speed interval of the diesel engine. The main components (engine, pump, generator and propeller) are connected through gear boxes and flexible couplings. Clutches can be engaged and disengaged to allow a change of the drive line's configuration, i.e. the pump and the propeller can be connected and disconnected.

8.2.2 Dredge cycle

A working cycle of a dredger comprises four parts (Fig. 8.2). First sand or mud is pumped up and stored in the hopper (dredging). Then the ship sails towards the place of discharge (sailing loaded). Discharging the ship can be done in several ways: by opening the bottom doors of the hopper (sailing configuration), by pressing

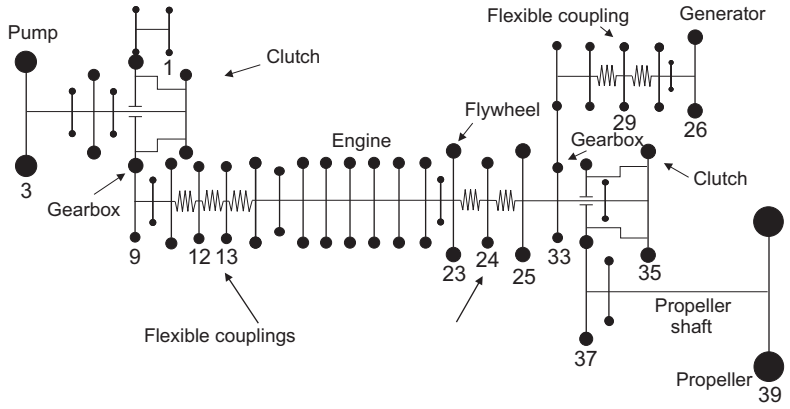

Figure 8.3: Lumped parameter model of the mass-elastic system

the load ashore through pipes, or by rainbowing the load close to the ship by means of a nozzle (pumping ashore/rainbowing). Finally the ship sails back unloaded (sailing unloaded) and the cycle recommences. A full cycle can take from a couple of hours up to a couple of days depending on the type of mixture and the distance between the places of charge and discharge. Each of the steps in the cycle requires a different configuration of the drive line. It is clear that the transient conditions are worth examining.

8.2.3 Sources of vibration

The main sources of vibration taken into account in the TVC-analysis, are the irregular driving torque of the diesel engine and the excitation generated by the propeller. While these periodic excitations definitely take priority in a vibration analysis, this chapter is limited to transient loads (e.g. start-up, engaging and disengaging clutches), as they have shown to be a source of severe damage to couplings and gear boxes. The most important sudden load changes are initiated by engaging and disengaging the propeller and pump clutches, by changing the load on the generator and by altering the speed of the diesel engine. Interestingly, they all occur at different places on the drive line. As a result, different vibration modes are excited, again supporting the usefulness of a nonlinear absorber.

8.2.4 A reduced model of the hopper dredger drive line

In the obliged TVC-analysis, the continuous drive line shown in Fig. 8.1 is modeled as a lumped parameter model according to methods explained in [66]. However, in practice this model still contains up to 50 degrees of freedom (Fig. 8.3) which, from the point of view of a vibration control engineer, is far too complex. Therefore,

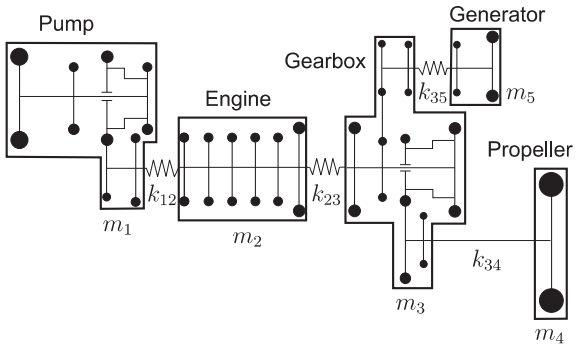

Figure 8.4: Guyan reduced model with 5 DOFs

Parameter	Value
m_1	3.1 $\cdot 10^3$ kg m^2
m_2	3.3 $\cdot 10^3$ kg m^2
m_3	1.8 $\cdot 10^3$ kg m^2
m_4	0.9 $\cdot 10^3$ kg m^2
m_5	1.7 $\cdot 10^3$ kg m^2
k_{12}	0.4 $\cdot 10^6$ Nm/rad
k_{23}	0.6 $\cdot 10^6$ Nm/rad
k_{34}	1.3 $\cdot 10^6$ Nm/rad
k_{35}	0.3 $\cdot 10^6$ Nm/rad

Table 8.1: Mass and stiffness values of the Guyan reduced model displayed in Fig. 8.4

the Guyan reduction procedure of the previous chapter is applied retaining only 5 master DOFs. The numerical mass and stiffness values (reduced to the diesel engine's speed) are listed in Table 8.1, a graphical representation is given in Fig. 8.4. The eigenfrequencies ω_i (with $\omega_1 = 0$) and the corresponding mass matrix normalized eigenvectors e_i of the reduced model are presented in Table 8.2. The percentage error between the eigenfrequencies of the original and the reduced model is shown to be well below the engineering 5%.

8.3 Transient vibrations due to impulsive loads

8.3.1 Problem statement

We consider the transient vibrations of the undamped mass-elastic drive line of Fig. 8.4 when it is excited by an impulsive load at the propeller. The objective is to protect the propeller gearbox from troublesome torsional vibrations by attaching a

	e_1	e_2	e_3	e_4	e_5
1. Pump	0.0096	-0.0121	0.0086	-0.0041	-0.0001
2. Diesel	0.0096	-0.0021	-0.0083	0.0115	0.0015
3. Gear box	0.0096	0.0058	-0.0076	-0.0104	-0.0159
4. Propeller	0.0096	0.0063	-0.0094	-0.0166	0.0234
5. Generator	0.0096	0.0162	0.0146	0.0053	0.0013
ω_i (rad/s)	0	10.42	16.06	22.42	47.34
$\omega_i/(2\pi)$ (Hz)	0	1.66	2.56	3.57	7.53
Error (%)	0	3.15	2.84	3.38	3.32

Table 8.2: Modal parameters

vibration absorber. The performance of the classical linear absorber is compared with that of a cubic nonlinear one. Both absorbers are attached to the propeller gearbox with absorber inertia 200 kg m^2 which is approximately 10 $\%$ of the gearbox inertia m_3.

For simplicity, the impulsive load is modelled as an initial velocity of 1 rad/s. Fig. 8.5 shows the corresponding response at the propeller gearbox which demonstrates that we are dealing with a multimodal response, i.e. multiple vibration modes contribute to the response. The corresponding frequency content (positive side of the amplitude spectrum obtained with fft) shows the presence of two dominant modes (modes $4 = 3.57$ Hz and $5 = 7.53$ Hz) while modes 2 (1.66 Hz) and 3 (2.55 Hz) are less important.

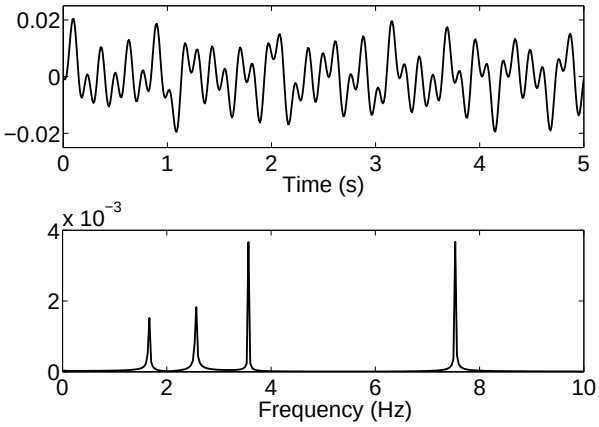

Figure 8.5: Multimodal response at the propeller gearbox without absorber (rigid body mode (0 Hz) is discarded

Tuning both absorbers to the multi-frequency response of Fig. 8.5 is not straightforward. We first apply the methods developed for SDOF systems by isolating the contribution of a single vibration mode. Isolating a single vibration mode can be achieved by using modal analysis [19] as discussed in the next section.

8.3.2 Energy within each vibration mode

Modal analysis shows that the response of the drive line to an initial velocity of the propeller can be decoupled as follows

$$q(t) = \dot{p}_1(0)e_1 t + \sum_{i=2}^{5} \frac{\dot{p}_i(0)e_i}{\omega_i} \sin \omega_i t \tag{8.1}$$

revealing the contribution of the different vibration modes. In (8.1), p_i is the i^{th} component of the vector of principal coordinates p with

$$q = Ep \tag{8.2}$$

$$= \sum_{i=1}^{n} e_i p_i \tag{8.3}$$

where $E = [e_1 e_2 \cdots e_n] \in (R^{n \times n})$ is the mass matrix normalized modal matrix. The initial conditions $p_i(0)$ (zero in our case) and $\dot{p}_i(0)$ can be determined as a function of $q(0)$ and $\dot{q}(0)$ from Eq. (8.2)

$$p(0) = E^{-1}q(0) \qquad \dot{p}(0) = E^{-1}\dot{q}(0). \tag{8.4}$$

$\dot{p}_i(0)$	Value (rad/s)
$\dot{p}_1(0)$	9.19
$\dot{p}_2(0)$	6.08
$\dot{p}_3(0)$	-9.01
$\dot{p}_4(0)$	-15.93
$\dot{p}_5(0)$	22.39

Table 8.3: Initial conditions $p_i(0)$ corresponding to an initial velocity of 1 rad/s at the propeller

and are listed in Table 8.3.

Equation (8.1) shows that an initial velocity of 1 rad/s at the propeller corresponds to an initial velocity of $\dot{p}_i(0)e_i$ for the different vibration modes. To isolate the contribution of a single vibration mode i, thereby achieving a unimodal response, we need to simulate the 5DOF system with initial conditions proportional to the corresponding eigenvector e_i (Table 8.2), i.e.

$$q(0) = 0 \quad \text{and} \quad \dot{q}(0) = \dot{p}_i(0)e_i \tag{8.5}$$

8.4 Tuning procedure in the unimodal case

As the attachment location (propeller gearbox) and the absorber mass m_a (200 kg m^2) are chosen a priori, only the stiffness and damping parameters of the absorber are left to be determined. Since we are dealing with a multi-frequency response (Fig. 8.5), this is not a straightforward task. We therefore choose to tune them to the most dominant vibration mode, such that we can rely on SDOF methods. Since there are two dominant modes (modes 4 and 5), both will be considered.

8.4.1 Linear absorber

In [5], an optimization procedure is described for the linear absorber attached to a SDOF linear undamped primary system (with natural frequency ω_0) subject to initial conditions. The absorber mass m_a is chosen a priori, while k_a and c_a are determined such that the decay rate is maximized. This is achieved by equalizing the negative real part of the poles and putting them as far as possible to the left hand side of the imaginary axis. The resulting optimal absorber parameters become

$$\omega_a \triangleq \frac{k_a}{m_a} = \frac{\omega_0}{1+\mu} \tag{8.6}$$

$$\zeta_a = \frac{c_a}{2m_a\omega_a} \leq \sqrt{\frac{\mu}{1+\mu}} \tag{8.7}$$

	mode 4	mode 5
m_a	200 kg m^2	200 kg m^2
k_a	9.63 $\cdot 10^4$ Nm/rad	4.06 $\cdot 10^5$ Nm/rad
c_a	$< 1.28 \cdot 10^3$ Nms/rad	$< 3.96 \cdot 10^3$ Nms/rad
μ	0.022	0.051

Table 8.4: Linear absorber parameters when tuned to vibration mode 4 and 5

where μ is defined as the absorber inertia m_a relative to the inertia of the main system. For MDOF systems featuring multiple natural frequencies, μ can be re-defined as the absorber inertia relative to the modal inertia $\frac{1}{e_i(j)^2}$ of mode i at the attachment location j [70]

$$\mu = \frac{m_a}{\frac{1}{e_i(j)^2}} \tag{8.8}$$

$$= m_a e_i(j)^2 \tag{8.9}$$

with in our case $j = 3$ (propeller gearbox). The absorber parameters when tuned to vibration mode 4 and 5 are listed in Table 8.4 where a maximum value is defined for c_a. For this maximum, which denotes the optimum for infinite times, no beating occurs. By decreasing c_a, thereby allowing beating, a faster reduction to a given amplitude can be obtained within a finite time. This is illustrated in Fig. 8.6 for vibration modes 4 and 5. Regarding vibration mode 4, a value $c_a = 250$ Nms/rad results in a vibration reduction to less than 50% of the value attained without absorber ($7.6 \cdot 10^{-3}$ rad) within 3 periods of vibration. For mode 5, a reduction to less than 20 $\%$ is achieved in less than three periods (after 0.31 s) for $c_a = 1600$ Nms/rad.

Remark The difference in vibration reduction between modes 4 and 5 is caused by the larger value of μ for vibration mode 5 ($\mu = 0.051$) compared to that of mode 4 ($\mu = 0.022$).

8.4.2 Cubic spring absorber

The nonlinear absorber can be tuned according to (5.60) of Chapter 5, repeated here for convenience

$$\gamma = \frac{k_{\text{na}}}{m_{\text{na}}} \frac{(x(0)^2\omega_0^2 + \dot{x}(0)^2)}{\omega_0^4} > \gamma_c \approx 0.18 \tag{8.10}$$

As discussed in Section 8.3.2, we need to replace $\dot{x}(0)$ with $\dot{p}_i(0)e_i(3), i = 4, 5$, keeping $x(0) = 0$. Applied to vibration modes 4 and 5, the threshold value k_{na} for

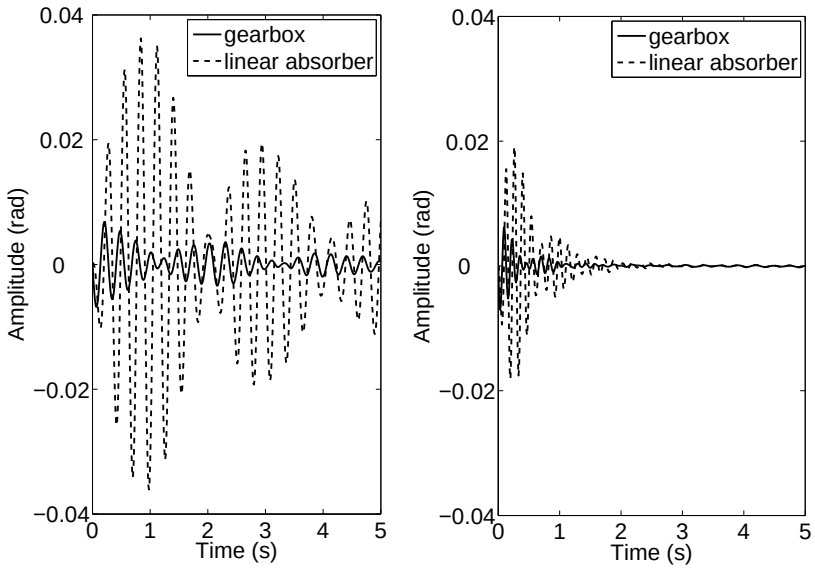

Figure 8.6: Gearbox and linear absorber response for unimodal vibration; Left: Mode 4; Right Mode 5

	mode 4	mode 5
m_{na}	200 kg m^2	200 kg m^2
k_{na}	4.30 $\cdot 10^8$ Nm/rad	2.5 $\cdot 10^9$ Nm/rad
c_{na}	550 Nms/rad	1600 Nms/rad

Table 8.5: Nonlinear absorber parameters when tuned to vibration mode 4 and 5

the undamped absorber becomes

$$k_{\text{na}} \geq \frac{0.18 m_{\text{na}} \omega_4^4}{(\dot{p}_4(0) e_4(3))^2} = 3.31 \cdot 10^8 \text{Nm/rad} \tag{8.11}$$

$$k_{\text{na}} \geq \frac{0.18 m_{\text{na}} \omega_5^4}{(\dot{p}_5(0) e_5(3))^2} = 1.43 \cdot 10^9 \text{Nm/rad} \tag{8.12}$$

For a damped cubic spring absorber, this threshold value is larger. Similar to the case of the linear absorber, we allow a beating response to obtain a fast reduction to a given amplitude. The absorber parameter values used in the simulations are listed in Table 8.5. The corresponding response is shown in Fig. 8.7. For vibration mode 4, almost 4 periods are required to achieve a 50 $\%$ reduction (instead of less than 3 periods for the linear absorber) while the 20% level is attained after $0.38s$

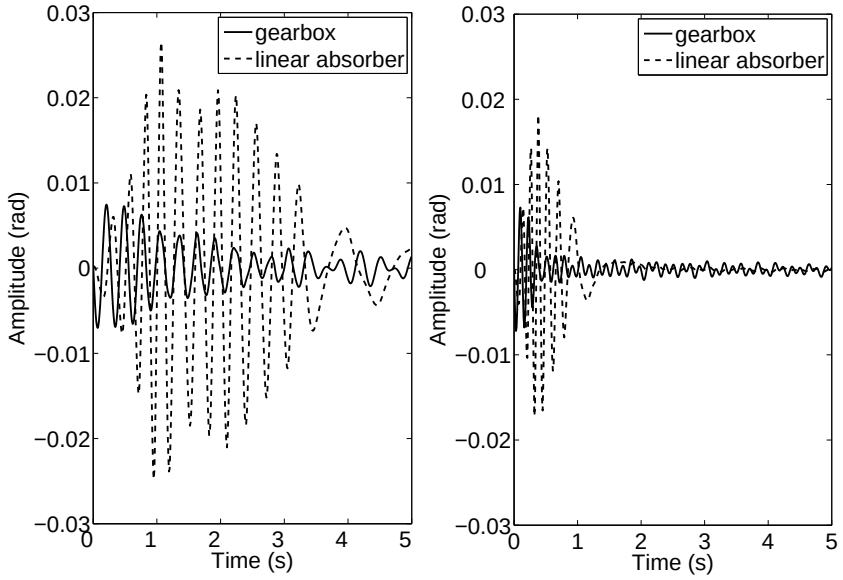

Figure 8.7: Gearbox and nonlinear absorber response for unimodal vibration; Left: Mode 4; Right Mode 5

for mode 5 (instead of 0.31 s when using the linear absorber). As was expected, the linear absorber performs better than the nonlinear absorber when a single vibration mode is dominating the response. Figure 8.6 shows a faster vibration reduction over Fig. 8.7 with the linear absorber in both short term (3 periods) and long term (10 periods). This can be explained by the fact that the frequency of the nonlinear absorber is energy dependent causing at a certain instant a mistuning in frequency. On the other hand, the linear absorber is energy independent resulting in a correct tuning frequency at all time.

8.5 Vibration reduction: multimodal case

Regarding the two dominant modes 4 and 5, the previous section revealed a much better vibration reduction for mode 5 compared to mode 4. Hence, for the multimodal case, we reuse the absorber parameters of the unimodal case of vibration mode 5.

The response of the gearbox, the time-frequency content (wavelet transform) of the relative motion between gearbox and absorber, and the energy dissipated by the absorber are illustrated in Fig. 8.8 and 8.9. As evidenced by the wavelet transform, both absorbers initially reduce energy from vibration mode 5 in a sim-

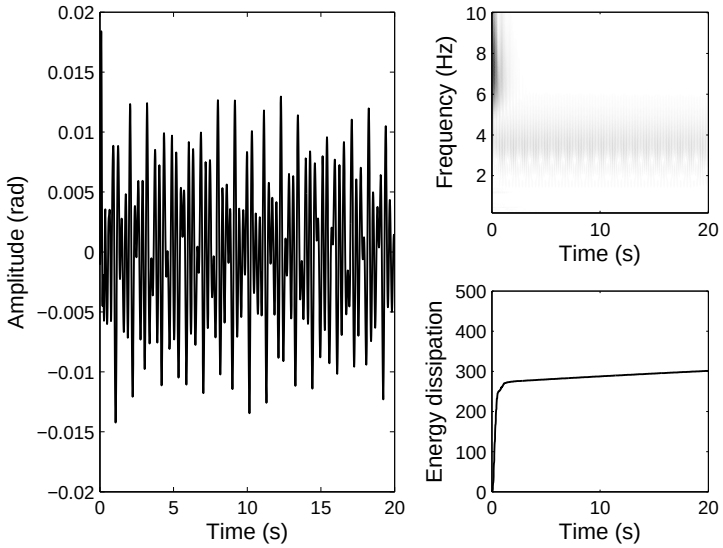

Figure 8.8: Multimodal response at the gearbox with linear absorber ($m_a = 200\ kg\ m^2$)

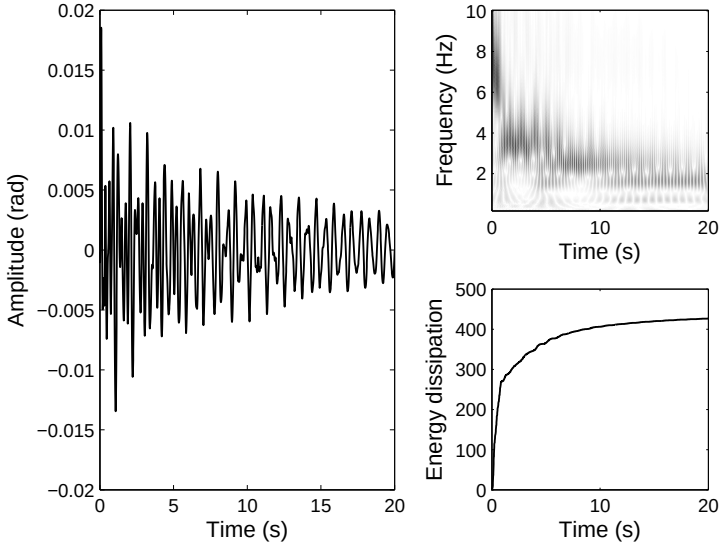

Figure 8.9: Multimodal response at the gearbox with nonlinear absorber ($m_{na} = 200\ kg\ m^2$)

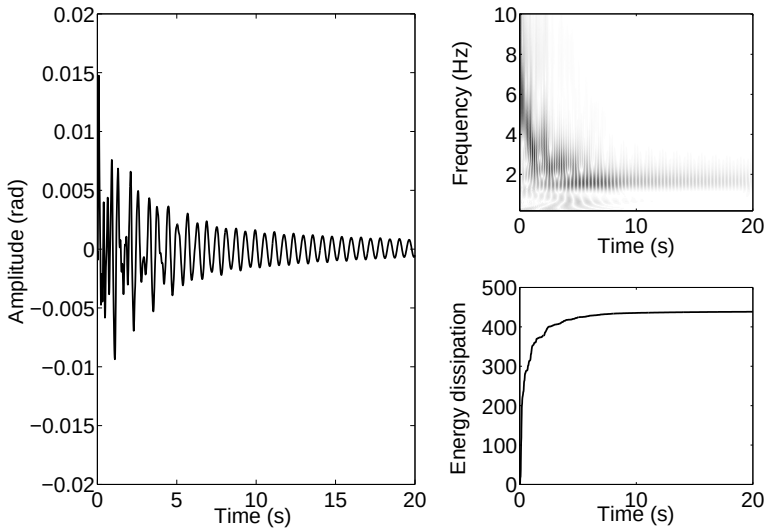

Figure 8.10: Multimodal response at the gearbox with nonlinear absorber ($m_{na} = 800$ kg m^2)

m_{na}	$4 \cdot 200$ kg m^2
k_{na}	$4 \cdot 2.5 \cdot 10^9$ Nm/rad Nm/rad
c_{na}	$4 \cdot 1600$ Nms/rad

Table 8.6: Nonlinear absorber parameters for increased absorber inertia

ilar way. The remaining energy is primarily stored in the other vibration modes which leaves the linear absorber inefficient as it is tuned to mode 5. The nonlinear absorber however succeeds in reducing energy from the other modes as well due to its inherent frequency-energy dependence. These so called *resonance capture cascades* described by [13] are clearly visible in the wavelet transform as the frequency changes from that of mode 5 to those of the lower vibration modes. The corresponding decrease of vibration energy is however much slower than that of the initial phase. Extremely increasing m_{na} to 800 kg m^2 (4 times the initial value or 40 $\%$ of the gearbox inertia), resolves this issue. A much faster energy reduction is achieved for modes 3 and 4 as well although the reduction for mode 2 remains slow (Fig. 8.10). The corresponding absorber parameters are listed in Table 8.6 showing that the values for k_{na} and c_{na} have been chosen 4 times larger as well.

8.6 Conclusion

This chapter demonstrated the capability of the nonlinear absorber to sequentially reduce the energy of multiple vibration modes in a real-life application. Both the reduction technique of Chapter 7 and the design considerations of the nonlinear vibration absorber discussed in Chapter 5 were successfully applied thereby validating their usefulness.

A thorough feasibility study of the strongly nonlinear vibration absorber is not presented and can be the subject of future research. Realizing the sensitivity of the device, an accurate study requires taking into account at least the varying torque of the diesel engine, the speed governor and the drive line's damping properties.

9 Conclusion

Dynamic vibration absorbers will always remain an important tool for the vibration control engineer. Why on earth would you consider expensive and complex solutions like active vibration control if you have these simple, low cost and ingenious devices at hand?

Because of course, they have their limitations. Pushing these limits remains a challenge, even after more than hundred years after their invention. In this thesis, we highlighted the limitations encountered when using the classical linear absorber and its recently developed strongly nonlinear counterpart. A fundamental understanding of the existence of these limitations paves the way towards the further improvement of dynamic vibration absorbers. It is the objective of this dissertation to meet this goal.

The linear vibration absorber

In a first part of this work, we have tried to fill some gaps regarding the classical linear vibration absorber. A first one, discussed in Chapter 3, is the attachment location, an important design parameter of the absorber when dealing with multi-degree-of-freedom systems. The goal of attaching the absorber was focused on obtaining a spectral gap, i.e. a frequency band without troubling resonances. The interlacing property provides crucial information in this matter. It shows that the resonances cannot be shifted beyond their neighboring antiresonances. In other words, the bandwidth of the spectral gap is limited no matter how large the absorber mass is (the limits are reached for $m_a \to \infty$). Now that the limits are determined,

we can exploit this new knowledge.

The key point is that the antiresonances are different for each location of the structure. So instead of the standard way of determining the attachment location, which means according to the eigenvector of the troublesome vibration mode, we can determine it by considering its neighboring antiresonances. The further the antiresonances are away from the troublesome vibration mode, the better the attachment location becomes. An extra interesting insight is that these antiresonances are mainly governed by the eigenvectors of the different vibration modes. Hence, instead of considering only one eigenvector as in the classical single mode approach, it appears that we take into account all of them thereby extending the single mode approach to a multi mode approach.

The link between resonances and antiresonances is even further enhanced in Chapter 4 where the problem of assigning antiresonances is addressed. Because this problem is ill-posed, i.e. a solution does not always exist, we went one step back and have revealed, for a large group of systems, how antiresonances are created and how they can be altered. An important tool in this matter is a substructure decoupling technique which disconnects the system at well chosen positions, obtaining in this way different subsystems. Two of these subsystems seem to be working as multi-degree-of-freedom absorbers, i.e. it's their resonances that, for a large part, constitute the antiresonances of the entire system transforming the initial problem into the problem of shifting resonances.

The nonlinear vibration absorber

In the initial proposal by Frahm, the dynamic vibration absorber is nothing more than a scale-down of the single-degree-of-freedom system to which it is attached to. Turning to multi-degree-of-freedom primary systems a simple scale-down of the entire system is not possible any more because the dynamical element is attached to a single location of the structure. Hence, it sounds reasonable to leave the linear dynamic vibration absorbers behind and to start thinking of dynamic absorbers that are conceptually totally different from the main system. One such absorber is the strongly nonlinear one, i.e. it has a strongly nonlinear (nonlinearizable) stiffness. The advantage over its linear counterpart is the ability to mitigate vibrations at multiple frequencies.

By using the nonlinear absorber, we are entering the world of nonlinear dynamics where the analysis becomes much harder than in the linear case. Moreover, whereas linear systems can be tackled with a generally valid approach, many different analysis techniques are required to fully understand the dynamics in the nonlinear case. Regarding the nonlinear vibration absorber, we have decided to limit the analysis to its amplitude dependency as this defines a crucial design aspect towards a practical implementation. Consequently, we don't obtain a fully detailed

understanding of the dynamics. The advantage of our limited analysis however, is that it can be extended to cope with a large variety of systems, a form of generality not often encountered in nonlinear dynamics.

By nondimensionizing the system, we were able to point out regions in parameter space (comprising mass, stiffness and initial conditions of both the primary system and the absorber) capable of efficient vibration reduction. The boundaries between these regions are quite strict, i.e. only a small change in a parameter value results in a large difference in vibration reduction efficiency of the absorber. As a result, the energy threshold phenomenon (i.e. a minimum input energy into the primary system is required for efficient vibration reduction), is extended to a more general parameter threshold. In this way, we have revealed the influence the different parameters have on the proper functioning of the absorber. We have also experimentally validated these results in a torsional vibration setup using a clamped-clamped wire as a strongly nonlinear absorber stiffness.

Despite this troubling amplitude-dependency, the nonlinear vibration absorber offers some interesting advantages. We have already mentioned its ability to act as a multi-frequency absorber. One that is not discussed in this dissertation, is the possibility of achieving a form of energy localization where energy gets transferred from the primary system towards the nonlinear absorber which acts then as a so called nonlinear energy sink. It could be interesting to further exploit this feature in a more general setting, i.e. is it possible to redistribute the vibration energy of the structure to certain desired locations by introducing nonlinearities, even maybe in the design stage?

Towards an industrial application

In the last part, we have addressed some design issues when linear and nonlinear vibration absorbers are applied to a real-life industrial application. A first important step in their design stage is an accurate theoretical model of the primary system. For the vibration control engineer, the typically used finite element method (FEM) models are far too complex. Consequently, they are to be reduced to a model of manageable size that highlights the important low-frequency behavior.

A very popular one is the Guyan reduction technique, a static condensation method where the entire set of coordinates is divided into masters (to be retained) and slaves (to be condensed out). The key question is which coordinates should be selected as masters. In the classical algorithm, this question is answered by eliminating one by one the slave coordinates such that in the end the desired master set remains. Because the set of masters is generally much smaller than the set of slaves, a large number of iterations is required driving this procedure computationally expensive. Here, we have provided an alternative to this selection procedure where master coordinates are selected one by one instead of slaves. In

addition to a strong reduction in both computing time and memory requirements, a comparable accuracy is obtained. These results hold at least for a large group of systems like those considered in Chapter 7, a conclusive evidence can however not be provided and remains the subject of future research.

As an industrial application we have considered the drive line of a hopper dredger which is suffering from excessive torsional vibrations. This real-life application allowed us to demonstrate the usefulness of the reduction technique and the design considerations of the nonlinear absorber addressed in Part II. As an example, we verified the existence of resonance capture cascades where the nonlinear vibration absorber succeeds in sequentially reducing the energy of different vibration modes. A detailed feasibility study is left for future work where the influence of the diesel engine's excitation, the speed governor and the damping of the main system should be taken into account.

10 Appendix A

10.1 Pilot plant for simulating earthquakes

The first experimental setup displayed in Fig. 10.1 has been constructed to analyze the behavior of a building in the presence of earthquakes. A frame (the building) in aluminium is fixed on a moving plate. The plate oscillates along one horizontal axis and is guided by rails that are fixed on a bottom plate. The moving plate is excited by means of a servomotor via a mechanism that converts the rotating movement of the motor into a linear movement of the plate. The servomotor is able to follow complicated signals such as accelerations due to earthquakes. The acceleration of the moving plate and the top of the frame is measured with accelerometers.

10.2 Benchmark system for vibration testing: a clamped beam

Figure 10.2 shows the second experimental setup developed during the course of this PhD. It addresses the transversal vibrations of a clamped aluminium beam which serves as a benchmark system for vibration testing.

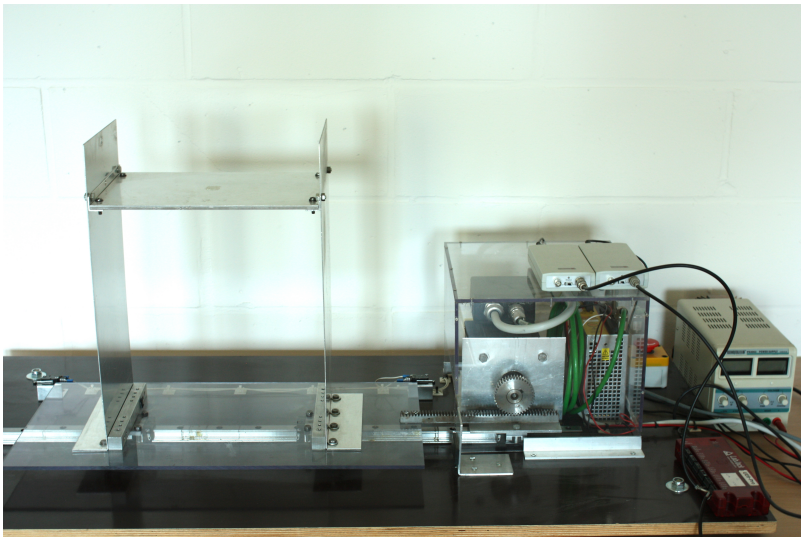

Figure 10.1: Pilot plant for simulating earthquakes

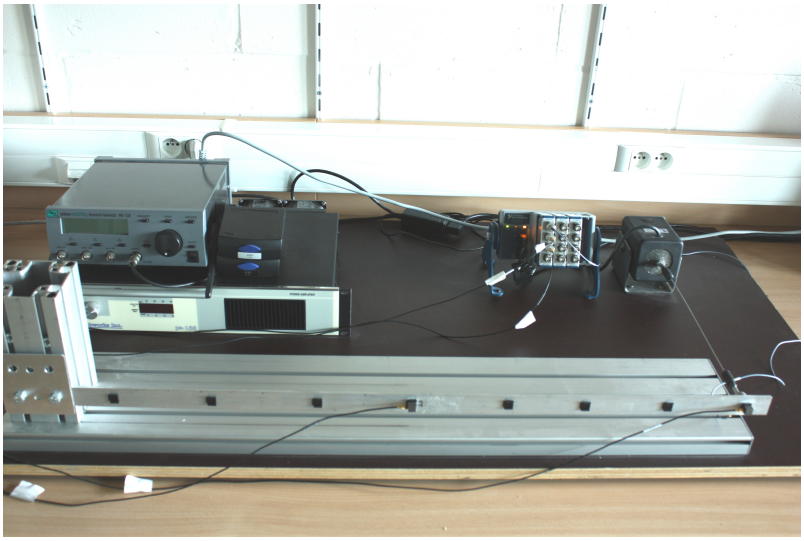

Figure 10.2: Benchmark system for vibration testing: a clamped beam

Bibliography

[1] J. He. Structural Modification. Philosophical Transactions of the Royal Society, 359:187–204, 2001.

[2] A. Preumont. Vibration Control of Active Structures: An Introduction. Kluwer, Dordrecht, 1997.

[3] L. Kela and P. Vhoja. Recent Studies of Adaptive Tuned Vibration Absorbers/Neutralizers. Applied Mechanics Reviews, 62(6), 2009.

[4] N. Jalili. A Comparative Study and Analysis of Semi-Active Vibration-Control Systems. Journal of Vibration and Acoustics, 124:593–605, 2002.

[5] B.G. Korenev and L.M. Reznikov. Dynamic Vibration Absorbers, Theory and Technical Applications. Wiley, New York, 1993.

[6] J.B. Hunt. Dynamic Vibration Absorbers. Mechanical Engineering Publications Ltd., Londen, 1979.

[7] D.J. Mead. Passive Vibration Control. Wiley, New York, 1998.

[8] J.Q. Sun, M.R. Jolly, and M.A. Norris. Passive, Adaptive and Active Tuned Vibration Absorber-a Survey. Transactions of the ASME, 117:234–242, june 1995.

[9] H. Frahm. Device for Damping Vibrations of Bodies. U.S. patent 989,958, 1911.

[10] J.P. Den Hartog. Mechanical Vibrations. McGraw-Hill, New York, 1956.

[11] O. V. Gendelman. Transition of energy to a nonlinear localized mode in a highly asymmetric system of two oscillators. Nonlinear dynamics, 25:237–253, 2001.

[12] A.F. Vakakis, O. Gendelman, L.A. Bergman, D.M. McFarland, G. Kerschen, and Y.S. Lee. Nonlinear Targeted Energy Transfer in Mechanical and Structural Systems. Springer, 2009.

[13] G. Kerschen, J. Kowtko, D.M. McFarland, L.A. Bergman, and A.F. Vakakis. Theoretical and Experimental Study of Multimodal Targeted Energy Transfer in a System of Coupled Oscillators. Nonlinear Dynamics, 47(1-3):285–309, 2007.

[14] T. Kailath. Linear Systems. Prentice Hall, Inc., New Jersey, 1980.

[15] Y.M. Ram. Enlarging a Spectral Gap by Structural Modification. Journal of Sound and Vibration, 176(2):225–234, 1994.

[16] R. Lawther. Enlarging Spectral Gaps of a Structure Using Spring-Mass Oscillators. Available from: www.civeng.unsw.edu.au/staff/ray.lawther/2004, 2004.

[17] G.B. Warburton and E.O. Ayorinde. Optimum Absorber Parameters for Simple Systems. Earthquake Engineering and Structural Dynamics, 8:197–217, 1980.

[18] S.N. Norman. Control Systems Engineering, volume 2. Addison-Wesley Publishing Company, 1995.

[19] D.J. Ewins. Modal Testing: Theory and Practice. Research Studies Press Ltd., Somerset, 1984.

[20] R.L. Fox and M.P. Kapoor. Rates of change of eigenvalues and eigenvectors. AIAA Journal, 6:2426–2429, 1968.

[21] J.K. Vethecan and A. Subic. Measures of Location Effectiveness of Vibration Absorbers. International Journal of Acoustics and Vibration, 7(3):131–140, 2002.

[22] R.E.D. Bishop and D.C. Johnson. The Mechanics of Vibration. Cambridge University Press, Cambridge, 1979.

[23] D.A. Rade and S. Valder. Optimisation of Dynamic Vibration Absorbers over a Frequency Band. Mechanical Systems and Signal Processing, 14(5):679–690, june 2000.

[24] Y.M. Ram and S. Elhay. The Theory of a Multi-Degree-Of-Freedom Dynamic Absorber. Journal of Sound and Vibration, 195(4):607–615, 1996.

[25] J.E. Kyprianou A., Mottershead and H. Ouyang. Assigment of Natural Frequencies by an added Mass and One or More Springs. Mechanical Systems and Processing, 18(2):263–289, march 2004.

[26] R. Lawther. Enlarging spectral gaps of a structure using spring-mass oscillators. unpublished, 2003. Available from: ¡www.civeng.unsw.edu.au/staff/ray.lawther/¿.

[27] R. Lawther. Assessing how changes to a structure can create gaps in the natural frequency spectrum. International Journal of Solids and Structures, 44(2):614–635, 2007.

[28] J.E. Mottershead. Structural Modification for the Assignment of Zeros Using Measured Receptances. Journal of Applied Mechanics, 68(5):791–798, September 2001.

[29] J.E. Mottershead and G. Lallement. Vibration nodes, and the cancellation of poles and zeros by unit-rank modifications to structures. Journal of Sound and Vibration, 222(5):833–851, 1999.

[30] R.E. Roberson. Synthesis of a nonlinear dynamic vibration absorber. Journal of the Franklin Institute, 254:205–220, 1952.

[31] Y. S. Lee, G. Kerschen, A. F. Vakakis, P. N. Panagopoulos, L. A. Bergman, and D. M. McFarland. Complicated dynamics of a linear oscillator with a light, essentially nonlinear attachment. Physica D, 204:41–69, 2005.

[32] G. Kerschen, Y.S. Lee, A.F. Vakakis, D.M. McFarland, and L. Bergman. Irreversible passive energy transfer in coupled oscillators with essential nonlinearity. SIAM Journal on Applied Mathematics, 66:648–679, 2006.

[33] D.D. Quinn, O.V. Gendelman, G. Kerschen, T. Sapsis, L.A. Bergman, and A.F. Vakakis. Efficiency of targeted energy transfers in coupled nonlinear oscillators associated with 1:1 resonance captures: Part I. Journal of Sound and Vibration, 311:1228–1248, 2008.

[34] A.H. Nayfeh and D.T. Mook. Nonlinear Oscillations. John Wiley & Sons, New York, 1995.

[35] R.E. Mickens. Oscillations in an $x^{4/3}$ potential. Journal of Sound and Vibration, 246:275–278, 2001.

[36] L.I. Manevitch. Complex representation of dynamics of coupled nonlinear oscillators. Mathematical models of nonlinear excitations, transfer dynamics and control in condensed systems, pages 269–300, 1999.

[37] W. Govaerts, R. Khoshsiar Ghaziani, Y. Kuznetsov, and H. Meijer. Matcont: A toolbox for continuation and bifurcation of cycles of maps. Universiteit Gent (Belgium) - Utrecht University (The Netherlands), 2007.

[38] S.H. Strogatz. Nonlinear Dynamics And Chaos: With Applications To Physics, Biology, Chemistry, And Engineering (Studies in Nonlinearity). Perseus Publishing, Cambridge, 1994.

[39] B. Vaurigaud, A.T. Savadkoohi, and C.-H. Lamarque. Targeted Energy Transfer with Parallel Nonlinear Energy Sinks. Part I: Design Theory and Numerical Results. Nonlinear Dynamics, 66:763–780, 2011.

[40] T. Nguyen. Etude du comportement dynamique et opimisation d'absorbeurs non-lineaires: théorie et experience. PhD thesis, Université de Lyon, France, 2010.

[41] R. Viguié and G. Kerschen. Nonlinear vibration absorber coupled to a nonlinear primary system: A tuning methodology. Journal of Sound and Vibration, 326:780–793, 2009.

[42] E. Gourdon, C. Taylor, N. Alexander, C.H. Lamarque, and S. Pernot. Nonlinear energy pumping under transient forcing with strongly nonlinear coupling: theoretical and experimental results. Journal of Sound and Vibration,, 300(2-5):522551, 2007.

[43] D.M. McFarland, L.A. Bergman, and A.F. Vakakis. Experimental study of nonlinear energy pumping occurring at a single fast frequency. International Journal of Non-Linear Mechanics, 40:891899, 2005.

[44] D.M. McFarland, G. Kerschen, J.J. Kowtko, Y.S. Lee, L.A. Bergman, and A.F. Vakakis. Experimental investigation of targeted energy transfers in strongly and nonlinearly coupled oscillators. Journal Acoustical Society of America, 118(2):791–799, 2005.

[45] S. Bellizzi, B. Cochelin, and C. Pinhede. A nonlinear energy sink based on a clamped-clamped thin blade. EUROMECH Colloquium 503, 2009.

[46] O.V. Gendelman and Yu. Starosvetsky. Quasi-periodic response regimes of Linear Oscillator Coupled to Nonlinear Energy Sink Under Periodic Forcing. Journal of Applied Mechanics, 74:325–331, March 2007.

[47] R.J. Guyan. Reduction of Stiffness and Mass Matrices. AIAA Journal, 3(2):380, 1965.

[48] R. Kidder. Reduction of structural frequency equations. AIAA Journal, 11(6):892, 1973.

[49] R. Craig and M. Bampton. Coupling of substructures in dynamic analysis. AIAA Journal, 6:1313–1319, 1968.

[50] J. O'Callahan and P. Avitabile. System equivalent reduction expansion process (SEREP). Proceedings of the 7th International Modal Analysis Conference, pages 29–37, 1989.

[51] J. O'Callahan. A procedure for an improved reduced system (IRS) model. Proceedings of the 7th International Modal Analysis Conference, pages 17–21, 1989.

[52] A.N. Krylov. On the numerical solution of the equation by which in technical questions frequencies of small oscillations of material systems are determined. Otdelenie Matematicheskikh i Estestvennykh Nauk, 2(4):491–539, 1931. original text in Russian.

[53] E.L. Wilson, M.W. Yuan, and J.M. Dicken. Dynamic analysis by direct superposition of Ritz vectors. Earthquake Engineering and Structural Dynamics, 10:813–821, 1982.

[54] P. Koutsovasilis and M. Beitelschmidt. Comparison of model reduction techniques for large mechanical systems. Multibody System Dynamics, 20(2):111–128, 2008.

[55] R.D. Henshell and J.H. Ong. Automatic Masters for Eigenvalue Economisation. International Journal of Earthquake Structural Dynamics, 3:375–383, 1975.

[56] K.O. Kim and Y.J. Choi. Energy Method for Selection of Degrees of Freedom in Condensation. AIAA Journal, 37(7):1253–1259, July 2000.

[57] M. Cho and H. Kim. Element-based node selection method for reduction of eigenvalue problems. AIAA Journal, 42(8):1677–1684, 2004.

[58] H. Kim and M. Cho. Two-level scheme for selection of primary degrees of freedom and semi-analytic sensitivity based on the reduced system. Computer Methods in Applied Mechanics and Engineering, 195(33-36):4244–4268, July 2006.

[59] V.N. Shah and M. Raymund. Analytical Selection of Masters for the Reduced Eigenvalue Problem. International Journal for Numerical Methods in Engineering, 18:89–98, 1982.

[60] K.W. Matta. Selection of Degrees of Freedom for Dynamic Analysis. Journal of Pressure Vessel Technology, 109(1):65–69, 1987.

[61] J.E. Penny, M.I. Friswell, and S.D. Garvey. The automatic choice of measurement locations for dynamic testing. AIAA Journal, 32(2):407–414, 1994.

[62] Z. Qu. Model Order Reduction Techniques: with applications in finite element analysis. Springer, 2004.

[63] M.R. Hatch. Vibration simulation using MATLAB and ANSYS. Chapman & Hall/CRC, 2001.

[64] S.A. Kilic, F. Saied, and A. Sameh. Efficient iterative solvers for structural dynamics problems. Computers and Structures, 82:2363–2375, 2004.

[65] H.M. Bücker. Iteratively solving large sparse linear systems on parallel computers. NIC series, 10:521–548, 2002.

[66] L.M. Adams. Rotating Machinery Vibration, From Analysis to Trouble Shooting. Marcel Dekker Inc., New York, 2001.

[67] M. Blanke and P.B. Nielsen. The marine engine governor. Maritime Communications and Control, pages 21–23, november 1990.

[68] R. Izadi-Zamanabadi and M. Blanke. A ship propulsion system as a benchmark for fault-tolerant control. Control Engineering Practice, 7(2):227–239, 1999.

[69] R.N. Bray and A.D. Bates. Dredging: A Handbook for Engineers. John Wiley and Sons Inc., New York, 2 edition, 1996.

[70] R. Rana and T.T. Soong. Parametric study and simplified design of tuned mass dampers. Engineering Structures, 20(3):193–204, 1998.